

ABSTRACT

YAN, JUN. Well-Balanced Schemes for the Non-Hydrostatic Saint-Venant System and Atmospheric Flow Equations with Gravity. (Under the direction of Dr. Alina Chertock.)

In this dissertation, we focus on numerical solutions describing two types of PDE models: a non-hydrostatic Saint-Venant system describing tsunami-like waves and gravitationally stratified atmospheric flows governed by the compressible Euler equations with gravity.

In the introductory chapter, we describe the exact Riemann solver for one-dimensional Euler equations to introduce shock, rarefaction, and contact waves that can help to understand the nature of hyperbolic PDEs. Then we present the efficient and robust second-order semi-discrete central-upwind scheme with an anti-diffusion term. This scheme is at the center of our study.

The second chapter is concerned with numerical schemes for tsunami-like waves and tests for their long-time performance and on-shore behaviors. The classical Saint-Venant system is a depth-averaged system that can be derived from Euler equations and is usually used to model the flows of coastal areas, lakes, and rivers in a relatively short time or spatial scale. Tsunami waves in deep water, however, travel very long distances without too much decay in their amplitudes. The non-hydrostatic Saint-Venant system derived by M.-O. Bristeau and J. Sainte-Marie(2008), work well for characterizing the long-time propagation of tsunami-like waves. Compared with the classical Saint-Venant system, the non-hydrostatic Saint-Venant model has non-hydrostatic pressure terms that need special treatments. These non-hydrostatic pressure terms will make the non-hydrostatic model dispersive, but they can also keep wave shape during long-time propagation. In our numerical simulations, we can capture the on-shore arrival of tsunami-like waves in which the front of the non-hydrostatic solution is about 10-20km behind the hydrostatic one, suggesting that non-hydrostatic terms are necessary to be included in an accurate tsunamis model.

In the third chapter, we simulate gravitationally stratified atmospheric flows governed by the compressible Euler equations with gravity in irregular domains. We consider irregular domains in 2-D. At the early stage of this research, we used Cartesian grids for irregular domains and solved the local Riemann problem for cells near irregular boundaries. The numerical results, however, showed incorrect airflow velocities when they passed irregular boundaries. The reason should be that the use of regular rectangular grids that intersect with irregular boundaries leads to the generation of arbitrarily small and highly distorted computational cells adjacent to boundaries of domains. The scheme itself might be easy to implement, but it fails to describe flows past boundaries accurately. A recently developed second-order central-upwind numerical scheme on quadrilateral meshes is introduced in this chapter to overcome this challenge. In addition, to make the scheme well-balanced, we rewrite the governing equations in terms of equilibrium variables representing perturbations of the physically relevant equilibrium. In our numerical simulations, we show how to design an appropriate quadrilateral mesh on irregular domains and demonstrate high resolution and robustness of the central-upwind numerical scheme on quadrilateral meshes.

© Copyright 2021 by Jun Yan

All Rights Reserved

Well-Balanced Schemes for the Non-Hydrostatic Saint-Venant System and Atmospheric Flow
Equations with Gravity

by
Jun Yan

A dissertation submitted to the Graduate Faculty of
North Carolina State University
in partial fulfillment of the
requirements for the Degree of
Doctor of Philosophy

Applied Mathematics

Raleigh, North Carolina

2021

APPROVED BY:

Dr. Zhilin Li

Dr. Hien Tran

Dr. Yunan Liu

Dr. Alina Chertock
Chair of Advisory Committee

DEDICATION

To my parents, Guoxing Yan and Tiaoxian Hu, who always love, encourage and support me.

BIOGRAPHY

Jun Yan was born in 1990, Hangzhou, Zhejiang province, China. He grew up in this small beautiful city and received his B.S. degree in Pure and Applied Mathematics in 2012 at Zhejiang University. He continued his studies at Stony Brook University and received an M.S. degree in Applied Mathematics in 2014. He then entered the Ph.D. program in Applied Mathematics at NCSU. Under the guidance of Dr. Alina Chertock, he started doing researches on numerical PDEs.

ACKNOWLEDGEMENTS

First of all, words are not enough to express my gratitude to my advisor, Dr. Alina Chectock. It's hard to imagine my entire graduate career without her continuous patience and infinite support. I would like to thank her help and tremendous inspiration in research. I should also thank our collaborators, Dr. Alexander Kurganov for his insightful ideas and significant contributions. I am thankful to Dr. Tong Wu for his great help in coding and research.

I would also thank the rest of my thesis committee: Dr. Zhilin Li, Dr. Hien Tran, and Dr. Yunan Liu for their encouragement, support and inspiration in research and real life.

I would like to thank my friends, Ran Bi, Jiabin Yu, and Yahe Yu for their help in studying courses and doing research.

TABLE OF CONTENTS

LIST OF TABLES	vi
LIST OF FIGURES	vii
Chapter 1 INTRODUCTION	1
1.1 Models	2
1.2 Hyperbolic Conservation/Balance Laws	2
1.3 Euler Equations	3
1.4 Saint-Venant Systems	5
1.4.1 Classical Saint-Venant System	7
1.4.2 Non-Hydrostatic Saint-Venant System	9
1.4.3 Steady States of Saint-Venant System	16
1.5 Compressible Euler Equation for Ideal Gas	18
1.6 Numerical Methods	21
1.6.1 Finite Volume Method	21
1.6.2 Semi-Discrete Central-Upwind Scheme	24
Chapter 2 Non-Hydrostatic Saint-Venant System	34
2.1 Mathematical Model	35
2.1.1 Central-Upwind Scheme	35
2.1.2 Time Evolution	41
2.2 Numerical Experiments	42
Chapter 3 Atmospheric Flow Equations with Gravity	53
3.1 Mathematical Model	54
3.2 Model Description and Numerical Method	55
3.2.1 Two-Dimensional Semi-Discrete Scheme	56
3.3 Numerical Examples	60
3.3.1 Example 1 (Convergence Test)	61
3.3.2 Example 2 (Zeppelin Test)	62
3.3.3 Example 3 (Lee Waves)	67
Chapter 4 Conclusions and Future Work	74
BIBLIOGRAPHY	75
APPENDICES	80
Appendix A Leibniz Integral Rule	81
Appendix B Rankine-Hugoniot Jump Condition	82
B.1 Derivation of Rankine-Hugoniot Jump Condition	82
Appendix C Third-Order Strong Stability Preserving Runge-Kutta Methods	84

LIST OF TABLES

Table 2.2.1	L^∞ -, L^1 - and L^2 -errors in w and the corresponding experimental rates of convergence.	48
Table 2.2.2	L^∞ -, L^1 - and L^2 -errors in q and the corresponding experimental rates of convergence.	48
Table 2.2.3	Parameters used in for the bottom topography functions (2.2.1) and (2.2.2).	48
Table 3.3.1	Example 1: Experimental convergence rates in the L^1 -norm.	62
Table 3.3.2	Lee-wave parameters.	69

LIST OF FIGURES

Figure 1.4.1	Shallow water model: bottom $B(x)$, free surface, $\eta(x, t)$ and water height $h(x, t)$,	6
Figure 1.6.1	Domain of Dependence from Different Cells	23
Figure 1.6.2	(a) Upwind control volume (b) Central control volume (c) Central-upwind control volumes	25
Figure 1.6.3	Control volumes selected according to smooth and nonsmooth areas	27
Figure 2.2.1	Example 1: Time evolution of the water surface for $\alpha_M = 0.8$ and $\alpha_N = 0, 1, 2, 3$	43
Figure 2.2.2	Example 1: Time evolution of the water surface for $\alpha_N = 0$ and $\alpha_M = 0, 0.2, 0.6, 1.2$	44
Figure 2.2.3	Example 1: Time evolution of the water surface for $\alpha_M = \alpha_N = 0$ (left) and 0.01 (right).	45
Figure 2.2.4	Example 1: Time evolution of the water surface for $\alpha_M = \alpha_N = 0.02$ (top left), 0.03 (top right), 0.04 (bottom left) and 0.05 (bottom right).	46
Figure 2.2.5	Example 1: Time evolution of the water surface for $\alpha_M = \alpha_N = 0.1$ (top left), 0.25 (top right), 0.5 (bottom left) and 1 (bottom right).	47
Figure 2.2.6	Example 1: Time evolution of the water surface for $\alpha_M = \alpha_N = 2$ (left) and 5 (right).	47
Figure 2.2.7	Example 2: Initial water surface (left) and discharge (right).	48
Figure 2.2.8	Example 2: The bottom topography function (2.2.1).	49
Figure 2.2.9	Example 2: Time evolution of the water surface for the classical Saint-Venant system ($\alpha_M = \alpha_N = 0$).	49
Figure 2.2.10	Example 2: Time evolution of the water surface for $\alpha_M = \alpha_N = 0.05$ (top left), 0.1 (top right), 0.15 (bottom left) and 0.2 (bottom right).	50
Figure 2.2.11	Example 3: The bottom topography function (2.2.2).	51
Figure 2.2.12	Example 3: On-shore arrival of the tsunami-like waves in the hydrostatic ($\alpha_M = \alpha_N = 0$) and non-hydrostatic with $\alpha_M = \alpha_N = 0.2$ regimes.	51
Figure 2.2.13	Example 3: Same as Figure 2.2.12, but zoomed in.	52
Figure 3.2.1	Quadrilateral cell $C_{j,k}$ with its four neighbors	57
Figure 3.3.1	Example 1: Computational domain (left) and structured quadrilateral mesh (right).	61
Figure 3.3.2	Example 2: Computational domain.	63
Figure 3.3.3	Example 2: Structured quadrilateral mesh.	64
Figure 3.3.4	Example 2: Potential temperature θ at different times.	67
Figure 3.3.5	Same as Figure 3.3.4, but the results are computed using a finer mesh.	68
Figure 3.3.6	Example 3: Computational domain.	69
Figure 3.3.7	Example 3: Structured quadrilateral mesh.	70
Figure 3.3.8	Example 3: Potential temperature θ at $t = 293.4$ for Cases (a)–(c). Contours are plotted at intervals of $\Delta\theta = 0.01$	72
Figure 3.3.9	Same as Figure 3.3.8, but the results are computed using a finer mesh.	73

CHAPTER

1

INTRODUCTION

In this dissertation, we study two types of systems: the non-hydrostatic Saint-Venant system and gravitationally stratified atmospheric flows model governed by the compressible Euler equations with gravity.

Non-hydrostatic Saint-Venant models work quite well for tsunami waves in deep water. These tsunami waves usually travel a very long distance without too much decrease in wave amplitudes until they reach the shore. They are hard to be noticed offshore, but contain a tremendous amount of kinetic energy, because of their relatively large wave speed and wavelength. During the on-shore arrival stage, tsunamis slow down, and their wavelength decrease. In order to conserve energy, part of their kinetic energy will become potential energy, and the wave amplitudes increase. This will release a disastrous impact when the waves come to shore. Therefore, it's very important to predict the arrival time of tsunami waves and how long they will last.

Gravitationally stratified atmospheric flows governed by the compressible Euler equations have lots of applications in predicting weather and climate changes. Hydrostatics is the branch of fluid mechanics that studies fluids at rest. It can offer physical explanations of many phenomena of daily life, such as why atmospheric pressure and density change with altitude. These flows are called gravitationally stratified flows. In many applications, solutions of the system are small perturbations of gravitationally stratified flows. To understand the dynamics of such flows, we consider the fully compressible system of Euler equations with gravity as our model.

1.1 Models

The study of fluid dynamics is important in a variety of scientific scenarios, including forecasting tsunami waves, predicting climate changes, controlling pollution, and explaining the behaviors of nebulae in interstellar space. The formulation of the equations describing fluid dynamics stands among the greatest achievements in science. Here, we focus our attention on the Euler equations, the hyperbolic system of conservation/balance laws.

The derivation of the Euler equations without gravity is based on 3 conservation laws: conservation of mass, conservation of momentum, and conservation of energy. And a description of conservation laws is provided below.

1.2 Hyperbolic Conservation/Balance Laws

In this dissertation, we will denote bold symbols as vector functions and plain symbols as scalar functions. For example, \mathbf{x} , \mathbf{q} and \mathbf{F} are vector functions(or variables) and x , q and F are scalar functions(or variables).

Conservation laws describe a type of PDEs that have the property of conserving certain quantities during time evolution. In mathematics, it has the following differential form in d dimensions:

$$\frac{\partial}{\partial t} \mathbf{q}(\mathbf{x}, t) + \sum_{i=1}^d \frac{\partial \mathbf{F}_i(\mathbf{q}(\mathbf{x}, t))}{\partial x_i} = 0, \quad (1.2.1)$$

where $\mathbf{x} = (x_1, \dots, x_d)^T \in \Omega$ are spatial variables, time variable t , $\mathbf{q} = \mathbf{q}(\mathbf{x}, t)$ are m unknown functions $\mathbf{q}(\mathbf{x}, t) : \Omega \times \mathbb{R}^+ \longrightarrow \mathbb{R}^m$, and the flux functions $\mathbf{F}_i(\mathbf{q}(\mathbf{x}, t)) : \Omega \times \mathbb{R}^+ \longrightarrow \mathbb{R}^m$. Here, $1 \leq i \leq d$ and the computational domain is $\Omega \in \mathbb{R}^d$. If $d = 1$ and $m = 1$, $q(x, t)$ is a scalar function, and then the flux function becomes a scalar-valued function:

$$\frac{\partial}{\partial t} q(x, t) + \frac{\partial}{\partial x} F(q(x, t)) = 0. \quad (1.2.2)$$

The above equation is called a scalar conservation law. When $m \geq 2$, $\mathbf{q}(\mathbf{x}, t)$ and $\mathbf{F}(\mathbf{q}(\mathbf{x}, t)) := (\mathbf{F}_i(\mathbf{q}(\mathbf{x}, t)))_{1 \leq i \leq d}$ are vector-valued, the equation (1.2.1) is called a system of conservation laws:

$$\frac{\partial}{\partial t} \mathbf{q}(\mathbf{x}, t) + \nabla \cdot \mathbf{F}(\mathbf{q}(\mathbf{x}, t)) = 0. \quad (1.2.3)$$

The initial conditions should be given: $\mathbf{q}(\mathbf{x}, 0) = \mathbf{q}_0(\mathbf{x})$ for $\mathbf{x} \in \Omega$. The boundary conditions in this dissertation are usually wall boundary conditions or periodic boundary conditions.

The concept of conservation laws is derived from the fact that in an isolated system without external force, some quantities of the whole system remain unchanged regardless of time evolution. Later, we will show the role of conservation laws in deriving Euler equations.

In this dissertation, we also discuss hyperbolic systems of balance laws:

$$\frac{\partial}{\partial t} \mathbf{q}(\mathbf{x}, t) + \nabla \cdot \mathbf{F}(\mathbf{q}(\mathbf{x}, t)) = \mathbf{S}(\mathbf{q}), \quad (1.2.4)$$

where $\mathbf{S}(\mathbf{q})$ is the vector of source terms. Compared with (1.2.3), the system of balance laws is the system of conservation laws with additional source terms.

1.3 Euler Equations

Euler equations were introduced in Leonhard Euler's famous work "Principes généraux du mouvement des fluides" in 1757. These equations play a central role in studying fluid dynamics and describe the time evolution of inviscid and adiabatic flows in space.

Euler equations study 3 quantities of fluids: density, velocity and energy. Originally, Leonhard Euler found 2 differential equations for conservation laws of mass and momentum. But conservation laws of momentum involves pressure term, which should be closed by another state variable. So the conservation law of energy is developed.

First, let's derive the conservation of mass(the continuity equation). In a control volume Ω with its boundary $\partial\Omega$, we can express ρ as its fluid density. The rate of change of total mass in Ω is

$$\frac{\partial}{\partial t} \int_{\Omega} \rho dV. \quad (1.3.1)$$

Meanwhile, we let u denote the fluid velocities in x direction, \mathbf{n} the outward normal vector on surface $\partial\Omega$. The rate of change of total mass should equal to the net density flow rate(density flux) ρu into $\partial\Omega$:

$$\frac{\partial}{\partial t} \int_{\Omega} \rho dV = - \int_{\partial\Omega} (\rho u) \cdot \mathbf{n} dA. \quad (1.3.2)$$

Applying the Divergence Theorem to right side of (1.3.2), we have

$$\frac{\partial}{\partial t} \int_{\Omega} \rho dV = - \int_{\Omega} \nabla \cdot (\rho u) dV. \quad (1.3.3)$$

Rearrange all terms into the integral of Ω ,

$$\int_{\Omega} \left[\frac{\partial}{\partial t} \rho + \nabla \cdot (\rho u) \right] dV = 0. \quad (1.3.4)$$

By the assumption of continuum mechanics, any arbitrary small control volume can be applied to this equation. So we have derived the conservation of mass:

$$\frac{\partial}{\partial t} \rho + \nabla \cdot (\rho u) = 0. \quad (1.3.5)$$

It is a special case of a scalar conservation law when $q = \rho$ and density flux function $F(q) = \rho u$:

$$\frac{\partial}{\partial t} q + \nabla \cdot F(q) = 0, \quad (1.3.6)$$

Second, in a system with no external force, we need to consider the flux function of momentum ρu . Momentum flux is made up with two components: advective momentum flux ρu^2 and microscopic momentum flux due to pressure P . Thus we have the conservation law of momentum:

$$\frac{\partial \rho u}{\partial t} + \nabla \cdot (\rho u^2 + P) = 0. \quad (1.3.7)$$

Third, if we are studying idea gas, total energy can be expressed as $E = \frac{1}{2} \rho u^2 + \frac{P}{\gamma-1}$. Apparently, we have macroscopic energy flux $E u$. Meanwhile, microscopic momentum flux P mentioned before will lead to microscopic energy flux $P u$. Thus we have the conservation law of energy:

$$\frac{\partial E}{\partial t} + \nabla \cdot ((E + p)u) = 0. \quad (1.3.8)$$

3 conservation laws mentioned above make up the one-dimensional Euler equation:

$$\begin{cases} \rho_t + (\rho u)_x = 0, \\ (\rho u)_t + (\rho u^2 + p)_x = 0, \\ E_t + ((E + p)u)_x = 0, \end{cases} \quad (1.3.9)$$

The multi-dimensional Euler equation without gravity(or external source) can be given as:

$$\begin{cases} \frac{\partial}{\partial t} \rho + \nabla \cdot (\rho \mathbf{u}) = 0, \\ \frac{\partial \rho \mathbf{u}}{\partial t} + \nabla \cdot (\rho \mathbf{u} \otimes \mathbf{u} + p \mathbf{I}) = 0, \\ \frac{\partial E}{\partial t} + \nabla \cdot ((E + p)\mathbf{u}) = 0, \end{cases} \quad (1.3.10)$$

where \mathbf{u} are fluid velocity in multi-dimension, \otimes is the tensor product that if we have $v = [v_1, v_2, \dots, v_n]$ and $w = [w_1, w_2, \dots, w_m]$,

$$v \otimes w = \begin{bmatrix} v_1 w_1 & v_1 w_2 & \cdots & v_1 w_m \\ v_2 w_1 & v_2 w_2 & \cdots & v_2 w_m \\ \vdots & \vdots & \ddots & \vdots \\ v_n w_1 & v_n w_2 & \cdots & v_n w_m \end{bmatrix},$$

and \mathbf{I} is the identity matrix.

1.4 Saint-Venant Systems

The classical and non-hydrostatic Saint-Venant systems can be derived from the Euler equations mentioned above. Here, we will derive these 2 systems as an introductory part. In chapter 2, we will discuss numerical schemes of these systems in details.

Similar to the Euler equations in conservation laws(without force) mentioned in (1.3.10), we start from the Euler equations with gravitational source in two dimensional cases:

$$\begin{cases} \frac{\partial}{\partial t}\rho + (\rho u)_x + (\rho v)_y = 0, \\ \frac{\partial \rho u}{\partial t} + (\rho u^2 + p)_x + (\rho uv)_y = 0, \\ \frac{\partial \rho v}{\partial t} + (\rho v u)_x + (\rho v^2 + p)_y = -\rho g. \end{cases} \quad (1.4.1)$$

where x and y are spatial variables, u and v represent horizontal and vertical velocities, respectively, and g is the acceleration due to gravity.

Since water is usually treated as homogeneous:

$$\nabla \rho = 0, \quad (1.4.2)$$

and incompressible:

$$\nabla \cdot u = 0, \quad (1.4.3)$$

we can derive:

$$\frac{\partial \rho}{\partial t} = -\rho(u_x + v_y) - (u\rho_x + v\rho_y) = 0, \quad (1.4.4)$$

from the first equation(the conservation law of mass) in (1.4.1). This suggests homogeneous incompressible flows have constant density:

$$\rho = \text{constant}. \quad (1.4.5)$$

So, water density is constant for both classical and non-hydrostatic systems. The Euler equations with gravity then becomes:

$$\begin{cases} \frac{\partial u}{\partial x} + \frac{\partial v}{\partial y} = 0, \\ \frac{\partial u}{\partial t} + u \frac{\partial u}{\partial x} + v \frac{\partial u}{\partial y} + \frac{1}{\rho} \frac{\partial p}{\partial x} = 0, \\ \frac{\partial v}{\partial t} + u \frac{\partial v}{\partial x} + v \frac{\partial v}{\partial y} + \frac{1}{\rho} \frac{\partial p}{\partial y} = -g. \end{cases} \quad (1.4.6)$$

Then this system (1.4.6) is complete with boundary conditions. We denote the bottom as $B(x)$, the free surface $\eta(x, t)$ and water depth measured vertically from the bottom topography $h(x, t) =$

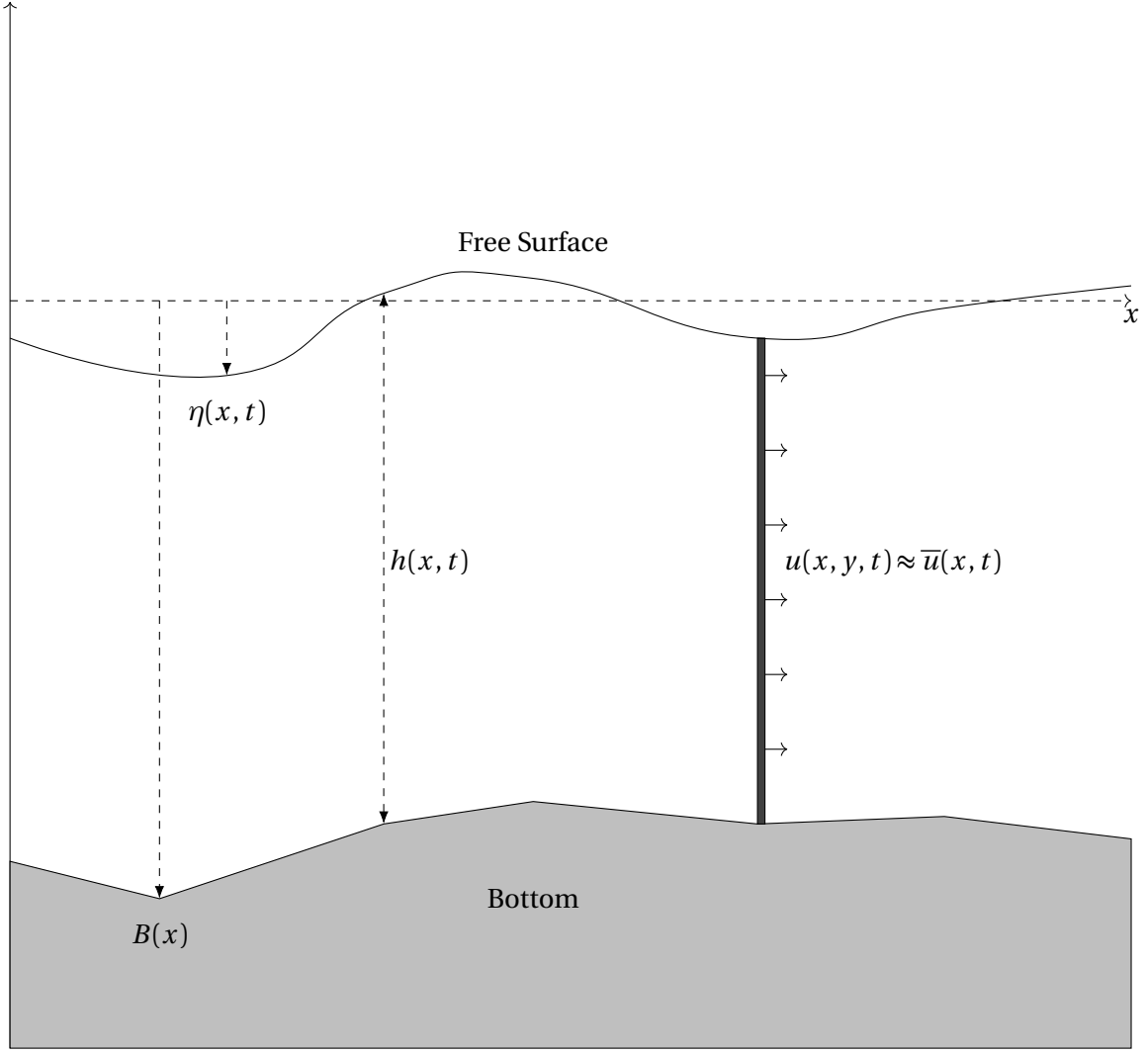


Figure 1.4.1 Shallow water model: bottom $B(x)$, free surface, $\eta(x, t)$ and water height $h(x, t)$,

$\eta(x, t) - B(x)$ in Figure 1.4.1.

Two kinematic boundary conditions are given here. At the bottom $y = B(x)$, we have no normal flow:

$$\frac{\partial B}{\partial t} + u_b \frac{\partial B}{\partial x} - v_b = 0, \quad (1.4.7)$$

with u_b and v_b the horizontal and vertical velocities at the bottom.

At the surface $y = \eta(x, t)$, we have no normal flow:

$$\frac{\partial \eta}{\partial t} + u_\eta \frac{\partial \eta}{\partial x} - v_\eta = 0, \quad (1.4.8)$$

with u_η and v_η the horizontal and vertical velocities at the surface.

1.4.1 Classical Saint-Venant System

The classical Saint-Venant system is a kind of shallow water equations describing a thin layer of homogeneous incompressible flow with its vertical height much less than its horizontal length scale of the computational domain. From this shallow water assumption, the vertical velocity of the fluid $v(x, y, t)$ would be negligible, and the velocity are roughly constant regardless of its depth y : $u(x, y, t) \approx \bar{u}(x, t)$. Related discussion and rescaled system can be seen in [Bri08]. And below is the related definition of averaged quantities:

$$\bar{u}(x, t) := \frac{1}{\eta - B} \int_B^\eta u(x, y, t) dy, \quad \bar{u^2}(x, t) := \frac{1}{\eta - B} \int_B^\eta u^2(x, y, t) dy. \quad (1.4.9)$$

Using Leibniz integral rule for differentiation in A, we can derive the continuity equation for the classical Saint-Venant system:

$$\begin{aligned} \frac{\partial h}{\partial t} + \frac{\partial}{\partial x}(h\bar{u}) &= \frac{\partial(\eta - B)}{\partial t} + \frac{\partial}{\partial x} \left(\int_B^\eta u(x, y, t) dy \right) \\ &= \frac{\partial \eta}{\partial t} - \frac{\partial B}{\partial t} + \int_B^\eta \frac{\partial u}{\partial x} dy + u_\eta \frac{\partial \eta}{\partial x} - u_b \frac{\partial B}{\partial x} \\ &= \frac{\partial \eta}{\partial t} + u_\eta \frac{\partial \eta}{\partial x} - \int_B^\eta \frac{\partial v}{\partial y} dy - \frac{\partial B}{\partial t} - u_b \frac{\partial B}{\partial x} \\ &= \frac{\partial \eta}{\partial t} + u_\eta \frac{\partial \eta}{\partial x} - v_\eta + v_b - \frac{\partial B}{\partial t} - u_b \frac{\partial B}{\partial x} \\ &= 0. \end{aligned} \quad (1.4.10)$$

For the third equation of (1.4.6),

$$\frac{\partial v}{\partial t} + u \frac{\partial v}{\partial x} + v \frac{\partial v}{\partial y} + \frac{1}{\rho} \frac{\partial p}{\partial y} = -g, \quad (1.4.11)$$

Classic shallow water equation use the hydrostatic approximation by setting the material derivative of the vertical velocity v to be 0:

$$\frac{Dv}{Dt} := \frac{\partial v}{\partial t} + u \frac{\partial v}{\partial x} + v \frac{\partial v}{\partial y} = 0. \quad (1.4.12)$$

Pressure can thus be approximated using hydrostatic equation:

$$\frac{\partial p}{\partial y} = -\rho g. \quad (1.4.13)$$

At the free surface of $y = \eta$, the pressure is equal to air pressure p^a . The classic hydrostatic pressure:

$$p = p^a + \rho g(\eta - y), \quad (1.4.14)$$

Then we can derive the horizontal momentum equation for classic shallow water system:

$$\begin{aligned}
\frac{\partial(h\bar{u})}{\partial t} + \frac{\partial}{\partial x}(h\bar{u}^2) &= \frac{\partial}{\partial t} \left(\int_B^\eta u(x, y, t) dy \right) + \frac{\partial}{\partial x} \left(\int_B^\eta u^2(x, y, t) dy \right) \\
&= \eta_t u_\eta - B_t u_b + \int_B^\eta \frac{\partial u}{\partial t} dy + \eta_x u_\eta^2 - B_x u_b^2 + \int_B^\eta 2u u_x dy \\
&= \eta_t u_\eta + \eta_x u_\eta^2 - B_t u_b - B_x u_b^2 + \int_B^\eta u u_x dy + \int_B^\eta \frac{\partial u}{\partial t} dy + \int_B^\eta u u_x dy \\
&= \eta_t u_\eta + \eta_x u_\eta^2 - B_t u_b - B_x u_b^2 - \int_B^\eta u v_y dy + \int_B^\eta \frac{\partial u}{\partial t} dy + \int_B^\eta u u_x dy \\
&= \eta_t u_\eta + \eta_x u_\eta^2 - B_t u_b - B_x u_b^2 - \left(u_\eta v_\eta - u_b v_b - \int_B^\eta u_y^0 dy \right) + \int_B^\eta \frac{\partial u}{\partial t} dy + \int_B^\eta u u_x dy \\
&= u_\eta \left(\eta_t + \eta_x u_\eta - v_\eta \right) - u_b \left(B_t + B_x u_b - v_b \right) + \int_B^\eta \left(\frac{\partial u}{\partial t} + u u_x \right) dy \\
&= \int_B^\eta \left(\frac{\partial u}{\partial t} + u u_x \right) dy \\
&= - \int_B^\eta \left(u \frac{\partial u}{\partial y} + \frac{1}{\rho} \frac{\partial p}{\partial x} \right) dy \\
&= -g \int_B^\eta \left(\frac{\partial \eta}{\partial x} \right) dy \\
&= -g \int_B^\eta \left(h_x + B_x \right) dy \\
&= -g h \left(h_x + B_x \right) dy \\
&= -\frac{\partial}{\partial x} \left(\frac{1}{2} g h^2 \right) - g h B_x.
\end{aligned}$$

Above all, the classic Saint-Venant system is derived by replacing depth average value \bar{u} with u

$$\begin{cases} h_t + (hu)_x = 0, \\ (hu)_t + \left(hu^2 + \frac{g}{2} h^2 \right)_x = -g h B_x. \end{cases} \quad (1.4.15)$$

Remark 1.4.1 Notice that $h\bar{u}^2$ is approximated by $h\bar{u}^2$ because $u(x, y, t) \approx \bar{u}(x, t)$ (See [Bri08; Fal93] for more details).

1.4.2 Non-Hydrostatic Saint-Venant System

Let's start with the 2-dimensional Euler equation with gravity (1.4.1):

$$\begin{cases} \frac{\partial u}{\partial x} + \frac{\partial v}{\partial y} = 0, \\ \frac{\partial u}{\partial t} + u \frac{\partial u}{\partial x} + v \frac{\partial u}{\partial y} + \frac{1}{\rho} \frac{\partial p}{\partial x} = 0, \\ \frac{\partial v}{\partial t} + u \frac{\partial v}{\partial x} + v \frac{\partial v}{\partial y} + \frac{1}{\rho} \frac{\partial p}{\partial y} = -g, \end{cases} \quad (1.4.16)$$

with kinematic boundary conditions:

$$\begin{cases} \frac{\partial B}{\partial t} + u_b \frac{\partial B}{\partial x} - v_b = 0, \\ \frac{\partial \eta}{\partial t} + u_\eta \frac{\partial \eta}{\partial x} - v_\eta = 0, \end{cases} \quad (1.4.17)$$

The continuity equation of non-hydrostatic Saint-Venant system can be derived in a same way as in (1.4.10):

$$\frac{\partial(h\bar{u})}{\partial t} + \frac{\partial}{\partial x} \left(h\bar{u}^2 + \frac{1}{2} g h^2 \right) = -g h B_x,$$

Compared with classic Saint-Venant system, non-hydrostatic Saint-Venant system requires more discussion about pressure term p . The pressure term is not simply characterized by hydrostatic relation (1.4.13).

We can express pressure p from the third equation of the Euler equation (1.4.16),

$$\begin{aligned} \frac{\partial v}{\partial t} + \frac{\partial(uv)}{\partial x} + \frac{\partial(v^2)}{\partial y} + \frac{1}{\rho} \frac{\partial p}{\partial y} &= -g, \\ \frac{\partial p}{\partial y} &= -\rho g - \rho \left(\frac{\partial v}{\partial t} + \frac{\partial(uv)}{\partial x} + \frac{\partial(v^2)}{\partial y} \right), \end{aligned}$$

then

$$\begin{aligned} p &= p^a + \rho g(\eta - y) + \rho \int_y^\eta \left(\frac{\partial v}{\partial t} + \frac{\partial(uv)}{\partial x} + \frac{\partial(v^2)}{\partial y} \right) dy \\ &= p^a + \rho g(\eta - y) + \rho \left[\left(\int_y^\eta \frac{\partial v}{\partial t} dy \right) + \left(\int_y^\eta \frac{\partial(uv)}{\partial x} dy \right) + v_\eta^2 - v^2 \right] \\ &= p^a + \rho g(\eta - y) + \rho \left[\frac{\partial}{\partial t} \left(\int_y^\eta v dy \right) - \eta_t v_\eta + \frac{\partial}{\partial x} \left(\int_y^\eta uv dy \right) - \eta_x u_\eta v_\eta + v_\eta^2 - v^2 \right] \\ &= p^a + \rho g(\eta - y) + \rho \left[\frac{\partial}{\partial t} \left(\int_y^\eta v dy \right) + \frac{\partial}{\partial x} \left(\int_y^\eta uv dy \right) - v^2 \right]. \end{aligned} \quad (1.4.18)$$

From (1.4.14), we have hydrostatic pressure $p^h = p^a + \rho g(\eta - y)$. To make an analysis of components

of pressure p , we denote non-hydrostatic pressure p^{nh} and a new variable α , then

$$\begin{aligned} p^{nh} &:= \rho \left[\frac{\partial}{\partial t} \int_y^\eta v dy + \alpha \right], \\ \alpha &\approx \frac{\partial}{\partial x} \left(\int_y^\eta u v dy \right) - v^2, \\ p &\approx p^h + p^{nh} = p^a + \rho g(\eta - y) + \rho \left[\frac{\partial}{\partial t} \left(\int_y^\eta v dy \right) + \alpha \right]. \end{aligned} \quad (1.4.19)$$

Then we can derive the momentum equation for the non-hydrostatic Saint-Venant system below:

$$\frac{\partial}{\partial t}(h\bar{u}) + \frac{\partial}{\partial x}(h\bar{u}^2) + \frac{1}{\rho} \frac{\partial}{\partial x}(h\bar{p}) = \frac{1}{\rho} \left[-\bar{p}|_b \frac{\partial B}{\partial x} + p^a \frac{\partial \eta}{\partial x} \right], \quad (1.4.20)$$

where

$$\begin{cases} \bar{v} := -(y - B) \frac{\partial \bar{u}}{\partial x} + \frac{\partial B}{\partial x} \bar{u}, \\ \bar{p} := \frac{1}{h} \int_B^\eta p dy, \\ h\bar{p} = hp^a + \frac{1}{2}gh^2 + \frac{\partial}{\partial t} \left(\int_B^\eta \int_y^\eta \bar{v} dy \right) + \int_B^\eta \alpha dz, \\ \bar{p}|_b = p^a + gh + \frac{\partial}{\partial t} \left(\int_B^\eta \bar{v} dz \right) + \alpha|_b. \end{cases} \quad (1.4.21)$$

Note that $\int_B^\eta \alpha dz$ and $\alpha|_b$ will be to be described later.

Proof. Let's start from the second equation of the Euler equations (1.4.16),

$$\frac{\partial u}{\partial t} + u \frac{\partial u}{\partial x} + v \frac{\partial u}{\partial y} + \frac{1}{\rho} \frac{\partial p}{\partial x} = 0, \quad (1.4.22)$$

$$\frac{\partial u}{\partial t} + \frac{\partial(u^2)}{\partial x} + \frac{\partial(uv)}{\partial y} + \frac{1}{\rho} \frac{\partial p}{\partial x} = 0, \quad (1.4.23)$$

implies

$$\begin{aligned} & \int_B^\eta \frac{\partial u}{\partial t} dy + \int_B^\eta \frac{\partial(u^2)}{\partial x} dy + \int_B^\eta \frac{\partial(uv)}{\partial y} dy + \frac{1}{\rho} \int_B^\eta \frac{\partial p}{\partial x} dy = 0, \\ & \frac{\partial}{\partial t} \left(\int_B^\eta u dy \right) - \eta_t u_\eta + B_t u_b + \frac{\partial}{\partial x} \left(\int_B^\eta u^2 dy \right) - \eta_x u_\eta^2 + B_x u_b^2 \\ & + u_\eta v_\eta - u_b v_b + \frac{1}{\rho} \left[\frac{\partial}{\partial x} \left(\int_B^\eta p dy \right) - \eta_x p^a + B_x p_b \right] = 0, \\ & \frac{\partial}{\partial t} (h\bar{u}) - \eta_t u_\eta + B_t u_b + \frac{\partial}{\partial x} (h\bar{u}^2) - \eta_x u_\eta^2 + B_x u_b^2 \\ & + u_\eta v_\eta - u_b v_b + \frac{1}{\rho} \left[\frac{\partial}{\partial x} (h\bar{p}) - \eta_x p^a + B_x p_b \right] = 0, \end{aligned}$$

$$\begin{aligned}
& \frac{\partial}{\partial t}(h\bar{u}) + \frac{\partial}{\partial x}(h\bar{u}^2) + \frac{1}{\rho} \frac{\partial}{\partial x}(h\bar{p}) - \cancel{u_\eta(\eta_t + \eta_x u_\eta - v_\eta)}^0 + \cancel{u_b(B_t + B_x u_b - v_b)}^0 = \frac{1}{\rho} \left[\eta_x p^a - B_x p_b \right], \\
& \frac{\partial}{\partial t}(h\bar{u}) + \frac{\partial}{\partial x}(h\bar{u}^2) + \frac{1}{\rho} \frac{\partial}{\partial x}(h\bar{p}) = \frac{1}{\rho} \left[\eta_x p^a - B_x p_b \right].
\end{aligned} \tag{1.4.24}$$

For the term $h\bar{p}$, we can derive from (1.4.18) and (1.4.19):

$$\begin{aligned}
h\bar{p} &= \int_B^\eta p dy = \int_B^\eta \left\{ p^a + \rho g(\eta - y) + \rho \left[\frac{\partial}{\partial t} \left(\int_y^\eta v dy \right) + \alpha \right] \right\} dy \\
&= hp^a + \frac{1}{2} \rho g h^2 + \rho \int_B^\eta \frac{\partial}{\partial t} \left(\int_y^\eta v dy \right) dy + \rho \int_B^\eta \alpha dy \\
&= hp^a + \frac{1}{2} \rho g h^2 + \rho \frac{\partial}{\partial t} \left(\int_B^\eta \int_y^\eta v dy dy \right) - \cancel{\rho B_t \int_B^\eta v dy}^0 + \rho \int_B^\eta \alpha dy \\
&\approx hp^a + \frac{1}{2} \rho g h^2 + \rho \frac{\partial}{\partial t} \left(\int_B^\eta \int_y^\eta v dy dy \right) + \rho \int_B^\eta \alpha dy.
\end{aligned} \tag{1.4.25}$$

The reason $v \approx \bar{v}$ is given below. From the first equation of (1.4.16), using the Leibniz integral rule and the kinematic boundary condition at free surface in (1.4.8), we have

$$\begin{aligned}
v &= v_b + \int_B^y v_y dy \\
&= v_b - \int_B^y u_x dy \\
&= v_b - \left(\frac{\partial}{\partial x} \int_B^y u dy + B_x u_b \right) \\
&= B_t - \frac{\partial}{\partial x} \int_B^y u dy \\
&= -\frac{\partial}{\partial x} \int_B^y u dy.
\end{aligned}$$

Then using $u(x, y, t) \approx \bar{u}(x, t)$ from our assumption of shallow water mentioned above,

$$\begin{aligned}
v &\approx -\frac{\partial}{\partial x} \int_B^y \bar{u} dy \\
&= -\frac{\partial}{\partial x} \left((y - B) \bar{u} \right) \\
&= -(y - B) \frac{\partial \bar{u}}{\partial x} + \frac{\partial B}{\partial x} \bar{u} = \bar{v},
\end{aligned}$$

It's important to mention that although v and \bar{v} are small, $\bar{v}(x, y, t) = -(y - B) \frac{\partial \bar{u}}{\partial x} + \frac{\partial B}{\partial x} \bar{u}$ as an linear approximate of $v(x, y, t)$ in the variable y .

For the term p_b in (1.4.24), we can apply the formula of pressure p mentioned in (1.4.19),

$$p_b = p^a + \rho g h + \rho \left[\frac{\partial}{\partial t} \left(\int_B^\eta v dy \right) + \alpha|_b \right]. \quad (1.4.26)$$

Then use $v \approx \bar{v}$, we can approximate p_b using $\bar{p}|_b$:

$$\bar{p}|_b = p^a + \rho g h + \rho \left[\frac{\partial}{\partial t} \left(\int_B^\eta \bar{v} dy \right) + \alpha|_b \right]. \quad (1.4.27)$$

Above all, we have derived all formulas in (1.4.20) and (1.4.21). But it remains to find the explicit form for α mentioned above(in (1.4.19)).

Meanwhile, the 2-dimensional Euler equation with gravity (1.4.16) with kinematic boundary conditions (1.4.17) admits an energy equation:

$$\frac{\partial}{\partial t} \int_B^\eta \left[\frac{u^2}{2} + \frac{w^2}{2} + \frac{1}{\rho} \left(g y + p^a \right) \right] dy + \frac{\partial}{\partial x} \int_B^\eta u \left[\frac{u^2}{2} + \frac{w^2}{2} + \frac{1}{\rho} \left(g y + p \right) \right] dy = \frac{h}{\rho} \frac{\partial p^a}{\partial t}, \quad (1.4.28)$$

where LHS represents the change of kinematic and potential energy of this system divided by density and RHS represents the energy supply coming from the variations of the atmospheric pressure p^a divided by density. It's balance laws in total energy.

Proof. The time derivative of (kinetic and potential) energy in LHS of (1.4.28) is

$$\begin{aligned} & \frac{\partial}{\partial t} \int_B^\eta \left[\frac{u^2}{2} + \frac{w^2}{2} + \frac{1}{\rho} \left(g y + p^a \right) \right] dy \\ &= \eta_t \frac{u_\eta^2}{2} - B_t \frac{u_b^2}{2} + \int_B^\eta u u_t dy \\ & \quad + \eta_t \frac{v_\eta^2}{2} - B_t \frac{v_b^2}{2} + \int_B^\eta v v_t dy \\ & \quad + \frac{g}{\rho} (\eta \eta_t - B B_t) + \frac{1}{\rho} \frac{\partial (h p^a)}{\partial t} \\ &= \eta_t \frac{u_\eta^2}{2} - B_t \frac{u_b^2}{2} + \int_B^\eta u u_t dy \\ & \quad + \eta_t \frac{v_\eta^2}{2} - B_t \frac{v_b^2}{2} + \int_B^\eta v v_t dy \\ & \quad + \frac{g}{\rho} (\eta \eta_t - B B_t) + \frac{1}{\rho} \left(\eta_t p^a - B_t p^a + h \frac{\partial p^a}{\partial t} \right). \end{aligned}$$

The spatial derivative of (kinetic and potential) energy flux in LHS of (1.4.28) is

$$\frac{\partial}{\partial x} \int_B^\eta u \left[\frac{u^2}{2} + \frac{v^2}{2} + \frac{1}{\rho} \left(g y + p \right) \right] dy$$

$$\begin{aligned}
&= \eta_x \frac{u_\eta^3}{2} - B_x \frac{u_b^3}{2} + \int_B \left(\frac{1}{2} u^2 u_x + u^2 u_x \right) dy \\
&\quad + \eta_x \frac{u_\eta v_\eta^2}{2} - B_x \frac{u_b v_b^2}{2} + \int_B \left(\frac{u_x v^2}{2} + u v v_x \right) dy \\
&\quad + \frac{g}{\rho} \left(\eta_x u_\eta \eta - B_x u_b B + \int_B y u_x dy \right) \\
&\quad + \frac{1}{\rho} \left[\eta_x u_\eta p^a - B_x u_b p_b + \int_B \left(u_x p + u p_x \right) dy \right] \\
&= \eta_x \frac{u_\eta^3}{2} - B_x \frac{u_b^3}{2} + \int_B \left(u^2 u_x \right) dy - \frac{1}{2} \int_B u^2 dv \\
&\quad + \eta_x \frac{u_\eta v_\eta^2}{2} - B_x \frac{u_b v_b^2}{2} + \int_B \left(u v v_x \right) dy - \frac{1}{2} \int_B v^2 dv \\
&\quad + \frac{g}{\rho} \left(\eta \eta_x u_\eta - B B_x u_b - \int_B y dv \right) \\
&\quad + \frac{1}{\rho} \left[\eta_x u_\eta p^a - B_x u_b p_b + \int_B (u p_x) dy - \int_B p dv \right] \\
&= \eta_x \frac{u_\eta^3}{2} - B_x \frac{u_b^3}{2} + \int_B \left(u^2 u_x \right) dy - \frac{1}{2} u_\eta^2 v_\eta + \frac{1}{2} u_b^2 v_b + \int_B v u u_y dy \\
&\quad + \eta_x \frac{u_\eta v_\eta^2}{2} - B_x \frac{u_b v_b^2}{2} + \int_B \left(u v v_x \right) dy - \frac{1}{2} v_\eta^3 + \frac{1}{2} v_b^3 + \int_B v^2 v_y dy \\
&\quad + \frac{g}{\rho} \left(\eta \eta_x u_\eta - B B_x u_b - \eta v_\eta + B v_b + \int_B v dy \right) \\
&\quad + \frac{1}{\rho} \left[\eta_x u_\eta p^a - B_x u_b p_b + \int_B (u p_x) dy - p^a v_\eta + p^b v_b + \int_B v p_y dy \right].
\end{aligned}$$

Combine two terms in the LHS, we have

$$\begin{aligned}
&\frac{\partial}{\partial t} \int_B \left[\frac{u^2}{2} + \frac{w^2}{2} + \frac{1}{\rho} \left(g y + p^a \right) \right] dy + \frac{\partial}{\partial x} \int_B u \left[\frac{u^2}{2} + \frac{v^2}{2} + \frac{1}{\rho} \left(g y + p \right) \right] dy \\
&= \frac{1}{2} u_\eta^2 \left(\eta_t + \eta_x u_\eta - v_\eta \right) - \frac{1}{2} u_b^2 \left(B_t + B_x u_b - v_b \right) \\
&\quad + \frac{1}{2} v_\eta^2 \left(\eta_t + \eta_x u_\eta - v_\eta \right) - \frac{1}{2} v_b^2 \left(B_t + B_x u_b - v_b \right) \\
&\quad + \frac{g \eta}{\rho} \left(\eta_t + \eta_x u_\eta - v_\eta \right) - \frac{g B}{\rho} \left(B_t + B_x u_b - v_b \right) \\
&\quad + \frac{p^a}{\rho} \left(\eta_t + \eta_x u_\eta - v_\eta \right) - \frac{p^a}{\rho} \left(B_t + B_x u_b - v_b \right) + \frac{h}{\rho} \frac{\partial p^a}{\partial t} \\
&\quad + \int_B \left[u \left(u_t + u u_x + v u_y + p_x \right) + v \left(v_t + u v_x + v v_y + p_y \right) \right] dy + \frac{g}{\rho} \int_B v dy
\end{aligned}$$

$$= \frac{h}{\rho} \frac{\partial p^a}{\partial t}. \quad (1.4.29)$$

Thus, we have proved the energy equation for non-hydrostatic equation in (1.4.28).

A similar energy equation for the depth-averaged non-hydrostatic Saint-Venant system (1.4.20) with (1.4.21) exists. The non-hydrostatic Saint-Venant system satisfies the following energy balance equation:

$$\begin{aligned} \frac{\partial}{\partial t} \int_B \left[\frac{\bar{u}^2}{2} + \frac{\bar{w}^2}{2} + \frac{1}{\rho} \left(g y + p^a \right) \right] dy + \frac{\partial}{\partial x} \left[\frac{h \bar{u}^2}{2} + h \bar{p} + \frac{1}{\rho} \left(\frac{\eta^2 - B^2}{2} \right) \right] &= \frac{h}{\rho} \frac{\partial p^a}{\partial t} \\ &+ \frac{1}{2} \frac{\partial \eta}{\partial t} (\bar{v}|_\eta)^2 + \int_B^\eta \bar{v} \frac{\partial \alpha}{\partial y} dy. \end{aligned} \quad (1.4.30)$$

For details, we refer readers to [Bri11; Bri08]. These 2 systems should admit same energy condition, which implies:

$$\frac{1}{2} \frac{\partial \eta}{\partial t} (\bar{v}|_\eta)^2 + \int_B^\eta \bar{v} \frac{\partial \alpha}{\partial y} dy = 0. \quad (1.4.31)$$

From the analysis of (1.4.19), we have

$$\begin{aligned} \alpha &\approx \frac{\partial}{\partial x} \left(\int_y^\eta u v dy \right) - v^2 \\ \alpha|_\eta &= \lim_{y \rightarrow \eta} \frac{\partial}{\partial x} \left(\int_y^\eta u v dy \right) - v^2 \\ &= \lim_{y \rightarrow \eta} \left[\frac{\partial}{\partial x} \left(\int_y^\eta u v dy \right) - v^2 \right] \\ &= \lim_{y \rightarrow \eta} \left[\eta_x u_\eta v_\eta + \left(\int_y^\eta \frac{\partial u v}{\partial x} dy \right) - v_\eta^2 \right] \\ &= \lim_{y \rightarrow \eta} \left[-\eta_t v_\eta - v_\eta^2 + \left(\int_y^\eta \frac{\partial u v}{\partial x} dy \right) \right] \\ &= -\frac{\partial \eta}{\partial t} v_\eta \\ &\approx -\frac{\partial \eta}{\partial t} \bar{v}|_\eta. \end{aligned}$$

Above all, we can set equations for α ,

$$\begin{cases} \frac{1}{2} \frac{\partial \eta}{\partial t} (\bar{v}|_\eta)^2 + \int_B^\eta \bar{v} \frac{\partial \alpha}{\partial y} dy = 0 \\ \alpha|_\eta = -\frac{\partial \eta}{\partial t} \bar{v}|_\eta. \end{cases} \quad (1.4.32)$$

If we denote

$$\beta := -\frac{\partial \alpha}{\partial y}, \quad (1.4.33)$$

Then from (1.4.19), the third equation of (1.4.16) and $\bar{u} \approx u$, $\bar{v} \approx v$ (the assumption of shallow water), we have

$$\begin{aligned}
\beta &= -\frac{\partial \alpha}{\partial y} \approx -\frac{\partial}{\partial y} \left\{ \frac{(p-p^a)}{\rho} - g(\eta-y) - \left[\frac{\partial}{\partial t} \left(\int_y^\eta v dy \right) \right] \right\} \\
&= -\frac{1}{\rho} \frac{\partial p}{\partial y} + g + \frac{\partial}{\partial t} \left[\frac{\partial}{\partial y} \int_y^\eta v dy \right] \\
&= -\frac{1}{\rho} \frac{\partial p}{\partial y} + g - \rho \frac{\partial v}{\partial t} \\
&= u \frac{\partial v}{\partial x} + v \frac{\partial v}{\partial y} \\
&\approx \bar{u} \frac{\partial \bar{v}}{\partial x} + \bar{v} \frac{\partial \bar{v}}{\partial y}.
\end{aligned}$$

Since \bar{v} is linear in y , it's natural to assume

$$\beta = a_1(x, t) \cdot (y - B) + a_2(x, t). \quad (1.4.34)$$

From the first equation of (1.4.32),

$$\begin{aligned}
&\frac{1}{2} \frac{\partial \eta}{\partial t} (\bar{w}|_\eta) (-h \frac{\partial \bar{u}}{\partial x} + \frac{\partial B}{\partial x} \bar{u}) - \int_B^\eta \left[-(y-B) \frac{\partial \bar{u}}{\partial x} + \frac{\partial B}{\partial x} \bar{u} \right] \left[a_1(y-B) + a_2 \right] dy = 0, \\
&\frac{\partial \bar{u}}{\partial x} \left[-\frac{1}{2} \frac{\partial \eta}{\partial t} \bar{w}_\eta h + a_1 \frac{h^3}{3} + a_2 \frac{h^2}{2} \right] + \frac{\partial B}{\partial x} \bar{u} \left[\frac{1}{2} \frac{\partial \eta}{\partial t} \bar{w}_\eta - a_1 \frac{h^2}{2} - a_2 h \right] = 0.
\end{aligned}$$

Then a_1 and a_2 can be derived:

$$a_1 = \frac{3\bar{w}_\eta}{h^2} \frac{\partial \eta}{\partial t}, \quad a_2 = -\frac{\bar{w}_\eta}{h} \frac{\partial \eta}{\partial t}. \quad (1.4.35)$$

And using the formula for α to satisfy (1.4.32):

$$\alpha = -\frac{\partial \eta}{\partial t} \bar{w}_\eta + \int_y^\eta \beta dy, \quad (1.4.36)$$

the depth-integrated non-hydrostatic Saint-Venant system (1.4.20) and (1.4.21) satisfies the following energy equation:

$$\frac{\partial}{\partial t} \int_B^\eta \left[\frac{\bar{u}^2}{2} + \frac{\bar{w}^2}{2} + \frac{1}{\rho} \left(g y + p^a \right) \right] dy + \frac{\partial}{\partial x} \left[\frac{h \bar{u}^2}{2} + h \bar{p} + \frac{1}{\rho} \left(\frac{\eta^2 - B^2}{2} \right) \right] = \frac{h}{\rho} \frac{\partial p^a}{\partial t}. \quad (1.4.37)$$

And α related values are ready for (1.4.21):

$$\int_B^\eta \alpha dy = \frac{1}{2} \frac{\partial \eta}{\partial t} h \bar{w}_\eta, \quad \alpha|_b = -\frac{1}{2} \frac{\partial \eta}{\partial t} \bar{w}_\eta. \quad (1.4.38)$$

Then the non-hydrostatic Saint-Venant system is derived:

$$\begin{cases} h_t + (hu)_x = 0, \\ (hu)_t + M_t + \left(hu^2 + \frac{g}{2}h^2\right)_x + N = -ghB_x + p^a w_x, \end{cases} \quad (1.4.39)$$

with

$$M = \left(-\frac{1}{3}h^3u_x + \frac{1}{2}h^2B_xu\right)_x + B_x\left(-\frac{1}{2}h^2u_x + B_xhu\right), \quad (1.4.40)$$

and

$$N = \left[(h^2)_t(hu_x - B_xu)\right]_x + 2B_xh_t(hu_x - B_xu) - B_{xt}\left(-\frac{1}{2}h^2u_x + B_xhu\right). \quad (1.4.41)$$

When M and N are ignored, (1.4.39) reduces to classic Saint-Venant system((1.4.15)). In chapter 2, we will propose a central-upwind scheme to solve this non-hydrostatic Saint-Venant system and discuss the effects of M and N in the long-time propagation and on-shore arrival of tsunami-like waves.

1.4.3 Steady States of Saint-Venant System

Steady state solutions are solutions that do not change in time. In many physical applications, solutions of a system are small perturbations of the steady states. These perturbations may be smaller than the size of the numerical truncation error on a coarse grid. Capturing these perturbations is one of the major interests and difficulties of solving different systems of PDEs. To overcome this difficulty, one can use a very fine grid, but in many physically relevant situations, it might be computationally unaffordable or time-consuming.

A numerical scheme is called well-balanced if it can preserve a (particular) steady-state solution exactly(without any numerical error). Different well-balanced schemes will be further discussed in chapter 2 and 3.

The classic Saint-Venant system (1.4.15) and non-hydrostatic Saint-Venant system (1.4.39) have steady state solutions. In this section, we derive some of their steady state solutions.

For the classic Saint-Venant system, since steady state doesn't change in time, we have (1.4.15) reduced to

$$\begin{cases} (hu)_x = 0, \\ \left(hu^2 + \frac{g}{2}h^2\right)_x = -ghB_x. \end{cases} \quad (1.4.42)$$

From the first equation of (1.4.42), we have

$$hu \equiv \text{constant}. \quad (1.4.43)$$

For the second equation of (1.4.42), we have

$$\begin{aligned} \cancel{(hu)_x} \bar{u} + (hu)u_x + gh h_x &= -gh B_x, \\ uu_x + g(h+B)_x &= 0, \\ \left[\frac{u^2}{2} + g(h+B) \right]_x &= 0. \end{aligned}$$

This implies that

$$\frac{u^2}{2} + g(h+B) \equiv \text{constant}. \quad (1.4.44)$$

So the classic Saint-Venant system (1.4.15) admits steady state solutions satisfying

$$hu \equiv \text{constant}, \quad \frac{u^2}{2} + g(h+B) \equiv \text{constant}. \quad (1.4.45)$$

One of the most important steady states satisfying (1.4.45) is the stationary steady state. It is also called the 'lake-at-rest' solution that describes a motionless lake:

$$u \equiv 0, \quad w := h+B \equiv \text{constant}. \quad (1.4.46)$$

For non-hydrostatic Saint-Venant system (1.4.39), the steady state solution satisfies

$$\begin{cases} (hu)_x = 0, \\ \left[hu^2 + \frac{1}{2}gh^2 \right]_x + N = -gh B_x, \end{cases} \quad (1.4.47)$$

with

$$N(h, u) = \left((h^2)_t (hu_x - B_x u) \right)_x + 2B_x h_t (hu_x - B_x u).$$

Here, $N = 0$ for its assumption of being steady state solutions. So (1.4.47) becomes

$$\begin{cases} (hu)_x = 0, \\ \left[hu^2 + \frac{1}{2}gh^2 \right]_x = -gh B_x, \end{cases} \quad (1.4.48)$$

which is the same as (1.4.42).

We have same steady state solution (1.4.45) and stationary steady state solution (1.4.46) for non-hydrostatic Saint-Venant system (1.4.39).

1.5 Compressible Euler Equation for Ideal Gas

In chapter 3, we will discuss atmospheric flow equations with gravity. It has the following form:

$$\begin{cases} \rho_t + (\rho u)_x + (\rho v)_y = 0, \\ (\rho u)_t + (\rho u^2 + p)_x + (\rho uv)_y = 0, \\ (\rho v)_t + (\rho vu)_x + (\rho v^2 + p)_y = -\rho g, \\ (\rho \theta)_t + (\rho \theta u)_x + (\rho \theta v)_y = 0, \end{cases} \quad (1.5.1)$$

where θ is potential energy and equation of state is

$$P = (\rho \theta)^\gamma. \quad (1.5.2)$$

Here, we provide two approaches to derive this system.

In the first approach, we can start from the multi-dimensional Euler equation with gravity:

$$\begin{cases} \frac{\partial}{\partial t} \rho + (\rho u)_x + (\rho v)_y = 0, \\ \frac{\partial \rho u}{\partial t} + (\rho u^2 + p)_x + (\rho uv)_y = 0, \\ \frac{\partial \rho v}{\partial t} + (\rho vu)_x + (\rho v^2 + p)_y = -\rho g, \\ \frac{\partial E}{\partial t} + [(E + p)u]_x + [(E + p)v]_y = -\rho v g, \end{cases} \quad (1.5.3)$$

with total energy $E = \frac{1}{2} \rho (u^2 + v^2) + \frac{p}{\gamma - 1}$.

The (fourth) energy balance equation of classic Euler equation (1.5.3) is expressed in terms of total energy E . But we can express the conservation of energy in terms of potential temperature, especially in atmospheric flow equations with gravity.

The equation of state of an ideal gas:

$$p = (\rho \theta)^\gamma, \quad (1.5.4)$$

where p is pressure, θ is potential temperature and $\gamma = 1.4$ is the specific heat ratio.

Let's first derive the identity below using only the first 3 equations of (1.5.3):

$$\left[\frac{1}{2} \rho (u^2 + v^2) \right]_t + p_x u + \left[\frac{1}{2} \rho (u^2 + v^2) u \right]_x + p_y v + \left[\frac{1}{2} \rho (u^2 + v^2) v \right]_y = -\rho v g. \quad (1.5.5)$$

Proof:

$$\begin{aligned}
& [\frac{1}{2}\rho(u^2 + v^2)]_t + p_x u + [\frac{1}{2}\rho(u^2 + v^2)u]_x + p_y v + [\frac{1}{2}\rho(u^2 + v^2)v]_y \\
&= \frac{1}{2}[(\rho u)_t u + \rho u u_t + (\rho v)_t v + \rho v v_t] + p_x u + [\frac{1}{2}\rho(u^2 + v^2)u]_x + p_y v + [\frac{1}{2}\rho(u^2 + v^2)v]_y \\
&= \frac{1}{2}[(\rho u)_t u + (\rho u)_t u - \rho_t u^2 + (\rho v)_t v + (\rho v)_t v - \rho_t v^2] + p_x u + [\frac{1}{2}\rho(u^2 + v^2)u]_x + p_y v + [\frac{1}{2}\rho(u^2 + v^2)v]_y \\
&= (\rho u)_t u + (\rho v)_t v - \frac{1}{2}\rho_t[u^2 + v^2] + p_x u + [\frac{1}{2}\rho(u^2 + v^2)u]_x + p_y v + [\frac{1}{2}\rho(u^2 + v^2)v]_y \\
&= (\rho u)_t u + p_x u + (\rho v)_t v + p_y v - \frac{1}{2}\rho_t[u^2 + v^2] + [\frac{1}{2}\rho(u^2 + v^2)u]_x + [\frac{1}{2}\rho(u^2 + v^2)v]_y \\
&= -(\rho u^2)_x u - (\rho u v)_y u - \rho v g - (\rho u v)_x v - (\rho v^2)_y v \\
&\quad - \frac{1}{2}\rho_t[u^2 + v^2] + [\frac{1}{2}\rho(u^2 + v^2)u]_x + [\frac{1}{2}\rho(u^2 + v^2)v]_y \\
&= -\rho v g - (\rho u^2)_x u - (\rho u v)_y u - (\rho u v)_x v - (\rho v^2)_y v + \frac{1}{2}[(\rho u)_x + (\rho v)_y][u^2 + v^2] \\
&\quad + \frac{1}{2}[\rho(u^2 + v^2)u]_x + \frac{1}{2}[\rho(u^2 + v^2)v]_y \\
&= -\rho v g - \rho_x u^3 - 2\rho u^2 u_x - \rho_y u^2 v - \rho u_y v u - \rho u^2 v_y \\
&\quad - \rho_x u v^2 - \rho u_x v^2 - \rho u v_x v - \rho_y v^3 - 2\rho v^2 v_y \\
&\quad + \frac{1}{2}[\rho_x u + \rho u_x + \rho_y v + \rho v_y][u^2 + v^2] \\
&\quad + \frac{1}{2}[\rho_x u^3 + \rho 3u^2 u_x + \rho_x v^2 u + 2\rho v v_x u + \rho v^2 u_x] \\
&\quad + \frac{1}{2}[\rho_y u^2 v + 2\rho u u_y v + \rho u^2 v_y + \rho_y v^3 + 3\rho v^2 v_y] \\
&= -\rho v g - \rho_x u^3 - 2\rho u^2 u_x - \rho_y u^2 v - \rho u_y v u - \rho u^2 v_y \\
&\quad - \rho_x u v^2 - \rho u_x v^2 - \rho u v_x v - \rho_y v^3 - 2\rho v^2 v_y \\
&\quad + \frac{1}{2}[\rho_x u^3 + \rho u_x u^2 + \rho_y v u^2 + \rho v_y u^2 + \rho_x u v^2 + \rho u_x v^2 + \rho_y v^3 + \rho v_y v^2] \\
&\quad + \frac{1}{2}[\rho_x u^3 + 3\rho u^2 u_x + \rho_x v^2 u + 2\rho v v_x u + \rho v^2 u_x] \\
&\quad + \frac{1}{2}[\rho_y u^2 v + 2\rho u u_y v + \rho u^2 v_y + \rho_y v^3 + 3\rho v^2 v_y] \\
&= -\rho v g.
\end{aligned}$$

□

Thus we can derive the fourth equation of (1.5.1) with potential θ from (1.5.3):

$$\begin{aligned}
& \frac{\partial E}{\partial t} + [(E + p)u]_x + [(E + p)v]_y = -\rho v g, \\
& \frac{\partial}{\partial t} \left[\frac{1}{2} \rho (u^2 + v^2) + \frac{p}{\gamma - 1} \right] + \left[\left(\frac{1}{2} \rho (u^2 + v^2) + \frac{\gamma p}{\gamma - 1} \right) u \right]_x + \left[\left(\frac{1}{2} \rho (u^2 + v^2) + \frac{\gamma p}{\gamma - 1} \right) v \right]_y = -\rho v g, \\
& \frac{\partial}{\partial t} \left[\frac{1}{2} \rho (u^2 + v^2) + \frac{p}{\gamma - 1} \right] + \left[\left(\frac{1}{2} \rho (u^2 + v^2) + \frac{\gamma p}{\gamma - 1} \right) u \right]_x + \left[\left(\frac{1}{2} \rho (u^2 + v^2) + \frac{\gamma p}{\gamma - 1} \right) v \right]_y \\
& - \left[\frac{1}{2} \rho (u^2 + v^2) \right]_t - p_x u - \left[\frac{1}{2} \rho (u^2 + v^2) u \right]_x - p_y v - \left[\frac{1}{2} \rho (u^2 + v^2) v \right]_y = -\rho v g + \rho v g, \\
& \left(\frac{p}{\gamma - 1} \right)_t + \left(\frac{p}{\gamma - 1} \right)_x u + \left(p + \frac{p}{\gamma - 1} \right) u_x + \left(\frac{p}{\gamma - 1} \right)_y v + \left(p + \frac{1}{\gamma - 1} p \right) v_y = 0, \\
& p_t + p_x u + \gamma p u_x + p_y v + \gamma p v_y = 0, \\
& \gamma (\rho \theta)^{\gamma - 1} (\rho \theta)_t + \gamma (\rho \theta)^{\gamma - 1} (\rho \theta)_x u + \gamma (\rho \theta)^{\gamma - 1} \rho \theta u_x + \gamma (\rho \theta)^{\gamma - 1} (\rho \theta)_y v + \gamma (\rho \theta)^{\gamma - 1} \rho \theta v_y = 0, \\
& (\rho \theta)_t + (\rho \theta)_x u + \rho \theta u_x + (\rho \theta)_y v + \rho \theta v_y = 0, \\
& (\rho \theta)_t + (\rho \theta)_x u + (\rho \theta)_y v = 0.
\end{aligned}$$

In the second approach, we can start from an isentropic process. It's a thermodynamics process that is both adiabatic and reversible. If a material undergoes a change in its physical state like pressure, volume or temperature without any heat being added to it or withdrawn from it, the change is called adiabatic. Here, we focus on its property of being adiabatic.

For an adiabatic transformation,

$$dq = 0. \quad (1.5.6)$$

Here $d(\cdot)$ indicates differentiation or small change and q means heat. So no heat change in this system.

From the first law of thermodynamics we have

$$dq = c_p dT - \alpha dp, \quad (1.5.7)$$

where, c_p is heat capacity at constant pressure, T is temperature, p is pressure, and α is volume. Using the gas equation $p\alpha = RT$, we have

$$c_p dT - \frac{RT}{p} dp = 0 \text{ or } \frac{dT}{T} = \frac{R}{c_p} \frac{dp}{p}. \quad (1.5.8)$$

The *potential temperature* θ of an air parcel is the temperature that the parcel of air would have if it were expanded or compressed adiabatically from its existing pressure p to a standard(ground)

pressure of p_0 . We then can derive:

$$\begin{aligned}\int_{\theta}^T \frac{dT}{T} &= \frac{R}{c_p} \int_{p_0}^p \frac{dp}{p}, \\ \ln\left(\frac{T}{\theta}\right) &= \frac{R}{c_p} \ln\left(\frac{p}{p_0}\right), \\ \theta &= T \left(\frac{p}{p_0}\right)^{-\kappa},\end{aligned}$$

where $\kappa = \frac{R}{c_p}$. Then

$$\frac{dq}{T} = c_p \frac{dT}{T} - R \frac{dp}{p} = c_p \frac{d\theta}{\theta}, \quad (1.5.9)$$

indicates $d\theta = 0$ for the diabatic process. We have material derivative of potential temperature θ

$$\frac{D\theta}{Dt} := \frac{\partial\theta}{\partial t} + u \frac{\partial\theta}{\partial x} + v \frac{\partial\theta}{\partial y} = 0. \quad (1.5.10)$$

Thus we can derive $(\rho\theta)_t + (\rho\theta u)_x + (\rho\theta v)_y = 0$.

Above all, the 2-dimensional compressible Euler equation for ideal gas using potential temperature:

$$\begin{cases} \rho_t + (\rho u)_x + (\rho v)_y = 0, \\ (\rho u)_t + (\rho u^2 + p)_x + (\rho uv)_y = 0, \\ (\rho v)_t + (\rho vu)_x + (\rho v^2 + p)_y = -\rho g, \\ (\rho\theta)_t + (\rho\theta u)_x + (\rho\theta v)_y = 0. \end{cases} \quad (1.5.11)$$

The numerical scheme and simulations based on this model will be discussed in chapter 3.

1.6 Numerical Methods

1.6.1 Finite Volume Method

Finite volume methods are among the most efficient algorithms to solve PDEs. They enjoy the advantages of capturing numerical solutions in an accurate and non-oscillatory manner. The reason is that finite volume method is a way of representing and evaluating PDEs by introducing volume(cell) average values and numerical(edge) flux instead of point value in finite difference methods. Thus it can represent the fluxes near adjacent volumes(cells) and further extend its applications to unstructured meshes at ease.

For simplicity, we start with the scalar conservation law in (1.2.2),

$$\frac{\partial}{\partial t} q(x, t) + \frac{\partial}{\partial x} F(q(x, t)) = 0. \quad (1.6.1)$$

Here, q is a scalar known function with spatial and time variables, x and t , $F(q(x, t))$ is the flux

function. It can be easily written in an integral form:

$$\frac{d}{dt} \int_a^b q(x, t) dx + F(q(b, t)) - F(q(a, t)) = 0. \quad (1.6.2)$$

When this interval is changed to a cell $x \in [x_{j-\frac{1}{2}}, x_{j+\frac{1}{2}}]$ when $t = t_n$, we can define volume(cell) average

$$\bar{q}_j^n := \frac{1}{\Delta x} \int_{x_{j-\frac{1}{2}}}^{x_{j+\frac{1}{2}}} q(x, t^n) dx, \quad (1.6.3)$$

If we integrate the above integral form of conservation laws in time from t^n to t^{n+1} and divide whole equation by Δx , we have

$$\frac{1}{\Delta x} \left[\int_{x_{j-\frac{1}{2}}}^{x_{j+\frac{1}{2}}} q(x, t^{n+1}) dx - \int_{x_{j-\frac{1}{2}}}^{x_{j+\frac{1}{2}}} q(x, t^n) dx \right] + \frac{1}{\Delta x} \left[\int_{t^n}^{t^{n+1}} F(q(x_{j+\frac{1}{2}}, t)) dt - \int_{t^n}^{t^{n+1}} F(q(x_{j-\frac{1}{2}}, t)) dt \right] = 0, \quad (1.6.4)$$

and it can be rewritten as

$$\bar{q}_j^{n+1} - \bar{q}_j^n = -\frac{1}{\Delta x} \left[\int_{t^n}^{t^{n+1}} F(q(x_{j+\frac{1}{2}}, t)) dt - \int_{t^n}^{t^{n+1}} F(q(x_{j-\frac{1}{2}}, t)) dt \right], \quad (1.6.5)$$

it can be further simplified by introducing numerical(edge) flux:

$$F_{j+\frac{1}{2}}^n = \frac{1}{\Delta t} \int_{t^n}^{t^{n+1}} F(q(x_{j+\frac{1}{2}}, t)) dt, \quad (1.6.6)$$

Finally this differential equation becomes the fully-discrete form of finite volume method for general conservation law,

$$\bar{q}_j^{n+1} - \bar{q}_j^n = -\frac{\Delta t}{\Delta x} [F_{j+\frac{1}{2}}^n - F_{j-\frac{1}{2}}^n], \quad (1.6.7)$$

Another important form is the semi-discrete form of the finite volume method for general conservation law

$$\frac{d\bar{q}_j^n}{dt} + \frac{1}{\Delta x} [F_{j+\frac{1}{2}}^n - F_{j-\frac{1}{2}}^n] = 0, \quad (1.6.8)$$

which we will discuss later.

Deriving a stable approximation of the numerical flux $F_{j+\frac{1}{2}}^n$ in (1.6.6) is necessary. Note that (1.6.7) involves cell averages on the LHS of the equation and numerical fluxes to be calculated on the right. Numerical fluxes in (1.6.6) are time integrals of the flux function from time t^n to t^{n+1} that require an appropriate approximation of the evolution of $q(x_{j+\frac{1}{2}}, t)$. Since this time integral contain the numerical solution at t^{n+1} , numerical flux need to be estimated consistent and stable.

In Figure 1.6.1, the points in the numerical flux $F_{j+\frac{1}{2}}^n$ is $\{x_{j+\frac{1}{2}}\} \times [t^n, t^{n+1}]$. Tracing back characteristic of these points to the line $t = t^n$, stability requires the domain of dependence is fully

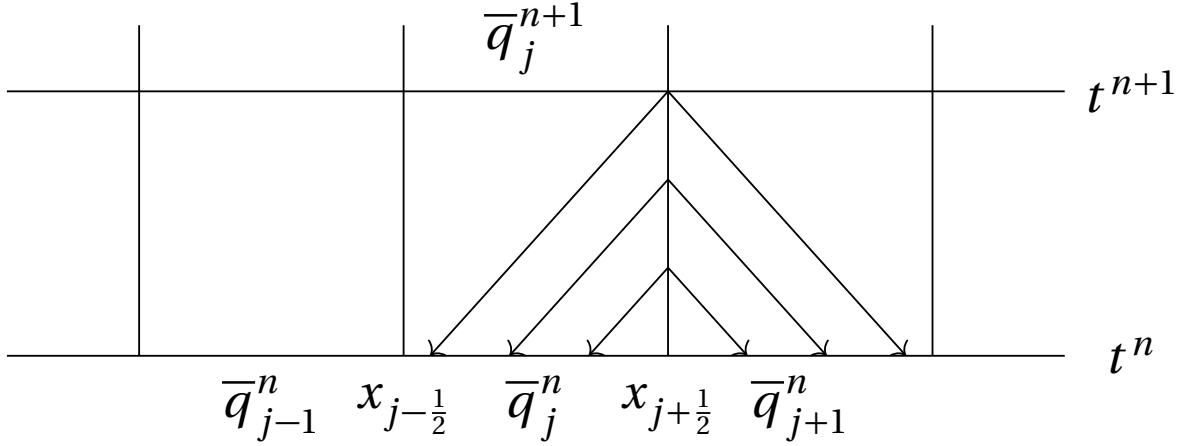


Figure 1.6.1 Domain of Dependence from Different Cells

contained in adjacent cells C_j and C_{j+1} . This process is usually denoted as:

$$\hat{F}_{j+\frac{1}{2}}(\bar{q}_j^n, \bar{q}_{j+1}^n) = F_{j+\frac{1}{2}}^n. \quad (1.6.9)$$

If $\bar{q}_j^n = \bar{q}_j^n \equiv \text{constant} := c$, it's easy to test consistency by checking

$$\hat{F}_{j+\frac{1}{2}}(c, c) = F(c). \quad (1.6.10)$$

In order for the designed numerical scheme to be stable, it is necessary to introduce the Courant-Friedrichs-Lewy (CFL) condition here.

For one-dimensional advection equation:

$$\frac{\partial q}{\partial t} + a \frac{\partial q}{\partial x} = 0, \quad (1.6.11)$$

where numerical flux $F(q) = aq$ and finite wave speed a . The CFL condition then has the following form:

$$C = \frac{a \Delta t}{\Delta x} \leq 1, \quad (1.6.12)$$

where C is the Courant number, typically it's less than 1.

For multi-dimensional cases,

$$\frac{\partial \mathbf{q}}{\partial t} + \nabla_x \cdot \mathbf{F}(\mathbf{q}) = 0, \quad (1.6.13)$$

where λ_i is i -th eigenvalues of Jacobian matrix $\frac{\partial \mathbf{F}}{\partial \mathbf{q}}$, the Courant number

$$C = \Delta t \max_i \frac{|\lambda_i|}{\Delta x_i} \quad (1.6.14)$$

should be restricted to determine time step Δt in computation.

1.6.2 Semi-Discrete Central-Upwind Scheme

Godunov-type schemes offer a framework to solve finite volume methods. In Sergei Godunov's pioneer work [God59], he approximated numerical solution at t^n as piecewise constant over the grid volumes(cells), then evolved the solution by solving local Riemann problems at the cell interfaces(edges) exactly and eventually projected the solution at t^{n+1} by averaging state variables obtained in Riemann problems. One of his great contributions is that his work can be extended for a general nonlinear system of equations in an upwind style. Godunov-type schemes are also referred to as **REA** algorithm(1d as an example):

1. **Reconstruct** a piecewise polynomial function $\tilde{q}(x, t^n)$ from cell averages \bar{q}_j^n in cell $[x_{j-\frac{1}{2}}, x_{j+\frac{1}{2}}]$ at time t^n .

If the scheme is first order, a piecewise constant reconstruction is enough:

$$\tilde{q}(x, t^n) = \bar{q}_j^n, \quad x \in [x_{j-\frac{1}{2}}, x_{j+\frac{1}{2}}]. \quad (1.6.15)$$

If the scheme is 2nd order, a piecewise linear reconstruction is enough:

$$\tilde{q}(x, t^n) = \bar{q}_j^n + (q_x)_j^n (x - x_j), \quad x \in [x_{j-\frac{1}{2}}, x_{j+\frac{1}{2}}]. \quad (1.6.16)$$

2. **Evolve** the exact or approximate Riemann solution at cell interfaces $x_{j+\frac{1}{2}}$ and then compute numerical fluxes and update hyperbolic equations(like in (1.6.7) and (1.6.8)).
3. **Average** the piecewise polynomial function $\tilde{q}(x, t^{n+1})$ over $[x_{j-\frac{1}{2}}, x_{j+\frac{1}{2}}]$ to obtain new cell averages \bar{q}_j^{n+1} :

$$\bar{q}_j^{n+1} = \int_{x_{j-\frac{1}{2}}}^{x_{j+\frac{1}{2}}} \tilde{q}(x, t^{n+1}) dx. \quad (1.6.17)$$

Noted that the first and third steps can be treated as a same step, sometimes it is called a projection stage leaving the second step as evolution stage.

Semi-discrete finite volume method in (1.6.8) with numerical flux introduced in (1.6.6),

$$\begin{aligned} \frac{d\bar{q}_j^n}{dt} + \frac{1}{\Delta x} [F_{j+\frac{1}{2}}^n - F_{j-\frac{1}{2}}^n] &= 0, \\ F_{j+\frac{1}{2}}^n &= \frac{1}{\Delta t} \int_{t^n}^{t^{n+1}} F(q(x_{j+\frac{1}{2}}, t)) dt. \end{aligned} \quad (1.6.18)$$

Godunov proposed classical upwind schemes in his work [God59]. Figure 1.6.2(a) illustrates, in upwind schemes, the space-time control volume is $[x_{j-\frac{1}{2}}, x_{j+\frac{1}{2}}] \times [t^n, t^{n+1}]$. One need to calculate or approximate the integral of the flux function at cell interface $x_{j+\frac{1}{2}}$. If the reconstruction is piecewise constant or linear, the solution $q(x, t)$ at interfaces $(x_{j\pm\frac{1}{2}}, t^n)$ is likely to be discontinues. Thus, an exact or approximate Riemann solver can be applied here. The advantages of upwind schemes are

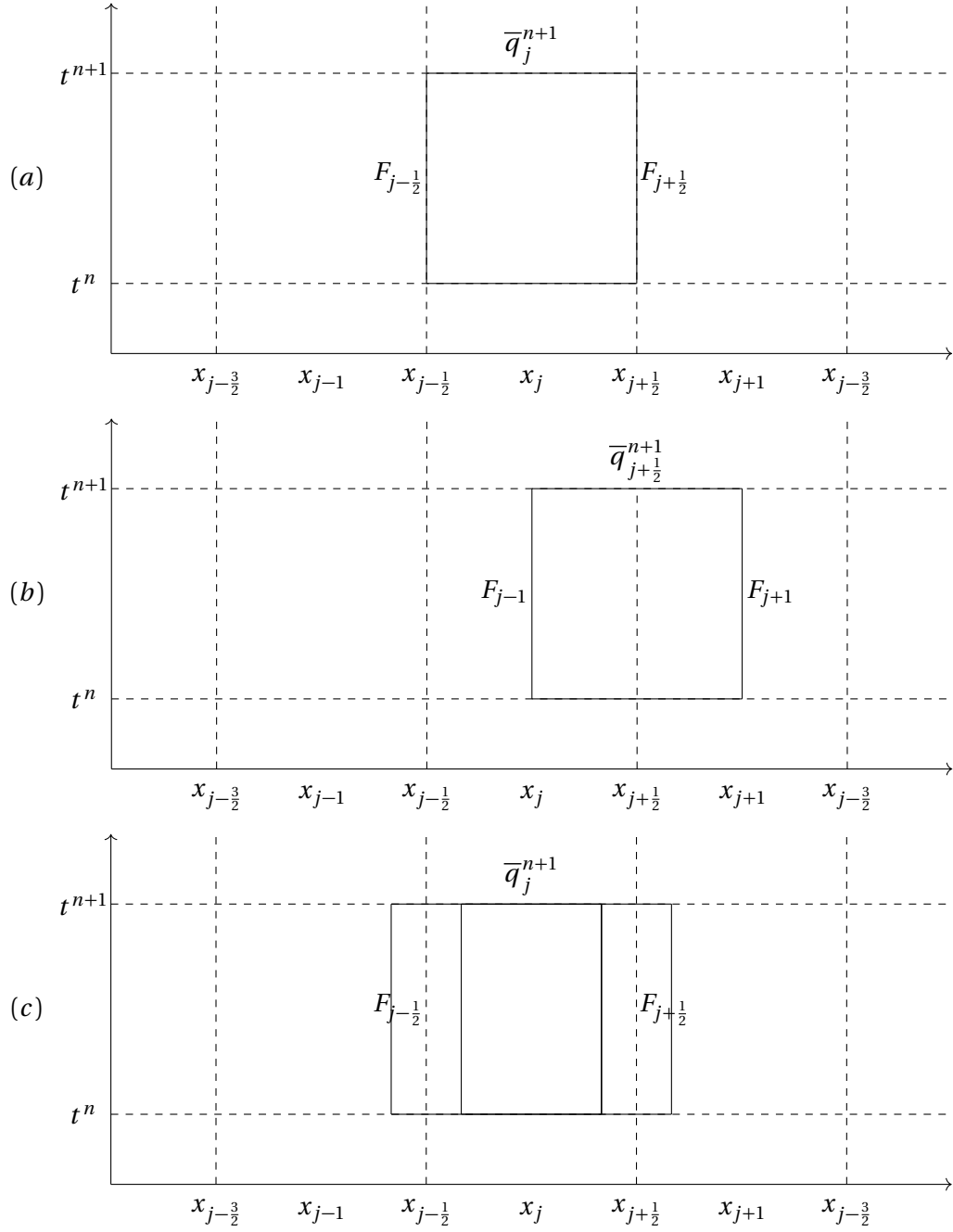


Figure 1.6.2 (a) Upwind control volume (b) Central control volume (c) Central-upwind control volumes

highly accurate, less diffusive and dissipative than central schemes(they will be mentioned later). The disadvantages of upwind schemes is the requirement of the existence of such Riemann solvers and their expensive computational costs.

The Lax–Friedrichs method, named after Peter Lax and Kurt O. Friedrichs is explicit and first order central scheme. Central schemes serves as an alternative to Godunov’s scheme. As demonstrated in Figure 1.6.2(b), it is Riemann-problem-solver-free at each cell interfaces. Since it’s simple and costs less computation, the solution is usually less accurate than those of Godunov method. It has also developed recently including staggered and non-staggered variants and higher order. Readers can check [Arm97; Bia99; Chr08; Jia98; Kur00a; Kur00b; Kur01a; Kur00c; Kur00d; Lev99] for more details.

Central-upwind schemes are recently developed to enjoy the benefits of avoiding Riemann solvers from central schemes and high accuracy and less dissipation from upwind schemes. They are introduced in [Kur07a; Kur00d; Kur01b]. The main idea behind central-upwind schemes is to use upwinding information at interfaces to better describe numerical flux at interfaces with discontinuities. As shown in Figure 1.6.2(c), we need to study how Riemann problem evolves in 3 regions(rectangles). As a review of construction step, we know that inside a cell like $[x_{j-\frac{1}{2}}, x_{j+\frac{1}{2}}]$, if $q(x, t^n)$ can be chosen to be a piecewise linear or constant function, it’s likely that discontinuities will occur at interface $x_{j\pm\frac{1}{2}}$, which will be local Riemann problems. Thus, from Figure 1.6.2(c), in the most left rectangle and most right rectangle that contains the interfaces $x_{j\pm\frac{1}{2}}$, Riemann problems occur and characteristics intersect. The solution in these 2 rectangles are called (informal) nonsmooth, when the solution inside the middle rectangle is called (informal) smooth since no characteristics from other cells can reach this part.

One-Dimensional Central Upwind Scheme for the Scalar Conservation Law

Here we derive a one-dimensional central upwind scheme for scalar conservation laws, which was originally developed in [Kur00c; Kur00d; Kur01b]. Noted that here we use pain symbol like q , F as scalar functions.

Given

$$\frac{\partial}{\partial t} q(x, t) + \frac{\partial}{\partial x} F(q(x, t)) = 0, \quad (1.6.19)$$

consider the cell $C_j := [x_{j-\frac{1}{2}}, x_{j+\frac{1}{2}}]$ at $t = t^n$. From (1.6.5), we have

$$\bar{q}_j^{n+1} - \bar{q}_j^n = -\frac{1}{\Delta x} \left[\int_{t^n}^{t^{n+1}} F(q(x_{j+\frac{1}{2}}, t)) dt - \int_{t^n}^{t^{n+1}} F(q(x_{j-\frac{1}{2}}, t)) dt \right]. \quad (1.6.20)$$

As mentioned before, cell averages \bar{q}_j can be used to construct piecewise linear function $\tilde{q}(x, t^n)$ inside C_j :

$$\tilde{q}(x, t^n) = P_j^n(x) := \bar{q}_j + (q_x)_j^n (x - x_j), \quad x_{j-\frac{1}{2}} < x < x_{j+\frac{1}{2}}. \quad (1.6.21)$$

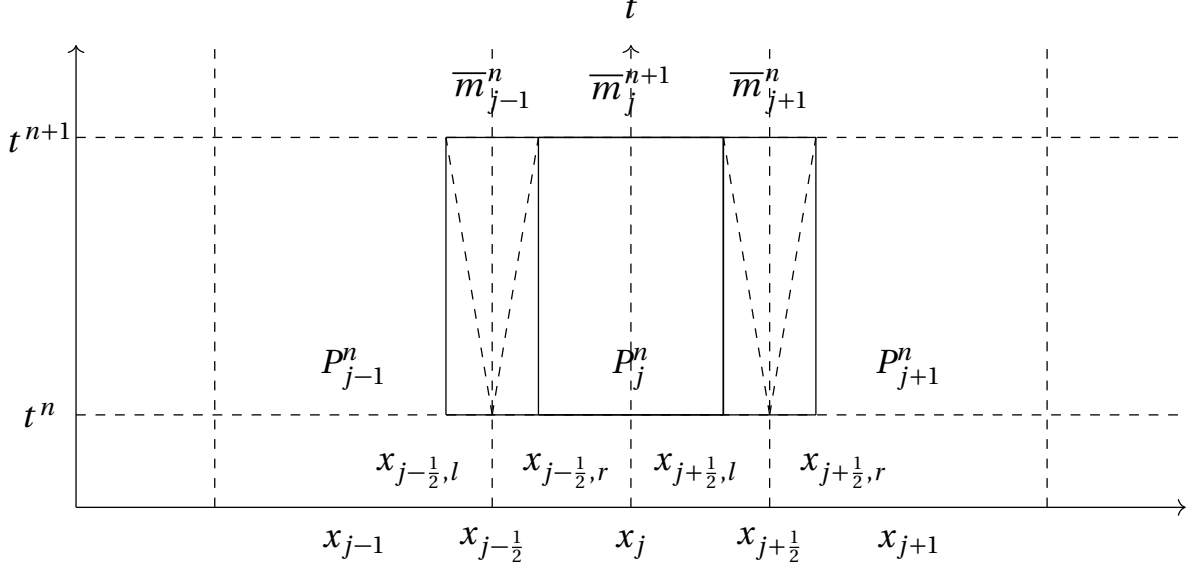


Figure 1.6.3 Control volumes selected according to smooth and nonsmooth areas

A more general form is

$$\tilde{q}(x, t^n) = \sum_j [\bar{q}_j + (q_x)_j^n (x - x_j)] \cdot \chi_{[x_{j-\frac{1}{2}}, x_{j+\frac{1}{2}}]} = \sum_j P_j^n(x) \cdot \chi_{[x_{j-\frac{1}{2}}, x_{j+\frac{1}{2}}]}, \quad (1.6.22)$$

where $\chi_{[x_{j-\frac{1}{2}}, x_{j+\frac{1}{2}}]}$ is a characteristic function in $[x_{j-\frac{1}{2}}, x_{j+\frac{1}{2}}]$. Here, the spatial derivative $(q_x)_j^n$ can be approximated by an appropriate slope limiter, for example, generalized minmod limiter (check [Lie03; Jia98; Swe84] for details):

$$(q_x)_j^n := s_j^n = \text{minmod} \left(\theta \frac{\bar{q}_j^n - \bar{q}_{j-1}^n}{\Delta x}, \frac{\bar{q}_{j+1}^n - \bar{q}_{j-1}^n}{2\Delta x}, \theta \frac{\bar{q}_{j+1}^n - \bar{q}_j^n}{\Delta x} \right), \quad \theta \in [1, 2], \quad (1.6.23)$$

where the minmod function defined as

$$\text{minmod}(z_1, z_2, \dots) := \begin{cases} \min_j \{z_j\}, & \text{if } z_j > 0 \ \forall j, \\ \max_j \{z_j\}, & \text{if } z_j < 0 \ \forall j, \\ 0, & \text{otherwise,} \end{cases} \quad (1.6.24)$$

and θ can control the amount of numerical dissipation and oscillation: larger value of θ corresponds to less dissipation but more oscillation in numerical results.

The discontinuity at $x_{j+\frac{1}{2}}$ (for example) propagate with maximum speed that can be bounded

by the eigenvalues of the Jacobian of the flux with the maximal magnitude:

$$a_{j+\frac{1}{2}}^+ := \max_{q \in C(q_{j+\frac{1}{2}}^-, q_{j+\frac{1}{2}}^+)} \left\{ \lambda_N \left(\frac{\partial F}{\partial q} \right), 0 \right\}, \quad (1.6.25)$$

$$a_{j+\frac{1}{2}}^- := \min_{q \in C(q_{j+\frac{1}{2}}^-, q_{j+\frac{1}{2}}^+)} \left\{ \lambda_1 \left(\frac{\partial F}{\partial q} \right), 0 \right\}, \quad (1.6.26)$$

where $\lambda_1 < \lambda_2 < \dots < \lambda_N$ are N eigenvalues of the Jacobian $\frac{\partial F}{\partial q}$, when it is a system of conservation law of dimension N .

$q_{j+\frac{1}{2}}^\pm$ mentioned above are values at different side of same interface $x_{j+\frac{1}{2}}$, and evaluated from different piecewise construction:

$$q_{j+\frac{1}{2}}^+ = P_{j+1}^n(x_{j+\frac{1}{2}} + 0) \text{ and } q_{j+\frac{1}{2}}^- = P_j^n(x_{j+\frac{1}{2}} - 0), \quad (1.6.27)$$

and $C(q_{j+\frac{1}{2}}^-, q_{j+\frac{1}{2}}^+)$ is the Riemann admissible curve in phase space that connects $q_{j+\frac{1}{2}}^\pm$ and are usually treated as all possible values between $q_{j+\frac{1}{2}}^-, q_{j+\frac{1}{2}}^+$. We refer the reader to [Kur07d; Wan99] for more details.

As Figure 1.6.3 illustrated, $[x_{j-\frac{1}{2},l}, x_{j-\frac{1}{2},r}] \times [t^n, t^{n+1}]$ and $[x_{j+\frac{1}{2},l}, x_{j+\frac{1}{2},r}] \times [t^n, t^{n+1}]$ are nonsmooth area that has characteristics from adjacent cells and $[x_{j-\frac{1}{2},r}, x_{j+\frac{1}{2},l}] \times [t^n, t^{n+1}]$ are smooth area that has characteristics only from the cell C_j :

$$x_{j+\frac{1}{2},l} := x_{j+\frac{1}{2}} + a_{j+\frac{1}{2}}^- \Delta t, \quad x_{j+\frac{1}{2},r} := x_{j+\frac{1}{2}} + a_{j+\frac{1}{2}}^+ \Delta t. \quad (1.6.28)$$

In order to fix $x_{j+\frac{1}{2},l}$ inside $[x_j, x_{j+\frac{1}{2}}]$ and $x_{j+\frac{1}{2},r}$ inside $[x_{j+\frac{1}{2}}, x_{j+1}]$, we can build up a CFL condition:

$$\Delta t \cdot \max_j \left\{ \max(a_{j+\frac{1}{2}}^+, -a_{j+\frac{1}{2}}^-) \right\} < \frac{\Delta x}{2}. \quad (1.6.29)$$

Here, we define cell averages over smooth region in time t_n :

$$\overline{m}_j^n = \frac{1}{x_{j+\frac{1}{2},l} - x_{j-\frac{1}{2},r}} \int_{x_{j-\frac{1}{2},r}}^{x_{j+\frac{1}{2},l}} P_j^n(x) dx. \quad (1.6.30)$$

In a similar way as the computation of (1.6.20), we can use midpoint quadrature for temporal integrals:

$$\begin{aligned} \overline{m}_j^{n+1} - \overline{m}_j^n &= -\frac{1}{x_{j+\frac{1}{2},l} - x_{j-\frac{1}{2},r}} \left[\int_{t^n}^{t^{n+1}} F(q(x_{j+\frac{1}{2},l}, t)) dt - \int_{t^n}^{t^{n+1}} F(q(x_{j-\frac{1}{2},r}, t)) dt \right], \\ \overline{m}_j^{n+1} &= \frac{1}{x_{j+\frac{1}{2},l} - x_{j-\frac{1}{2},r}} \left\{ \int_{x_{j-\frac{1}{2},r}}^{x_{j+\frac{1}{2},l}} P_j^n(x) dx - [F(q(x_{j+\frac{1}{2},l}, t^{n+\frac{1}{2}})) - F(q(x_{j-\frac{1}{2},r}, t^{n+\frac{1}{2}}))] \right\}, \end{aligned}$$

$$\overline{m}_j^{n+1} = \overline{q}_j^n + \frac{s_j^n}{2}(a_{j+\frac{1}{2}}^+ + a_{j+\frac{1}{2}}^-)\Delta t - \frac{\Delta t}{\Delta x - (a_{j+\frac{1}{2}}^+ + a_{j+\frac{1}{2}}^-)\Delta t} \left[F(q(x_{j+\frac{1}{2},l}, t^{n+\frac{1}{2}})) - F(q(x_{j-\frac{1}{2},r}, t^{n+\frac{1}{2}})) \right]. \quad (1.6.31)$$

For cell averages over nonsmooth region in time t_{n+1} :

$$\overline{m}_{j+\frac{1}{2}}^n = \frac{1}{x_{j+\frac{1}{2},r} - x_{j+\frac{1}{2},l}} \left[\int_{x_{j+\frac{1}{2},l}}^{x_{j+\frac{1}{2}}} P_j^n(x) dx + \int_{x_{j+\frac{1}{2}}}^{x_{j+\frac{1}{2},r}} P_{j+1}^n(x) dx \right]. \quad (1.6.32)$$

In a similar way as the computation of (1.6.20), we can use midpoint quadrature for temporal integrals:

$$\begin{aligned} \overline{m}_{j+\frac{1}{2}}^{n+1} - \overline{m}_{j+\frac{1}{2}}^n &= -\frac{1}{x_{j+\frac{1}{2},r} - x_{j+\frac{1}{2},l}} \left[\int_{t^n}^{t^{n+1}} F(q(x_{j+\frac{1}{2},r}, t)) dt - \int_{t^n}^{t^{n+1}} F(q(x_{j+\frac{1}{2},l}, t)) dt \right], \\ \overline{m}_j^{n+1} &= \frac{1}{x_{j+\frac{1}{2},r} - x_{j+\frac{1}{2},l}} \left\{ \int_{x_{j+\frac{1}{2},l}}^{x_{j+\frac{1}{2}}} P_j^n(x) dx + \int_{x_{j+\frac{1}{2}}}^{x_{j+\frac{1}{2},r}} P_{j+1}^n(x) dx \right. \\ &\quad \left. - \left[F(q(x_{j+\frac{1}{2},l}, t^{n+\frac{1}{2}})) - F(q(x_{j-\frac{1}{2},r}, t^{n+\frac{1}{2}})) \right] \right\}, \\ \overline{m}_j^{n+1} &= \frac{1}{a_{j+\frac{1}{2}}^+ - a_{j+\frac{1}{2}}^-} \left\{ q_{j+\frac{1}{2},r}^n a_{j+\frac{1}{2}}^+ - \frac{s_{j+1}^n}{2} (a_{j+\frac{1}{2}}^+)^2 \Delta t - q_{j+\frac{1}{2},l}^n a_{j+\frac{1}{2}}^- + \frac{s_j^n}{2} (a_{j+\frac{1}{2}}^-)^2 \Delta t \right. \\ &\quad \left. - \left[F(q(x_{j+\frac{1}{2},r}, t^{n+\frac{1}{2}})) - F(q(x_{j+\frac{1}{2},l}, t^{n+\frac{1}{2}})) \right] \right\}. \quad (1.6.33) \end{aligned}$$

At projection step, we can use a piecewise linear function to describe nonsmooth and smooth solution at time $t = t^{n+1}$:

$$\tilde{m}(x, t^{n+1}) = \begin{cases} \overline{m}_j^{n+1} + s_{j+\frac{1}{2}}^{n+1} (x - \frac{x_{j+\frac{1}{2},l} + x_{j-\frac{1}{2},r}}{2}), & x \in [x_{j-\frac{1}{2},r}, x_{j+\frac{1}{2},l}], \\ \overline{m}_{j+\frac{1}{2}}^{n+1}, & x \in [x_{j+\frac{1}{2},l}, x_{j+\frac{1}{2},r}]. \end{cases} \quad (1.6.34)$$

Here slope $s_{j+\frac{1}{2}}^{n+1}$ can be estimated using the minmod limiter:

$$s_{j+\frac{1}{2}}^{n+1} = \frac{\text{minmod}(\overline{m}_{j+\frac{1}{2}}^{n+1} - q_{j+\frac{1}{2},l}^{n+1}, q_{j+\frac{1}{2},r}^{n+1} - \overline{m}_{j+\frac{1}{2}}^{n+1})}{\frac{\Delta t}{2}(a_{j+\frac{1}{2}}^+ - a_{j+\frac{1}{2}}^-)}, \quad (1.6.35)$$

More approaches about numerical slope $s_{j+\frac{1}{2}}^{n+1}$ can be found in [Kur01b; Kur00c].

Thus we can derive cell averages of $[x_{j-\frac{1}{2}}, x_{j+\frac{1}{2}}]$ as:

$$\overline{q}_j^{n+1} = \lambda a_{j-\frac{1}{2}}^+ \overline{m}_{j-\frac{1}{2}}^{n+1} + [1 + \lambda(a_{j+\frac{1}{2}}^- - a_{j-\frac{1}{2}}^+)] \overline{m}_{j-\frac{1}{2}}^{n+1} - \lambda a_{j+\frac{1}{2}}^- \overline{m}_{j+\frac{1}{2}}^{n+1}$$

$$+ \frac{\lambda \Delta t}{2} \left[s_{j+\frac{1}{2}}^{n+1} a_{j+\frac{1}{2}}^+ a_{j+\frac{1}{2}}^- + s_{j-\frac{1}{2}}^{n+1} a_{j-\frac{1}{2}}^+ a_{j-\frac{1}{2}}^- \right], \quad (1.6.36)$$

After we put (1.6.36), nonsmooth average in (1.6.33) and smooth average in (1.6.31) to differential equation:

$$\frac{d}{dt} q_j^n = \lim_{\Delta t \rightarrow 0} \frac{\bar{q}_j^{n+1} - \bar{q}_j^n}{\Delta t}, \quad (1.6.37)$$

We can finally get the *1-D semi-discrete central-upwind scheme*:

$$\frac{d}{dt} \bar{q}_j(t) = - \frac{H_{j+\frac{1}{2}}(t) - H_{j-\frac{1}{2}}(t)}{\Delta x}, \quad (1.6.38)$$

computed in terms of the Central-Upwind numerical flux,

$$H_{j+\frac{1}{2}}(t) := \frac{a_{j+\frac{1}{2}}^+ F(q_{j+\frac{1}{2}}^-) - a_{j+\frac{1}{2}}^- F(q_{j+\frac{1}{2}}^+)}{a_{j+\frac{1}{2}}^+ - a_{j+\frac{1}{2}}^-} + \alpha_{j+\frac{1}{2}} (q_{j+\frac{1}{2}}^+ - q_{j+\frac{1}{2}}^- - \delta q_{j+\frac{1}{2}}), \quad (1.6.39)$$

with the coefficient

$$\alpha_{j+\frac{1}{2}} = \frac{a_{j+\frac{1}{2}}^+ a_{j+\frac{1}{2}}^-}{a_{j+\frac{1}{2}}^+ - a_{j+\frac{1}{2}}^-}, \quad (1.6.40)$$

and anti-diffusion term

$$\delta q_{j-\frac{1}{2}} = \frac{a_{j+\frac{1}{2}}^+ - a_{j+\frac{1}{2}}^-}{2} \lim_{\Delta t \rightarrow 0} \left\{ \Delta t s_{j+\frac{1}{2}}^{n+1} \right\} = \min \text{mod}(q_{j+\frac{1}{2}}^+ - q_{j+\frac{1}{2}}^*, q_{j+\frac{1}{2}}^* - q_{j+\frac{1}{2}}^-), \quad (1.6.41)$$

with an intermediate state

$$q_{j+\frac{1}{2}}^* = \lim_{\Delta t \rightarrow 0} \bar{m}_{j+\frac{1}{2}}^{n+1} = \frac{a_{j+\frac{1}{2}}^+ q_{j+\frac{1}{2}}^+ - a_{j+\frac{1}{2}}^- q_{j+\frac{1}{2}}^- - [F(q_{j+\frac{1}{2}}^+) - F(q_{j+\frac{1}{2}}^-)]}{a_{j+\frac{1}{2}}^+ - a_{j+\frac{1}{2}}^-}. \quad (1.6.42)$$

Two-Dimensional Central Upwind Scheme for a System of Balance Laws

Noted that here we use bold symbol like \mathbf{q} , \mathbf{F} , \mathbf{G} , and \mathbf{S} as vector functions.

For completeness, we describe 2-dimensional second-order semi-discrete central-upwind scheme for the system of hyperbolic balance laws given by

$$\frac{\partial}{\partial t} \mathbf{q}(x, y, t) + \frac{\partial}{\partial x} \mathbf{F}(\mathbf{q}(x, y, t)) + \frac{\partial}{\partial y} \mathbf{G}(\mathbf{q}(x, y, t)) = \mathbf{S}(\mathbf{q}(x, y, t)), \quad (1.6.43)$$

where \mathbf{q} represents The computation domain is broken into a rectangular grid, $C_{j,k} := [x_{j-\frac{1}{2}}, x_{j+\frac{1}{2}}] \times [y_{k-\frac{1}{2}}, y_{k+\frac{1}{2}}]$ with $|C_{j,k}| = \Delta x \Delta y$ centered at (x_j, y_k) for $j = 1, \dots, M$ and $k = 1, \dots, N$ being the indices of the grid in the x -direction and y -direction, respectively. The cell averages of $C_{j,k}$ of the computed

numerical solution

$$\bar{q}_{j,k}(t) := \frac{1}{\Delta x \Delta y} \iint_{C_{j,k}} q(x, y, t) dx dy, \quad (1.6.44)$$

$$\bar{S}_{j,k}(t) := \frac{1}{\Delta x \Delta y} \iint_{C_{j,k}} S(x, y, t) dx dy, \quad (1.6.45)$$

are available at time level t . The second order 2-D semi-discrete the central upwind scheme to (1.6.43) is the following system of ODEs:

$$\frac{d}{dt} \bar{q}_j(t) = -\frac{H_{j+\frac{1}{2},k}^x(t) - H_{j-\frac{1}{2},k}^x(t)}{\Delta x} - \frac{H_{j,k+\frac{1}{2}}^y(t) - H_{j,k-\frac{1}{2}}^y(t)}{\Delta y} + \bar{S}_{j,k}(t), \quad (1.6.46)$$

where $H_{j\pm\frac{1}{2},k}^x(t)$ and $H_{j,k\pm\frac{1}{2}}^y(t)$ are the central-upwind numerical fluxes given by

$$\begin{aligned} H_{j+\frac{1}{2},k}^x(t) &:= \frac{a_{j+\frac{1}{2},k}^+ F(q_{j+\frac{1}{2},k}^-) - a_{j+\frac{1}{2},k}^- F(q_{j+\frac{1}{2},k}^+)}{a_{j+\frac{1}{2},k}^+ - a_{j+\frac{1}{2},k}^-} + \alpha_{j+\frac{1}{2},k} (q_{j+\frac{1}{2},k}^+ - q_{j+\frac{1}{2},k}^- - \delta q_{j+\frac{1}{2},k}), \\ H_{j,k+\frac{1}{2}}^y(t) &:= \frac{b_{j,k+\frac{1}{2}}^+ G(q_{j,k+\frac{1}{2}}^-) - b_{j,k+\frac{1}{2}}^- G(q_{j,k+\frac{1}{2}}^+)}{b_{j,k+\frac{1}{2}}^+ - b_{j,k+\frac{1}{2}}^-} + \beta_{j,k+\frac{1}{2}} (q_{j,k+\frac{1}{2}}^+ - q_{j,k+\frac{1}{2}}^- - \delta q_{j,k+\frac{1}{2}}), \end{aligned} \quad (1.6.47)$$

with the coefficients

$$\begin{aligned} \alpha_{j+\frac{1}{2},k} &= \frac{a_{j+\frac{1}{2},k}^+ a_{j+\frac{1}{2},k}^-}{a_{j+\frac{1}{2},k}^+ - a_{j+\frac{1}{2},k}^-}, \\ \beta_{j,k+\frac{1}{2}} &= \frac{b_{j,k+\frac{1}{2}}^+ b_{j,k+\frac{1}{2}}^-}{b_{j,k+\frac{1}{2}}^+ - b_{j,k+\frac{1}{2}}^-}, \end{aligned} \quad (1.6.48)$$

and anti-diffusion term

$$\begin{aligned} \delta q_{j+\frac{1}{2},k} &= \minmod(q_{j+\frac{1}{2},k}^+ - q_{j+\frac{1}{2},k}^*, q_{j+\frac{1}{2},k}^* - q_{j+\frac{1}{2},k}^-), \\ \delta q_{j,k+\frac{1}{2}} &= \minmod(q_{j,k+\frac{1}{2}}^+ - q_{j,k+\frac{1}{2}}^*, q_{j,k+\frac{1}{2}}^* - q_{j,k+\frac{1}{2}}^-), \end{aligned} \quad (1.6.49)$$

$$(1.6.50)$$

with intermediate states

$$\begin{aligned} q_{j+\frac{1}{2},k}^* &= \frac{a_{j+\frac{1}{2},k}^+ q_{j+\frac{1}{2},k}^+ - a_{j+\frac{1}{2},k}^- q_{j+\frac{1}{2},k}^- - [F(q_{j+\frac{1}{2},k}^+) - F(q_{j+\frac{1}{2},k}^-)]}{a_{j+\frac{1}{2},k}^+ - a_{j+\frac{1}{2},k}^-}, \\ q_{j,k+\frac{1}{2}}^* &= \frac{b_{j,k+\frac{1}{2}}^+ q_{j,k+\frac{1}{2}}^+ - b_{j,k+\frac{1}{2}}^- q_{j,k+\frac{1}{2}}^- - [F(q_{j,k+\frac{1}{2}}^+) - F(q_{j,k+\frac{1}{2}}^-)]}{b_{j,k+\frac{1}{2}}^+ - b_{j,k+\frac{1}{2}}^-}. \end{aligned} \quad (1.6.51)$$

Here, in (1.6.47), $q_{j+\frac{1}{2},k}^{\pm}$ and $q_{j,k+\frac{1}{2}}^{\pm}$ are interpolated point values at different sides of cell interfaces $(x_{j+\frac{1}{2}}, y_k)$ and $(x_j, y_{k+\frac{1}{2}})$ from piecewise linear reconstructions:

$$\tilde{q}(x, y) = \sum_i [\bar{q}_{j,k} + (q_x)_{j,k}(x - x_j) + (q_y)_{j,k}(y - y_k)] \cdot \chi_{[x_{j-\frac{1}{2}}, x_{j+\frac{1}{2}}] \times [y_{k-\frac{1}{2}}, y_{k+\frac{1}{2}}]}. \quad (1.6.52)$$

The formulas are given below:

$$\begin{aligned} q_{j+\frac{1}{2},k}^+ &= \bar{q}_{j+1,k} - \frac{\Delta x}{2}(q_x)_{j+1,k}, \quad q_{j+\frac{1}{2},k}^- = \bar{q}_{j,k} + \frac{\Delta x}{2}(q_x)_{j,k}, \\ q_{j,k+\frac{1}{2}}^+ &= \bar{q}_{j,k+1} - \frac{\Delta y}{2}(q_y)_{j,k+1}, \quad q_{j,k+\frac{1}{2}}^- = \bar{q}_{j,k} + \frac{\Delta y}{2}(q_y)_{j,k}. \end{aligned} \quad (1.6.53)$$

Generalized minmod limiter is used here for slopes:

$$\begin{aligned} (q_x)_{j,k} &= \text{minmod} \left(\theta \frac{\bar{q}_{j,k} - \bar{q}_{j-1,k}}{\Delta x}, \frac{\bar{q}_{j+1,k} - \bar{q}_{j-1,k}}{2\Delta x}, \theta \frac{\bar{q}_{j+1,k} - \bar{q}_{j,k}}{\Delta x} \right), \\ (q_y)_{j,k} &= \text{minmod} \left(\theta \frac{\bar{q}_{j,k} - \bar{q}_{j,k-1}}{\Delta y}, \frac{\bar{q}_{j,k+1} - \bar{q}_{j,k-1}}{2\Delta y}, \theta \frac{\bar{q}_{j,k+1} - \bar{q}_{j,k}}{\Delta y} \right), \end{aligned} \quad (1.6.54)$$

where the minmod function defined as

$$\text{minmod}(z_1, z_2, \dots) := \begin{cases} \min_j \{z_j\}, & \text{if } z_j > 0 \forall j, \\ \max_j \{z_j\}, & \text{if } z_j < 0 \forall j, \\ 0, & \text{otherwise,} \end{cases} \quad (1.6.55)$$

and $\theta \in [1, 2]$ can control the amount of numerical dissipation and oscillation: larger value of θ corresponds to less dissipation but more oscillation in numerical results.

The local propagation speeds $a_{j+\frac{1}{2},k}^{\pm}$ and $b_{j,k+\frac{1}{2}}^{\pm}$ are computed same way using the eigenvalues λ_i of $\frac{\partial \mathbf{F}}{\partial \mathbf{q}}$ and $\frac{\partial \mathbf{G}}{\partial \mathbf{q}}$, where $\lambda_1 < \lambda_2 < \dots < \lambda_N$:

$$\begin{aligned} a_{j+\frac{1}{2},k}^+ &:= \max \left\{ \lambda_N \left(\frac{\partial \mathbf{F}}{\partial \mathbf{q}}(q_{j+\frac{1}{2},k}^-) \right), \lambda_N \left(\frac{\partial \mathbf{F}}{\partial \mathbf{q}}(q_{j+\frac{1}{2},k}^+) \right), 0 \right\}, \\ a_{j+\frac{1}{2},k}^- &:= \max \left\{ \lambda_1 \left(\frac{\partial \mathbf{F}}{\partial \mathbf{q}}(q_{j+\frac{1}{2},k}^-) \right), \lambda_1 \left(\frac{\partial \mathbf{F}}{\partial \mathbf{q}}(q_{j+\frac{1}{2},k}^+) \right), 0 \right\}, \\ b_{j,k+\frac{1}{2}}^+ &:= \max \left\{ \lambda_N \left(\frac{\partial \mathbf{G}}{\partial \mathbf{q}}(q_{j,k+\frac{1}{2}}^-) \right), \lambda_N \left(\frac{\partial \mathbf{G}}{\partial \mathbf{q}}(q_{j,k+\frac{1}{2}}^+) \right), 0 \right\}, \\ b_{j,k+\frac{1}{2}}^- &:= \max \left\{ \lambda_1 \left(\frac{\partial \mathbf{G}}{\partial \mathbf{q}}(q_{j,k+\frac{1}{2}}^-) \right), \lambda_1 \left(\frac{\partial \mathbf{G}}{\partial \mathbf{q}}(q_{j,k+\frac{1}{2}}^+) \right), 0 \right\}. \end{aligned} \quad (1.6.56)$$

The time step can be chosen to satisfy the CFL condition below:

$$\Delta t \cdot \max \left\{ \frac{\max_j \left(|a_{j+\frac{1}{2},k}^\pm| \right)}{\Delta x}, \frac{\max_k \left(|b_{j,k+\frac{1}{2}}^\pm| \right)}{\Delta y} \right\} < \frac{1}{4}. \quad (1.6.57)$$

CHAPTER

2

NON-HYDROSTATIC SAINT-VENANT SYSTEM

The main part of this chapter have been accepted in Proceedings of the XVII International Conference on Hyperbolic Problems: Theory, Numerics and Applications,[Che20]

In this chapter, we will discuss non-hydrostatic Saint-Venant System. It's proposed in [M.-O. BRISTEAU AND J. SAINTE-MARIE, *Discrete Contin. Dyn. Syst. Ser. B*, 10 (2008), pp. 733–759]. The physical background of this equation is tsunami waves. We are interested in its long-time performance in deep water and on-shore behaviors of tsunami-like waves. Classical Saint-Venant system[SV71], however, works well in model lakes, rivers and coastal areas in a relative short time spacial scale. Over long time, solutions of the Saint-Venant system break down, dissipate in an unphysical manner, shock waves develop, and the system fails to capture small, trailing waves that are seen in nature and laboratory experiments [MI06].

Non-hydrostatic models(the celebrated Green-Naghdi equation [Gre76; Bar04; Bon02; Bon04]) work well for long-time propagation of tsunami-like waves because they allow the wave to travel for long distances without decaying in amplitude. In addition, since these systems are dispersive, they give rise to trailing waves that are observed to follow tsunamis in nature. However, it is necessary to achieve some balance between dispersion observed with a non-hydrostatic model and the dissipation seen in the classical Saint-Venant system.

2.1 Mathematical Model

The non-hydrostatic Saint-Venant system presented in [Bri11; Bri08] is given by

$$\begin{cases} h_t + (hu)_x = 0, \\ (hu)_t + M_t + \left(hu^2 + \frac{g}{2}h^2\right)_x + N = -ghB_x + p^a w_x - 4(\nu u_x)_x - \kappa(h, hu)u, \end{cases} \quad (2.1.1)$$

where $h(x, t)$ is the water depth measured vertically from the bottom topography, described by function $B(x, t)$, $u(x, t)$ is the vertically averaged velocity, hu is the horizontal momentum or discharge, $p^a = p^a(x, t)$ is the atmospheric pressure function, $w := h + B$ is the free surface, ν is the viscosity coefficient, κ is the friction function, and M and N are defined as

$$M(h, hu, B) = \left(-\frac{1}{3}h^3u_x + \frac{1}{2}h^2B_xu\right)_x + B_x\left(-\frac{1}{2}h^2u_x + B_xhu\right),$$

and

$$N(h, hu, B) = \left((h^2)_t(hu_x - B_xu)\right)_x + 2B_xh_t(hu_x - B_xu) - B_{xt}\left(-\frac{1}{2}h^2u_x + B_xhu\right). \quad (2.1.2)$$

Here, M and N are terms that arise when the system is derived from the Euler equations and include non-hydrostatic pressure terms [Bri08].

One of the goals of the current work is to numerically study the effects of the dispersion terms present in the non-hydrostatic model (2.1.1). To this end, we introduce the *new scaling parameters* α_M and α_N as coefficients to M and N in (2.1.1). For the purpose of this work we will neglect fluid viscosity and friction by setting ν and $\kappa(h, hu)$ to be identically zero and also assume that the bottom topography function is independent of time, i.e., $B = B(x)$. In addition, we follow the approach in [Kur02; Kur07c] and rewrite our system in terms of the equilibrium variables $w = h + B$ and $q := hu$:

$$\begin{cases} w_t + q_x = 0, \\ q_t + \alpha_M M_t + \left(\frac{q^2}{w - B} + \frac{g}{2}(w - B)^2\right)_x + \alpha_N N = -g(w - B)B_x + p^a w_x. \end{cases} \quad (2.1.3)$$

When $\alpha_M = \alpha_N = p^a \equiv 0$, (2.1.3) reduces to the classical Saint-Venant system, and as we increase these parameters, the amount of dispersion in our model increases and the effects of the lack of the hydrostatic pressure assumption should be apparent.

2.1.1 Central-Upwind Scheme

We develop a new well-balanced positivity preserving scheme for (2.1.3), which is based on the semi-discrete central-upwind scheme from [Kur01b] (see also [Kur07c; Kur09]). For simplicity, we introduce a uniform grid $x_j = j\Delta x$ where Δx is a small spatial scale, and denote the computational cells centered at x_j by $I_j := [x_{j-\frac{1}{2}}, x_{j+\frac{1}{2}}]$.

Here, in order not to cause confusion, we use U instead of q to represent the unknowns. Then we rewrite the system (2.1.3) in the following form:

$$U_t + M(U, B)_t + F(U, B)_x + N(U, B) = S(U, B), \quad U := (w, q)^T, \quad (2.1.4)$$

where

$$\begin{aligned} F(U, B) &= \left(q, \frac{q^2}{w-B} + \frac{g}{2}(w-B)^2 \right)^T, \quad S(U, B) = (0, -g(w-B)B_x + p^a w_x)^T, \\ M(U, B) &= (0, \alpha_M M(U, B))^T, \quad N(U, B) = (0, \alpha_N N(U, B))^T. \end{aligned}$$

Using the above notations, a semi-discrete central-upwind scheme for (2.1.4) takes the form of the following system of time-dependent ODEs:

$$\frac{d}{dt}(\overline{U}_j(t) + \overline{M}_j(t)) = -\frac{H_{j+\frac{1}{2}}(t) - H_{j-\frac{1}{2}}(t)}{\Delta x} + \overline{S}_j(t) - \overline{N}_j(t), \quad (2.1.5)$$

where $(\overline{\cdot})_j(t)$ is used to denote the approximated cell averages over the corresponding cells:

$$\begin{aligned} \overline{U}_j(t) &\approx \frac{1}{\Delta x} \int_{I_j} U(x, t) dx, \quad \overline{S}_j(t) \approx \frac{1}{\Delta x} \int_{I_j} S(U(x, t), B(x)) dx, \\ \overline{M}_j(t) &\approx \frac{1}{\Delta x} \int_{I_j} M(U(x, t), B(x)) dx, \quad \overline{N}_j(t) \approx \frac{1}{\Delta x} \int_{I_j} N(U(x, t), B(x)) dx, \end{aligned}$$

and $H_{j+\frac{1}{2}}(t)$ are the central-upwind numerical fluxes $H_{j+\frac{1}{2}}$ proposed in [Kur07c] (see also [Kur07b; Kur01b]):

$$H_{j+\frac{1}{2}}(t) = \frac{a_{j+\frac{1}{2}}^+ F(U_{j+\frac{1}{2}}^-, B_{j+\frac{1}{2}}) - a_{j+\frac{1}{2}}^- F(U_{j+\frac{1}{2}}^+, B_{j+\frac{1}{2}})}{a_{j+\frac{1}{2}}^+ - a_{j+\frac{1}{2}}^-} + \frac{a_{j+\frac{1}{2}}^+ a_{j+\frac{1}{2}}^-}{a_{j+\frac{1}{2}}^+ - a_{j+\frac{1}{2}}^-} [U_{j+\frac{1}{2}}^+ - U_{j+\frac{1}{2}}^-]. \quad (2.1.6)$$

Here, the values $U_{j+\frac{1}{2}}^\pm$ are the right/left point values at $x = x_{j+\frac{1}{2}}$ of the conservative piecewise linear reconstruction \tilde{U} ,

$$\tilde{U}(x) := \overline{U}_j + (U_x)_j (x - x_j), \quad x_{j-\frac{1}{2}} < x < x_{j+\frac{1}{2}}, \quad (2.1.7)$$

which is used to approximate U at time t , that is,

$$U_{j+\frac{1}{2}}^\pm := \tilde{U}(x_{j+\frac{1}{2}} \pm 0) = \overline{U}_{j+\frac{1}{2} \pm \frac{1}{2}} \mp \frac{\Delta x}{2} (U_x)_{j+\frac{1}{2} \pm \frac{1}{2}}. \quad (2.1.8)$$

The numerical derivatives $(U_x)_j$ are at least first-order accurate component-wise approximations of $U_x(x_j, t)$, computed using a nonlinear limiter needed to ensure the non-oscillatory nature of the reconstruction (2.1.7). The right- and left-sided local speeds $a_{j+\frac{1}{2}}^\pm$ in (2.1.6) are obtained from the smallest and largest eigenvalues of the Jacobian $\frac{\partial U}{\partial U}$ (see Section 2.1.1.1 for details). Notice that

the terms $U_{j+\frac{1}{2}}^\pm, \bar{U}_j, a_{j+\frac{1}{2}}^\pm, \tilde{U}(x)$ and $(U_x)_j$ all depend on t , but we suppress this dependence for simplicity.

We also follow the work of [Kur07c; Kur09] and replace $B(x)$ in (2.1.6) with its continuous piecewise linear approximation by defining

$$B_{j+\frac{1}{2}} := B(x_{j+\frac{1}{2}}) \quad \text{and} \quad B_j := \frac{1}{2}(B_{j+\frac{1}{2}} + B_{j-\frac{1}{2}}). \quad (2.1.9)$$

This will help to ensure the positivity preserving nature of the proposed scheme, as we show below.

2.1.1.1 Positivity-Preserving Reconstruction

The use of a piecewise linear reconstruction (2.1.7) requires the computation of slopes $(U_x)_j$ to obtain the right/left point values defined in (2.1.8). It is well-known that in order to ensure the non-oscillatory nature of the reconstruction, the use of a nonlinear limiter is required. We choose to use the generalized minmod limiter:

$$(U_x)_j = \text{minmod} \left(\theta \frac{\bar{U}_j - \bar{U}_{j-1}}{\Delta x}, \frac{\bar{U}_{j+1} - \bar{U}_{j-1}}{2\Delta x}, \theta \frac{\bar{U}_{j+1} - \bar{U}_j}{\Delta x} \right), \quad \theta \in [1, 2], \quad (2.1.10)$$

where the minmod function defined as

$$\text{minmod}(z_1, z_2, \dots) := \begin{cases} \min_j \{z_j\}, & \text{if } z_j > 0 \forall j, \\ \max_j \{z_j\}, & \text{if } z_j < 0 \forall j, \\ 0, & \text{otherwise,} \end{cases}$$

is applied in a componentwise manner. The parameter θ can be used to control the amount of numerical viscosity present in the resulting scheme (see, e.g., [Lie03; Nes90; Swe84] for more details concerning the generalized minmod and other nonlinear limiters).

Even when all of the cell averages \bar{h}_j are nonnegative, the reconstructed right/left point values at the cell interface $h_{j+\frac{1}{2}}^\pm$ may be negative. To guarantee positivity of h throughout the entire computational domain, we follow the procedure from [Kur07c] and amend the reconstruction (2.1.7), (2.1.8), (2.1.10) in the following conservative way:

$$\begin{aligned} \text{if } w_{j+\frac{1}{2}}^- < B_{j+\frac{1}{2}}, \quad \text{then take } (w_x)_j &:= -\frac{\bar{w}_j}{\Delta x/2} \implies w_{j+\frac{1}{2}}^- = B_{j+\frac{1}{2}}, \quad w_{j-\frac{1}{2}}^+ = 2\bar{w}_j, \\ \text{if } w_{j-\frac{1}{2}}^+ < B_{j-\frac{1}{2}}, \quad \text{then take } (w_x)_j &:= \frac{\bar{w}_j}{\Delta x/2} \implies w_{j+\frac{1}{2}}^- = 2\bar{w}_j, \quad w_{j-\frac{1}{2}}^+ = B_{j-\frac{1}{2}}. \end{aligned} \quad (2.1.11)$$

It is necessary to compute the nonconservative quantity $u = q/h$ for the computation of numerical fluxes and local propagation speeds. We follow the desingularization procedure outlined in

[Kur07c; Kur09] to avoid possible division by small values of h :

$$u := \frac{\sqrt{2}(w-B) \cdot q}{\sqrt{(w-B)^4 + \max((w-B)^4, \varepsilon)}}, \quad (2.1.12)$$

where ε is a small desingularization parameter (in our numerical experiments, we have taken $\varepsilon = \min((\Delta x)^3, 10^{-4})$). Notice that this procedure will only affect the velocity computations when $h^4 < \varepsilon$. It is also important to recalculate the values of q at the points where the velocity was desingularized by setting

$$q := h \cdot u.$$

Since the flux term U in (2.1.4) is equivalent to that of the classical Saint-Venant system, the local propagation speeds $a_{j+\frac{1}{2}}^\pm$ are computed the same way using the eigenvalues of $\frac{\partial U}{\partial U}$:

$$\begin{aligned} a_{j+\frac{1}{2}}^+ &:= \max \left\{ u_{j+\frac{1}{2}}^+ + \sqrt{g h_{j+\frac{1}{2}}^+}, u_{j+\frac{1}{2}}^- + \sqrt{g h_{j+\frac{1}{2}}^-}, 0 \right\}, \\ a_{j+\frac{1}{2}}^- &:= \min \left\{ u_{j+\frac{1}{2}}^+ - \sqrt{g h_{j+\frac{1}{2}}^+}, u_{j+\frac{1}{2}}^- - \sqrt{g h_{j+\frac{1}{2}}^-}, 0 \right\}. \end{aligned}$$

Remark 2.1.1 Proof of the positivity preserving property of this reconstruction is available in [Kur02; Kur07c].

2.1.1.2 Discretization of the Non-hydrostatic Pressure Terms

The dispersive terms \overline{M}_j and \overline{N}_j are computed using the second-order midpoint rule. We first follow [Bri11] and discretize the terms of M at x_j in the following ways:

$$\begin{aligned} \left(\frac{1}{3} h^3 u_x \right)_x (x_j) &\approx \frac{1}{3\Delta x} \left[\frac{u_{j+1} - u_j}{\Delta x} (h_{j+\frac{1}{2}})^3 - \frac{u_j - u_{j-1}}{\Delta x} (h_{j-\frac{1}{2}})^3 \right] \\ &= \frac{1}{3(\Delta x)^2} \left[\frac{(h_{j+\frac{1}{2}})^3}{\overline{h}_{j+1}} \overline{q}_{j+1} - \frac{(h_{j+\frac{1}{2}})^3 + (h_{j-\frac{1}{2}})^3}{\overline{h}_j} \overline{q}_j + \frac{(h_{j-\frac{1}{2}})^3}{\overline{h}_{j-1}} \overline{q}_{j-1} \right], \end{aligned} \quad (2.1.13)$$

$$\begin{aligned} \left(\frac{1}{2} h^2 B_x u \right)_x (x_j) &= \left(\frac{1}{2} h B_x q \right)_x (x_j) \approx \frac{1}{2\Delta x} \left[h_{j+\frac{1}{2}} (B_x)_{j+\frac{1}{2}} q_{j+\frac{1}{2}} - h_{j-\frac{1}{2}} (B_x)_{j-\frac{1}{2}} q_{j-\frac{1}{2}} \right] \\ &= \frac{1}{4\Delta x} \left[h_{j+\frac{1}{2}} (B_x)_{j+\frac{1}{2}} \overline{q}_{j+1} + \left(h_{j+\frac{1}{2}} (B_x)_{j+\frac{1}{2}} - h_{j-\frac{1}{2}} (B_x)_{j-\frac{1}{2}} \right) \overline{q}_j - h_{j-\frac{1}{2}} (B_x)_{j-\frac{1}{2}} \overline{q}_{j-1} \right], \end{aligned} \quad (2.1.14)$$

$$\begin{aligned} \left(\frac{1}{2} B_x h^2 u_x \right)_x (x_j) &\approx \frac{1}{2} (B_x)_j \overline{h}_j^2 (u_x)_j \approx \frac{1}{2} (B_x)_j \overline{h}_j^2 \left[\frac{1}{\overline{h}_j} (q_x)_j - \frac{(h_x)_j}{\overline{h}_j^2} \overline{q}_j \right] \\ &= \frac{1}{4\Delta x} (B_x)_j \left[\overline{h}_j \overline{q}_{j+1} - 2\Delta x (h_x)_j \overline{q}_j - \overline{h}_j \overline{q}_{j-1} \right] \end{aligned} \quad (2.1.15)$$

$$(B_x^2 h u)(x_j) \approx (B_x)_j^2 \bar{q}_j, \quad (2.1.16)$$

where $u_j := \bar{q}_j / \bar{h}_j$ and

$$\begin{aligned} u_{j+\frac{1}{2}} &:= \frac{1}{2}(u_{j+1} + u_j), \quad h_{j+\frac{1}{2}} := \frac{1}{2}(\bar{h}_{j+1} + \bar{h}_j), \quad q_{j+\frac{1}{2}} := \frac{1}{2}(\bar{q}_{j+1} + \bar{q}_j), \\ (B_x)_j &:= \frac{B_{j+\frac{1}{2}} - B_{j-\frac{1}{2}}}{\Delta x}, \quad (B_x)_{j+\frac{1}{2}} := \frac{1}{2}((B_x)_{j+1} + (B_x)_j), \quad (q_x)_j := \frac{\bar{q}_{j+1} - \bar{q}_{j-1}}{2\Delta x}. \end{aligned} \quad (2.1.17)$$

We then replace the time derivatives h_t by its space equivalent $-q_x$ and use (2.1.17) to obtain the following discretization of N :

$$\begin{aligned} N_j = & -\frac{2}{\Delta x} \left[h_{j+\frac{1}{2}} \cdot \frac{q_{j+1} - q_j}{\Delta x} \left(h_{j+\frac{1}{2}} \frac{u_{j+1} - u_j}{\Delta x} - (B_x)_{j+\frac{1}{2}} u_{j+\frac{1}{2}} \right) \right. \\ & \left. - h_{j-\frac{1}{2}} \cdot \frac{q_j - q_{j-1}}{\Delta x} \left(h_{j-\frac{1}{2}} \frac{u_j - u_{j-1}}{\Delta x} - (B_x)_{j-\frac{1}{2}} u_{j-\frac{1}{2}} \right) \right] \\ & - 2(B_x)_j (q_x)_j \{ (q_x)_j - [(h_x)_j + (B_x)_j] u_j \} \end{aligned} \quad (2.1.18)$$

Remark 2.1.2 In equations (2.1.13)–(2.1.16), $(h_x)_j$ are obtained using the limiter as it is described in Section 2.1.1.1, while $(q_x)_j$ are calculated using the centered differences (see (2.1.17)). The latter is done to avoid the need to solve a nonlinear system of algebraic equations as we explain in Section 2.1.2.

Remark 2.1.3 We would like point out that all of the terms in (2.1.13)–(2.1.16) will be taken at either t^n or t^{n+1} depending on a particular choice of the time evolution method for the numerical integration of the system (2.1.5). The manner in which these terms are combined and treated is presented in Section 2.1.2.

2.1.1.3 Well-Balanced Source Discretization

The physically relevant steady-state solution for (2.1.3) is the “lake-at-rest” solution, corresponding to the water surface being perfectly flat and stationary:

$$w = h + B \equiv \text{Const}, \quad h u \equiv 0. \quad (2.1.19)$$

Preserving this particular steady state would guarantee that no artificial surface waves are generated. Our goal is to design a numerical scheme for (2.1.3) that exactly preserves the “lake-at-rest” steady-state solution (2.1.19). This is achieved by selecting a proper discretization of the geometric source term $\bar{S}_j^{(2)}$. Such a discretization was derived for the classical Saint-Venant system in [Kur02; Kur07c; Kur09; CD; Kur18; Che16; Che15; Bol13].

By $\bar{q}_j = \bar{q}_{j-1} = \bar{q}_{j+1} = 0$ and $\bar{w}_j = \bar{w}_{j+1} = \bar{w}_{j-1} = \text{constant}$, we have

$$\begin{aligned} q_{j+\frac{1}{2}}^{\pm} &= q_{j-\frac{1}{2}}^{\pm} = 0 \\ u_{j+\frac{1}{2}}^{\pm} &= u_{j-\frac{1}{2}}^{\pm} = 0 \\ a_{j+\frac{1}{2}}^+ &= -a_{j+\frac{1}{2}}^-, \quad a_{j-\frac{1}{2}}^+ = -a_{j-\frac{1}{2}}^- \\ w_{j+\frac{1}{2}}^- &= w_{j+\frac{1}{2}}^+, \quad w_{j-\frac{1}{2}}^- = w_{j-\frac{1}{2}}^+ \end{aligned}$$

$$\begin{aligned} \frac{H_{j+\frac{1}{2}}^{(2)} - H_{j-\frac{1}{2}}^{(2)}}{\Delta x} &= \\ &= \frac{1}{\Delta x} \left\{ \frac{a_{j+\frac{1}{2}}^+ \left[\left(\frac{q^2}{w-B} \right)^- + \frac{1}{2} g(w^2 - 2wB + B^2)^- \right]_{j+\frac{1}{2}} - a_{j+\frac{1}{2}}^- \left[\left(\frac{q^2}{w-B} \right)^+ + \frac{1}{2} g(w^2 - 2wB + B^2)^+ \right]_{j+\frac{1}{2}}}{a_{j+\frac{1}{2}}^+ - a_{j+\frac{1}{2}}^-} \right\} \\ &+ \frac{1}{\Delta x} \frac{a_{j+\frac{1}{2}}^+ a_{j+\frac{1}{2}}^-}{a_{j+\frac{1}{2}}^+ - a_{j+\frac{1}{2}}^-} [q_{j+\frac{1}{2}}^+ - q_{j+\frac{1}{2}}^-] \\ &- \frac{1}{\Delta x} \left\{ \frac{a_{j-\frac{1}{2}}^+ \left[\left(\frac{q^2}{w-B} \right)^- + \frac{1}{2} g(w^2 - 2wB + B^2)^- \right]_{j-\frac{1}{2}} - a_{j-\frac{1}{2}}^- \left[\left(\frac{q^2}{w-B} \right)^+ + \frac{1}{2} g(w^2 - 2wB + B^2)^+ \right]_{j-\frac{1}{2}}}{a_{j-\frac{1}{2}}^+ - a_{j-\frac{1}{2}}^-} \right\} \\ &- \frac{1}{\Delta x} \frac{a_{j-\frac{1}{2}}^+ a_{j-\frac{1}{2}}^-}{a_{j-\frac{1}{2}}^+ - a_{j-\frac{1}{2}}^-} [q_{j-\frac{1}{2}}^+ - q_{j-\frac{1}{2}}^-] \\ &= \frac{1}{\Delta x} \left\{ \frac{a_{j+\frac{1}{2}}^+ \left[\left(\frac{q^2}{w-B} \right)^- + \frac{1}{2} g(w^2 - 2wB + B^2)^- \right]_{j+\frac{1}{2}} - a_{j+\frac{1}{2}}^- \left[\left(\frac{q^2}{w-B} \right)^+ + \frac{1}{2} g(w^2 - 2wB + B^2)^+ \right]_{j+\frac{1}{2}}}{a_{j+\frac{1}{2}}^+ - a_{j+\frac{1}{2}}^-} \right\} \\ &+ \frac{1}{\Delta x} \frac{a_{j+\frac{1}{2}}^+ a_{j+\frac{1}{2}}^-}{a_{j+\frac{1}{2}}^+ - a_{j+\frac{1}{2}}^-} [q_{j+\frac{1}{2}}^+ - q_{j+\frac{1}{2}}^-] \\ &- \frac{1}{\Delta x} \left\{ \frac{a_{j-\frac{1}{2}}^+ \left[\left(\frac{q^2}{w-B} \right)^- + \frac{1}{2} g(w^2 - 2wB + B^2)^- \right]_{j-\frac{1}{2}} - a_{j-\frac{1}{2}}^- \left[\left(\frac{q^2}{w-B} \right)^+ + \frac{1}{2} g(w^2 - 2wB + B^2)^+ \right]_{j-\frac{1}{2}}}{a_{j-\frac{1}{2}}^+ - a_{j-\frac{1}{2}}^-} \right\} \\ &- \frac{1}{\Delta x} \frac{a_{j-\frac{1}{2}}^+ a_{j-\frac{1}{2}}^-}{a_{j-\frac{1}{2}}^+ - a_{j-\frac{1}{2}}^-} [q_{j-\frac{1}{2}}^+ - q_{j-\frac{1}{2}}^-] \\ &= \frac{1}{2\Delta x} \left[g(w^2 - 2wB + B^2)_{j+\frac{1}{2}}^- - g(w^2 - 2wB + B^2)_{j-\frac{1}{2}}^+ \right] \\ &= -g \frac{\left[w_{j+\frac{1}{2}}^- + w_{j-\frac{1}{2}}^+ - B_{j+\frac{1}{2}} - B_{j-\frac{1}{2}} \right]}{2} \cdot \frac{(B_{j+\frac{1}{2}} - B_{j-\frac{1}{2}})}{\Delta x} \end{aligned}$$

Then for classical Saint-Venant system, we have

$$\bar{S}_j^{(2)} = -g \frac{(w_{j+\frac{1}{2}}^- - B_{j+\frac{1}{2}}) + (w_{j-\frac{1}{2}}^+ - B_{j-\frac{1}{2}})}{2} \cdot \frac{(B_{j+\frac{1}{2}} - B_{j-\frac{1}{2}})}{\Delta x}$$

Meanwhile, for non-hydrostatic Saint-Venant system, both M_j and N_j as defined in Section 2.1.1.2 vanish at this steady state. Then we use this discretization along with an additional atmospheric pressure term for our scheme:

$$\bar{S}_j^{(2)} = -g \frac{(w_{j+\frac{1}{2}}^- - B_{j+\frac{1}{2}}) + (w_{j-\frac{1}{2}}^+ - B_{j-\frac{1}{2}})}{2} \cdot \frac{(B_{j+\frac{1}{2}} - B_{j-\frac{1}{2}})}{\Delta x} + p^a \frac{w_{j+\frac{1}{2}}^- - w_{j-\frac{1}{2}}^+}{\Delta x}. \quad (2.1.20)$$

2.1.2 Time Evolution

We solve the semi-discrete system (2.1.5) by applying the third-order strong stability preserving Runge-Kutta (SSP-RK) method from [Got11; Got01], which can be written as a convex combination of three forward Euler steps. For the purpose of demonstration, we proceed by fully discretizing (2.1.5) according to the forward Euler method, and all results obtained from doing so also apply to the SSP-RK method used in all of our numerical experiments.

When fully discretized by the forward Euler method, the first component of (2.1.5) becomes

$$\bar{w}_j^{n+1} = \bar{w}_j^n - \lambda \left(H_{j+\frac{1}{2}}^{(1)} - H_{j-\frac{1}{2}}^{(1)} \right), \quad (2.1.21)$$

where $\lambda = \Delta t / \Delta x$. Notice that (2.1.21) has no contribution from M , N or S and therefore we may advance the first component *independently* of the second one to obtain the cell averages of w at the new time level, $\{\bar{w}_j^{n+1}\}_{j=1}^N$ (and thus $\{\bar{h}_j^{n+1}\}_{j=1}^N$ since $\bar{h}_j^{n+1} := \bar{w}_j^{n+1} - B_j$, where B_j is given by (2.1.9)). The fully discretized version of the second component of (2.1.5) then becomes

$$\bar{q}_j^{n+1} + \alpha_M M_j^{n+1} = \bar{q}_j^n + \alpha_M M_j^n - \lambda \left(H_{j+\frac{1}{2}}^{(2)} - H_{j-\frac{1}{2}}^{(2)} \right) + \Delta t \bar{S}_j^{(2)} - \Delta t \alpha_N N_j^n, \quad (2.1.22)$$

where all of the terms on the RHS of (2.1.22) are taken at $t = t^n$.

Combining (2.1.13)–(2.1.16) for the discretization of M at time level t^{n+1} and inserting this into the left-hand side (LHS) of (2.1.22) leads to the tridiagonal system $\mathbf{T} = (\tau_{i,j}^{n+1})$, $j = 1, \dots, N$, $i = j-1, j, j+1$ for $\{\bar{q}_j^{n+1}\}$:

$$\bar{q}_j^{n+1} + \alpha_M M_j^{n+1} = \tau_{j-1,j}^{n+1} \bar{q}_{j-1}^{n+1} + \tau_{j,j}^{n+1} \bar{q}_j^{n+1} + \tau_{j+1,j}^{n+1} \bar{q}_{j+1}^{n+1}, \quad (2.1.23)$$

where

$$\begin{aligned}\tau_{j-1,j}^{n+1} &= \alpha_M \left[\frac{\bar{h}_j^{n+1}(B_x)_j - h_{j-\frac{1}{2}}^{n+1}(B_x)_{j-\frac{1}{2}}}{4\Delta x} - \frac{(h_{j-\frac{1}{2}}^{n+1})^3}{3\bar{h}_{j-1}^{n+1}(\Delta x)^2} \right], \\ \tau_{j,j}^{n+1} &= 1 + \alpha_M \left[\frac{h_{j+\frac{1}{2}}^{n+1}(B_x)_{j+\frac{1}{2}} - h_{j-\frac{1}{2}}^{n+1}(B_x)_{j-\frac{1}{2}}}{4\Delta x} + \frac{(h_{j+\frac{1}{2}}^{n+1})^3 + (h_{j-\frac{1}{2}}^{n+1})^3}{3\bar{h}_j^{n+1}(\Delta x)^2} + \frac{(B_x)_j(h_x)_j^{n+1}}{2} + (B_x)_j^2 \right], \\ \tau_{j,j+1}^{n+1} &= \alpha_M \left[\frac{h_{j+\frac{1}{2}}^{n+1}(B_x)_{j+\frac{1}{2}} - \bar{h}_j^{n+1}(B_x)_j}{4\Delta x} - \frac{(h_{j+\frac{1}{2}}^{n+1})^3}{3\bar{h}_{j+1}^{n+1}(\Delta x)^2} \right].\end{aligned}$$

Notice that the term $\bar{q}_j^n + \alpha_M M_j^n$ on the RHS of (2.1.22) is discretized in the same way, but at time level $t = t^n$.

Remark 2.1.4 The addition of the dispersive terms M and N does not affect the well-balanced property of the scheme because these terms vanish at the “lake-at-rest” steady state (2.1.19). The positivity-preserving property of the scheme is also unaffected because these terms do not appear in the first equation of (2.1.1).

Remark 2.1.5 We may write the LHS of (2.1.22) as described by (2.1.23) as $\mathbf{T}\mathbf{q}^{n+1}$, where \mathbf{q}^{n+1} is the vector of the unknown cell averages $\{\bar{q}_j^{n+1}\}_{j=1}^N$. When using free boundary conditions, \mathbf{T} will be strictly tridiagonal, and it is well-known that in this case, the linear algebraic system (2.1.22) can be efficiently solved using the LU decomposition; see, e.g., [Bur05; Tre97] for details. In the case of periodic boundary conditions, the matrix \mathbf{T} becomes circulant and one may still take advantage of the banded structure of the matrix by implementing the Sherman-Morrison algorithm proposed in [She50].

2.2 Numerical Experiments

In the following experiments, we will examine the role that the non-hydrostatic pressure terms play in the long-time propagation of water waves. We will use the classical Saint-Venant system for comparison, which is simply (2.1.3) with $\alpha_M = \alpha_N = p^a \equiv 0$. In all of the experiments, we take $p^a \equiv 0$, take the minmod parameter $\theta = 1.3$, and consider free boundary conditions.

Example 1 — Solitary Wave Propagation

In the first example (taken from [Bri11]), we study propagation of the wave given by the following initial data:

$$h(x, 0) = 1 + \frac{1}{10} \operatorname{sech}^2\left(\sqrt{\frac{3}{40}}(x - 70)\right), \quad u(x, 0) = \frac{\sqrt{g}}{10} \operatorname{sech}^2\left(\sqrt{\frac{3}{40}}(x - 70)\right),$$

over a flat bottom topography with $B(x) \equiv -0.1$. We take $g = 9.81$ and divide the computational domain $[0, 400]$ into 3200 finite-volume cells. According to [Bri11], in the case when $\alpha_M = \alpha_N = 1$, these data correspond to a solitary wave, which is a single elevation of water surface above an undisturbed surrounding, which is neither preceded nor followed by any free surface disturbances. In nature, solitary waves are a kind of stable wave. It's a well-studied numerical example for testing an algorithms to describe waves' long-time propagation.

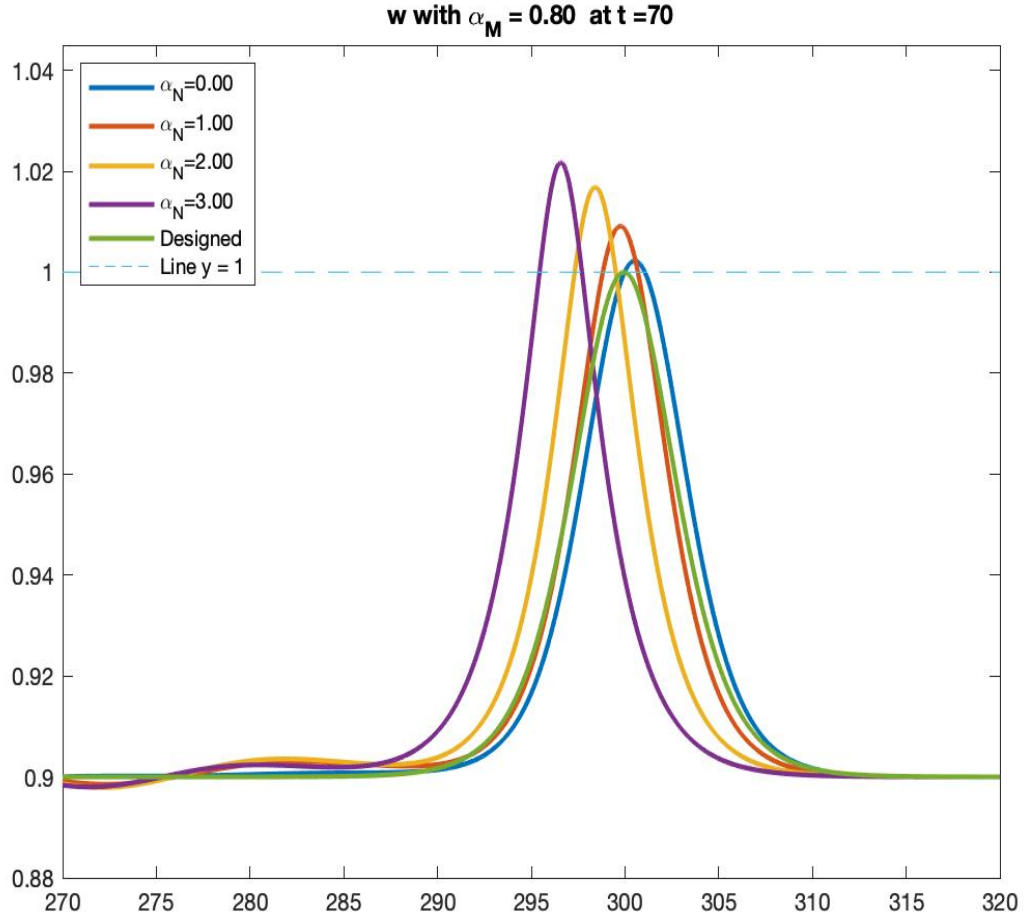


Figure 2.2.1 Example 1: Time evolution of the water surface for $\alpha_M = 0.8$ and $\alpha_N = 0, 1, 2, 3$.

If arbitrary α_M and α_N are chosen, we have degrees of freedom to be 2. It's hard to try out every combination. We will first fix $\alpha_M = 0.8$ and set $\alpha_N = 0, 1, 2, 3$ and then evolve solutions until $t = 70$. The numerical result is shown in Figure 2.2.1. The green 'Designed' wave is the designed solitary Wave at $t = 70$. Its top is less than 1. The blue wave faster than solitary wave is with $\alpha_N = 0$. The red line right above solitary wave is with $\alpha_N = 1$. The yellow and purple wave are with $\alpha_N = 2$ and $\alpha_N = 3$,

respectively. This means that if α_M is fixed, with the increasing of α_N , the numerical wave will travel slower but with an increasing height. This suggests around $\alpha_N = 1$, numerical waves should have same wave speed as the solitary wave.

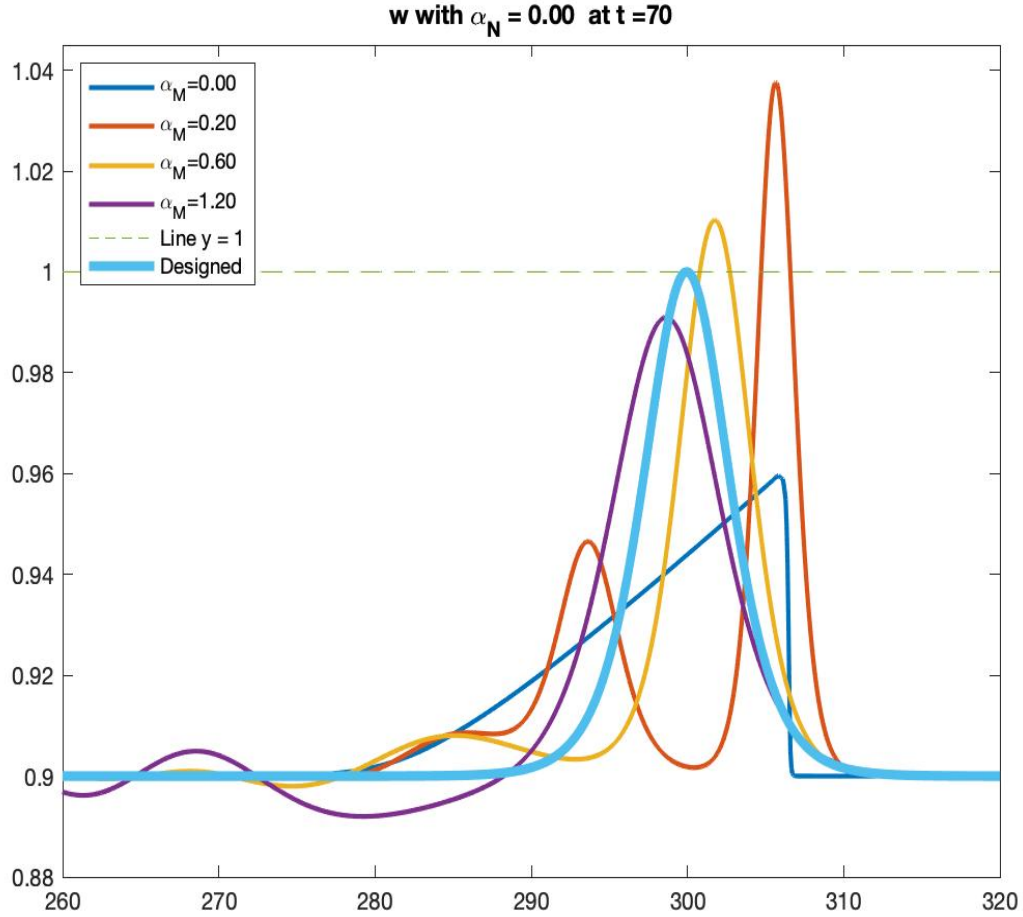


Figure 2.2.2 Example 1: Time evolution of the water surface for $\alpha_N = 0$ and $\alpha_M = 0, 0.2, 0.6, 1.2$.

We can fix $\alpha_N = 0$, set $\alpha_M = 0, 0.2, 0.6, 1.2$, and then evolve solutions until $t = 70$. The numerical result is shown in Figure 2.2.2. The (fat) light blue 'Designed' wave is the designed solitary wave at $t = 70$. Its top is at 1. The dark blue wave with the lowest height is with $\alpha_M = 0$, namely classical Saint-Venant system. A significant decay in amplitude can be seen. And the wave eventually becomes a shock. The red line that reach as 1.04 is with $\alpha_M = 0.2$. This drastic change in amplitude meaning the appearance of term M in (2.1) introduces dispersion to our numerical results. The yellow and purple wave are with $\alpha_M = 0.6$ and $\alpha_N = 1.2$, respectively. If we have $\alpha_M \rightarrow 1$, the wave is more close to the designed solitary wave.

After trying different pairs of (α_M, α_N) , we fix $\alpha_M = \alpha_N$ so that the choosing of parameters are not random.

Then we compute the solutions until the final time $t = 50$ and demonstrate how the speed, magnitude and shape of the wave is affected by the choice of α_M and α_N . We begin with the classical Saint-Venant system ($\alpha_M = \alpha_N = 0$) and then start adding the non-hydrostatic pressure terms by gradually increasing α_M and α_N . We first observe that for a very small value of $\alpha_M = \alpha_N = 0.01$, the solutions of hydrostatic and non-hydrostatic systems are almost the same except for a small change of the shape of the wave at the top; see Figure 2.2.3. We then further increase α_M and α_N to 0.02–0.05 and observe that up to the intermediate times (around $t = 20$) the solution magnitude increases before decreasing at later times. One can also observe a substantial change in the shape of the wave as a dispersive wave structure clearly develops for $\alpha_M = \alpha_N = 0.04$ and 0.05; see Figure 2.2.4. When α_M and α_N are increased up to 0.01, the magnitude of the wave seem to increase up to about $t = 30$ and then it stabilizes; for even larger values of $\alpha_M = \alpha_N = 0.25$ and 0.5, the dispersive wave structure starts disappearing and the amplitude growth becomes less pronounced; and for $\alpha_M = \alpha_N = 1$ the expected solitary wave structure is numerically recovered; see Figure 2.2.5. Finally, in Figure 2.2.6, we show the solution obtained for larger dispersive coefficients $\alpha_M = \alpha_N = 2$ and 5. As one can see, in these two cases the magnitude of the wave decreases and a wave train is clearly formed.

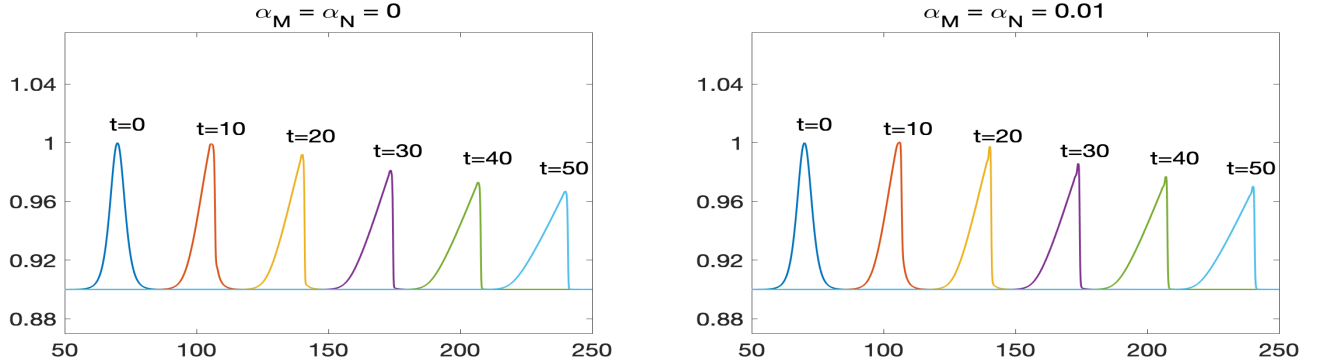


Figure 2.2.3 Example 1: Time evolution of the water surface for $\alpha_M = \alpha_N = 0$ (left) and 0.01 (right).

We also perform an experimental convergence study of the proposed method. To this end, we take the solution computed with $\alpha_M = \alpha_N = 1$ at time $t = 0.1$ on different grids and compare them with the reference solution obtained with 51200 finite-volume cells. The results are reported in Tables 2.2.1 and 2.2.2 for w and q , respectively. as One can observe, the expected second order of convergence is achieved in both L^∞ -, L^1 - and L^2 -norms.

Example 2 — Large-Scale Tsunami-Like Wave Propagation

In the second example, we consider a wave that was created using a Savage-Hutter type model of submarine landslides and generated tsunami waves. This model is governed by a two-layer system

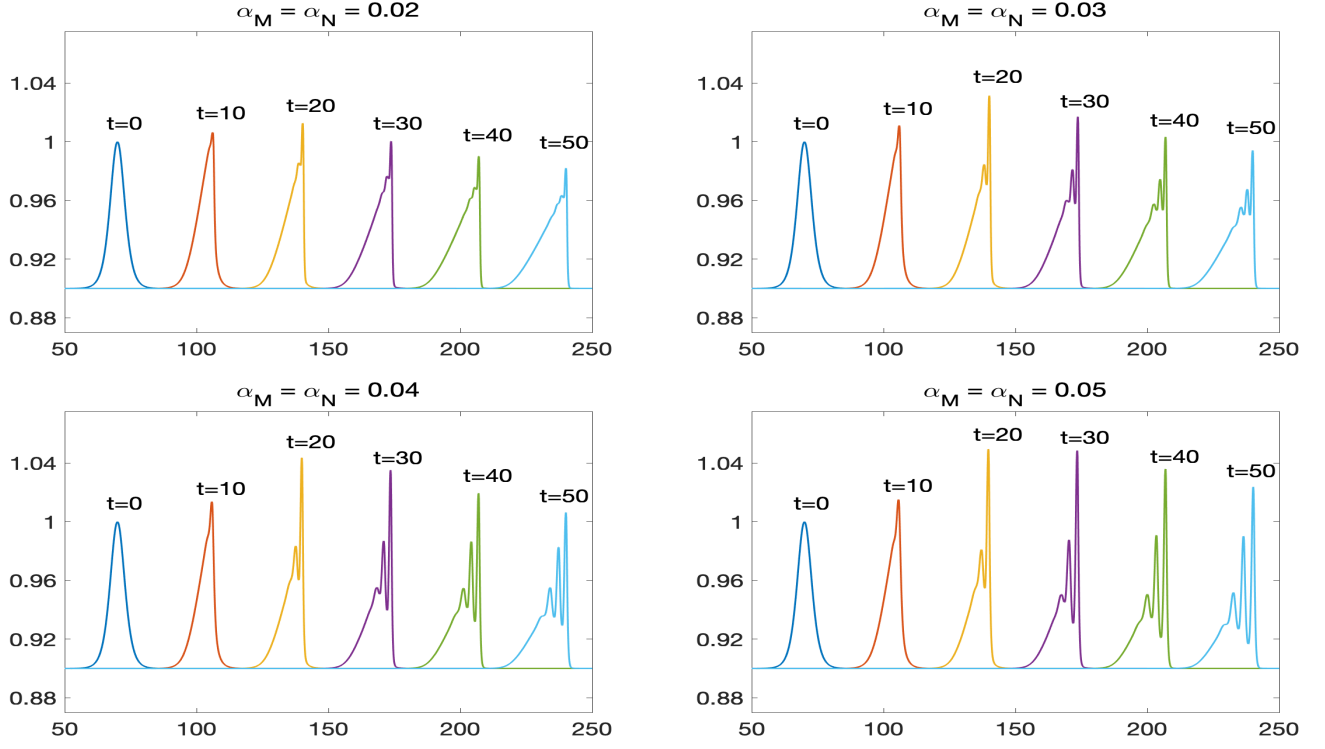


Figure 2.2.4 Example 1: Time evolution of the water surface for $\alpha_M = \alpha_N = 0.02$ (top left), 0.03 (top right), 0.04 (bottom left) and 0.05 (bottom right).

in which the lower layer is considered to be a fluid-granular mixture that has a larger density than the upper layer, which is water. The lower layer slides down the slope of the solid bottom, and the through momentum exchange causes waves to form at the water surface. For more details of this system and associated numerical methods, see [FN08; Hei01; Kur14].

The initial data are obtained from [Kur14], where a submarine landslide on the ocean floor creates surface waves traveling to the left and right. We choose the right-moving wave at $t = 0.3$ as the initial condition for the non-hydrostatic system (2.1.3) and the following bottom topography function:

$$B(x) = \begin{cases} -5, & x < 0, \\ -5 + \sum_{i=1}^5 C_i \sin(\pi(x - S_i)/L_i), & x \geq 0, \end{cases} \quad (2.2.1)$$

where the parameters C_i , S_i and L_i are given in Table 2.2.3. The initial water surface $w(x, 0)$ and velocity $u(x, 0)$ are plotted in Figure 2.2.7 and a nonflat part of the bottom topography is shown in Figure 2.2.8. In this example, the length scale is kilometers and the time scale is hours, so we take the corresponding gravity to be $g = 271008 \text{ km/h}^2$. The computational domain, $[-150, 2200]$, is divided into 18800 finite-volume cells.

We compute the solutions until the final time $t = 2$ and as in Example 1 study the dependence of the computed solutions on the choice of the dispersion parameters α_M and α_N . We begin with the classical Saint-Venant system ($\alpha_M = \alpha_N = 0$) and plot the obtained results in Figure 2.2.9. As one

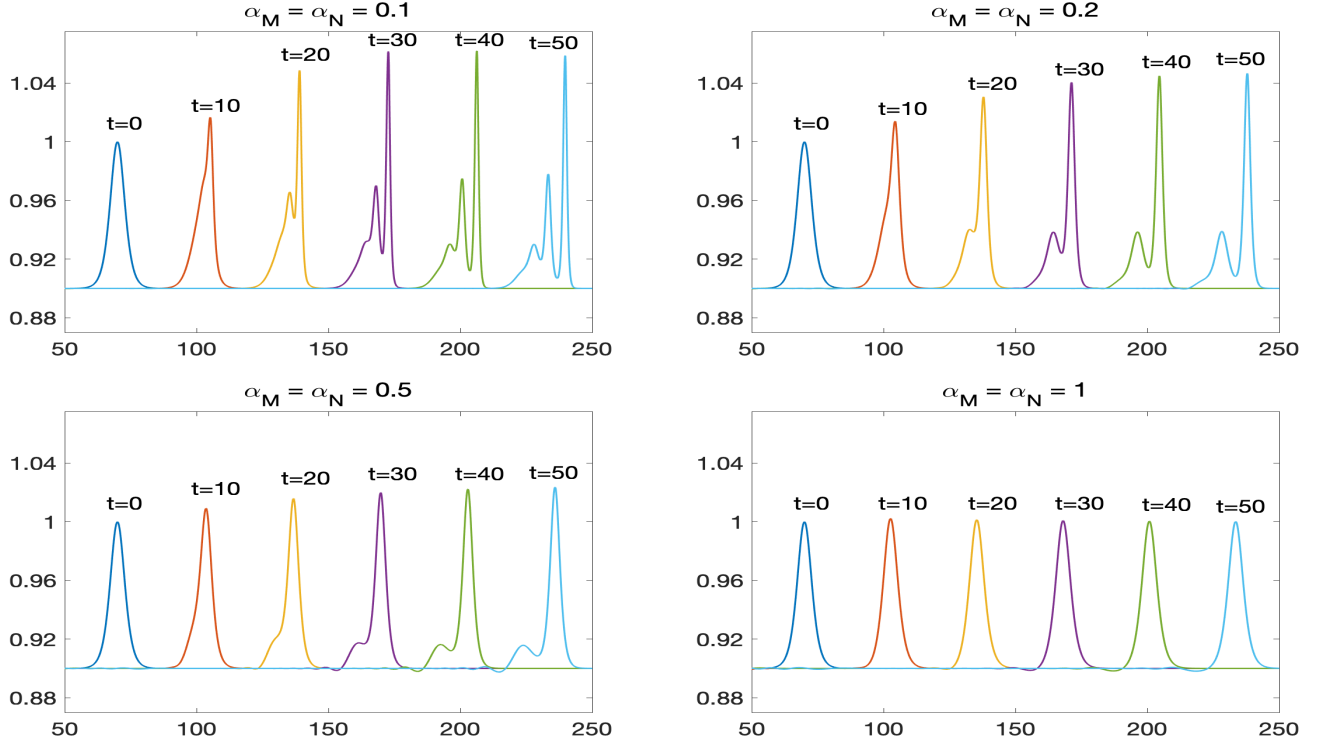


Figure 2.2.5 Example 1: Time evolution of the water surface for $\alpha_M = \alpha_N = 0.1$ (top left), 0.25 (top right), 0.5 (bottom left) and 1 (bottom right).

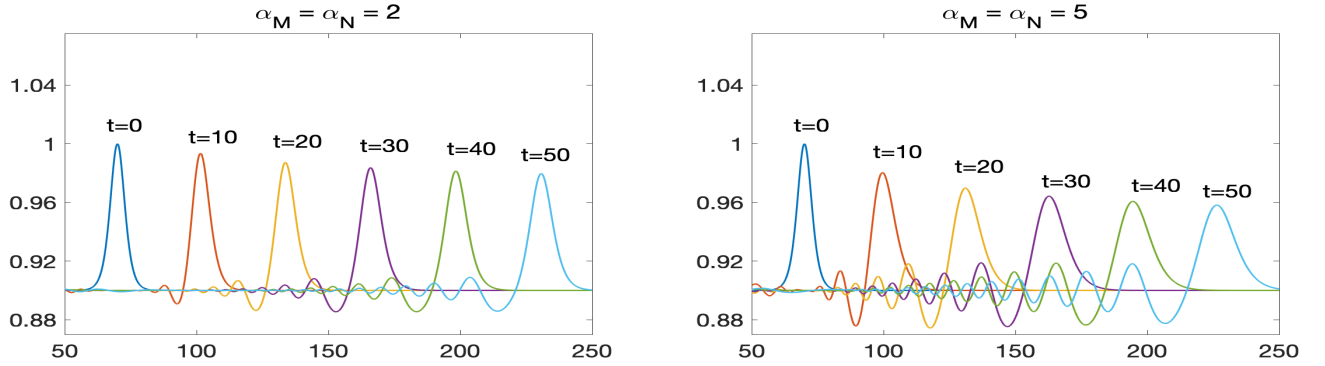


Figure 2.2.6 Example 1: Time evolution of the water surface for $\alpha_M = \alpha_N = 2$ (left) and 5 (right).

can see, there are many small waves created behind the large wave as a result of the nonflat bottom topography, but the structure of the larger waves does not seem to be significantly affected. Figure 2.2.10 shows time snapshots of the numerical solutions of the non-hydrostatic system (2.1.3) with $\alpha_M = \alpha_N = 0.05, 0.1, 0.15$ and 0.2 . As expected, dispersive wave trains start appearing and become more pronounced for larger values of α_M and α_N .

Table 2.2.1 L^∞ -, L^1 - and L^2 -errors in w and the corresponding experimental rates of convergence.

Number of cells	L^∞ -error	Rate	L^1 -error	Rate	L^2 -error	Rate
400	2.94e-04	–	1.97e-04	–	1.47e-04	–
800	9.23e-05	1.67	4.46e-05	2.14	3.54e-05	2.06
1600	1.51e-05	2.61	8.99e-06	2.31	5.53e-06	2.68
3200	2.55e-06	2.56	2.04e-06	2.14	1.01e-06	2.45
6400	6.63e-07	1.94	5.13e-07	1.99	2.31e-07	2.13
12800	1.75e-07	1.92	1.49e-07	1.79	5.88e-08	1.97

Table 2.2.2 L^∞ -, L^1 - and L^2 -errors in q and the corresponding experimental rates of convergence.

Number of cells	L^∞ -error	Rate	L^1 -error	Rate	L^2 -error	Rate
400	2.28e-04	–	4.12e-04	–	1.90e-04	–
800	5.48e-05	2.06	1.03e-04	2.00	4.62e-05	2.04
1600	1.34e-05	2.04	2.56e-05	2.01	1.12e-05	2.05
3200	2.89e-06	2.21	6.49e-06	1.98	2.78e-06	2.01
6400	7.31e-07	1.98	1.65e-06	1.98	6.94e-07	2.00
12800	1.70e-07	2.10	4.14e-07	1.99	1.71e-07	2.02

Table 2.2.3 Parameters used in for the bottom topography functions (2.2.1) and (2.2.2).

i	1	2	3	4	5
C_i	0.1	0.3	0.5	0.1	1
S_i	0	2	3	0	80
L_i	40	70	100	10	2500

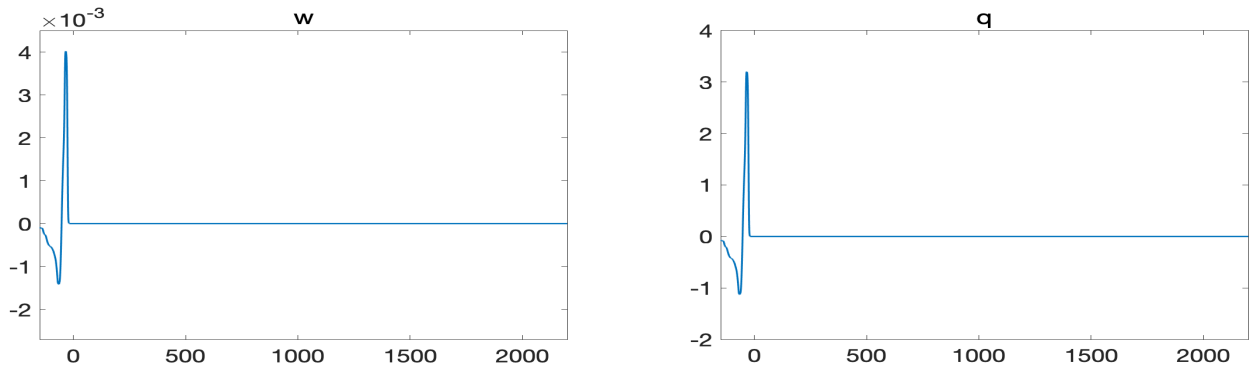


Figure 2.2.7 Example 2: Initial water surface (left) and discharge (right).

Example 3 — On-Shore Dynamics of the Large Wave

Tsunami waves are characterized by having a relatively low amplitude, large wavelength, and large characteristic wave speed, see, e.g., [Bry08; LeV11b; Ort00]. The amplitude of a tsunami wave can

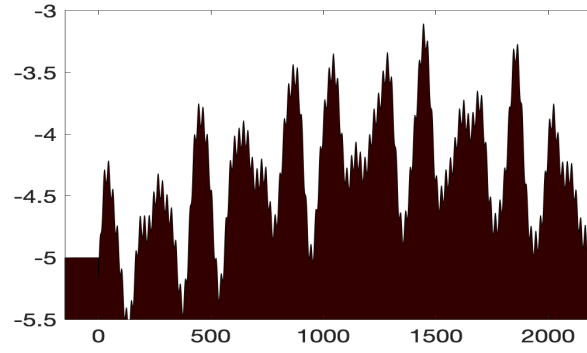


Figure 2.2.8 Example 2: The bottom topography function (2.2.1).

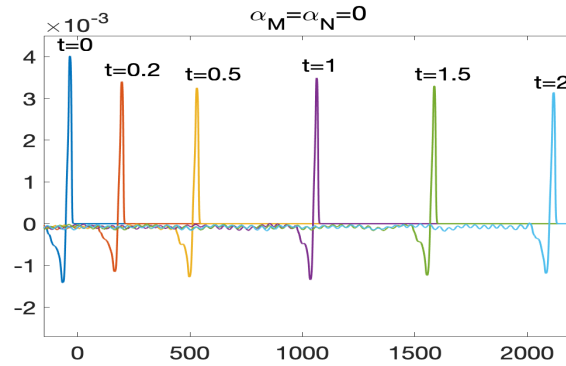


Figure 2.2.9 Example 2: Time evolution of the water surface for the classical Saint-Venant system ($\alpha_M = \alpha_N = 0$).

be so small that it may not even be noticed by a ship traveling through it in deep water. Because of their speed and wavelength, however, these waves contain a tremendous amount of energy. When the depth of the water decreases (in the beginning of the on-shore arrival stage of tsunami wave propagation), tsunamis undergo a process called wave shoaling, in which the wave slows down and the wavelength decreases. In order to conserve energy, it is transformed from kinetic to potential energy and the wave amplitude increases. This potential energy can then be released in disastrous fashion when the wave comes to shore. It is therefore very important to have accurate models and corresponding numerical methods for tsunami waves in order to mitigate any catastrophe that may result.

In order to further emphasize the difference between hydrostatic and non-hydrostatic solutions, we let the computed waves to approach the shore. We take the solutions at time $t = 2$ shown in Figure 2.2.9 for $\alpha_M = \alpha_N = 0$ and Figure 2.2.10 for $\alpha_M = \alpha_N = 0.2$ as initial data in the domain $[1000, 3000]$

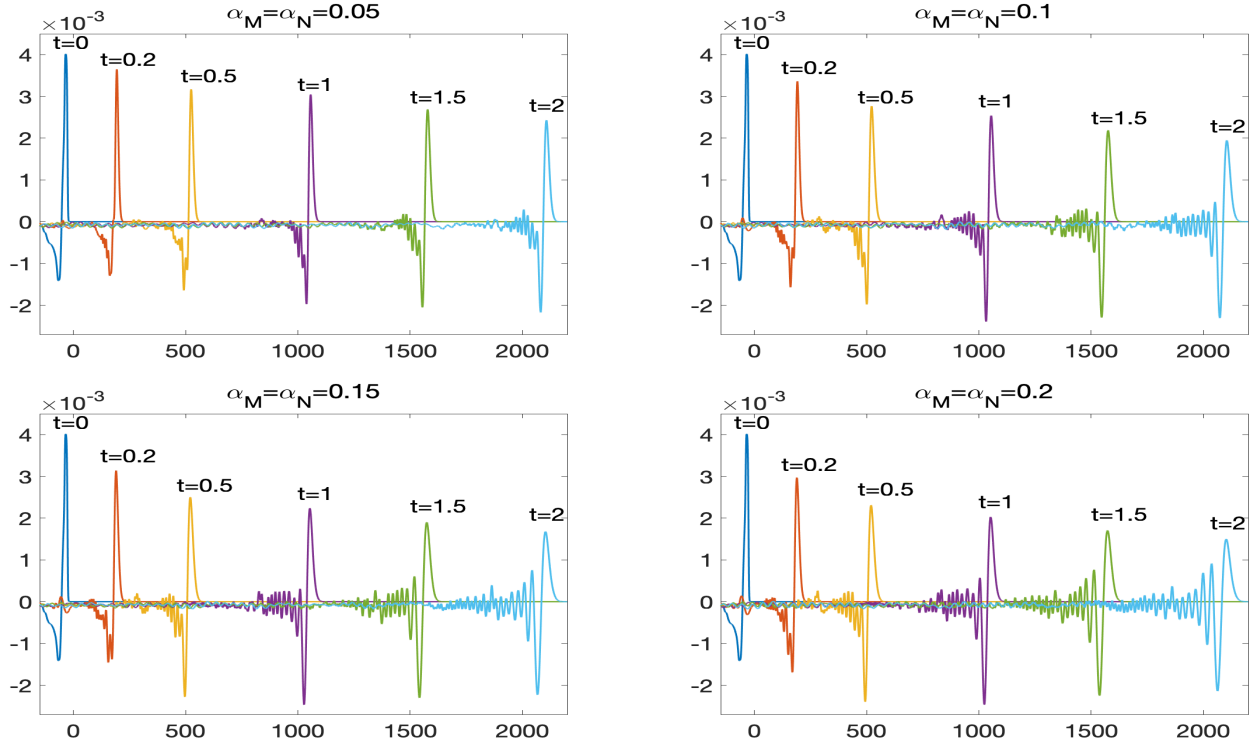


Figure 2.2.10 Example 2: Time evolution of the water surface for $\alpha_M = \alpha_N = 0.05$ (top left), 0.1 (top right), 0.15 (bottom left) and 0.2 (bottom right).

(divided into 16000 finite-volume cells) along with following bottom topography function:

$$B(x) = \begin{cases} -5 + \sum_{i=1}^5 C_i \sin(\pi(x - S_i)/L_i), & x < 2200, \\ -4.86 + 2.75e^{\left[-300\left(1 - \frac{x}{2600}\right)\right]}, & 2200 < x \leq 2600, \\ 10^{-10} - 2.11e^{\left[-300\left(\frac{x}{2600} - 1\right)\right]}, & x > 2600, \end{cases} \quad (2.2.2)$$

where the coefficients C_i , S_i , and L_i are given in Table 2.2.3. We notice that near the shore, the function B is simply a smooth curve that increases from -4.86 to almost zero; see Figure 2.2.11.

In order to accurately capture the on-shore arrival of the waves, we have implemented a special well-balanced reconstruction of wet/dry fronts from [Bol13] and computed both the hydrostatic and non-hydrostatic solutions until the final time $t = 3$. We present several time snapshots of the computed water surface in Figure 2.2.12. As one can see, both dispersive and non-dispersive waves go through the shoaling process where they slow down and increase in height, and eventually arrive on shore. If we look closer (Figure 2.2.13), we see that the trailing waves actually impact how the wave comes to shore: The front of the non-hydrostatic solution is about 10–20 km behind the hydrostatic one. This suggests that the non-hydrostatic terms *must* be included in a tsunami model if one wants to accurately represent the ultimate outcome of the tsunami waves.

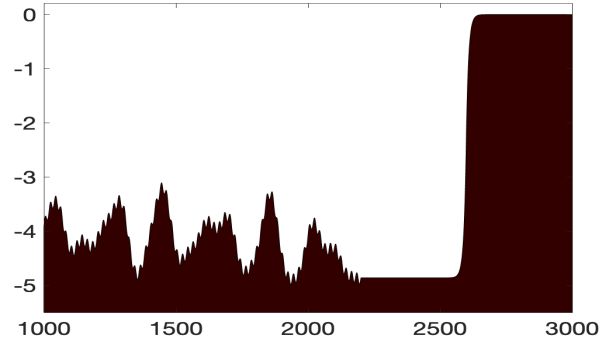


Figure 2.2.11 Example 3: The bottom topography function (2.2.2).

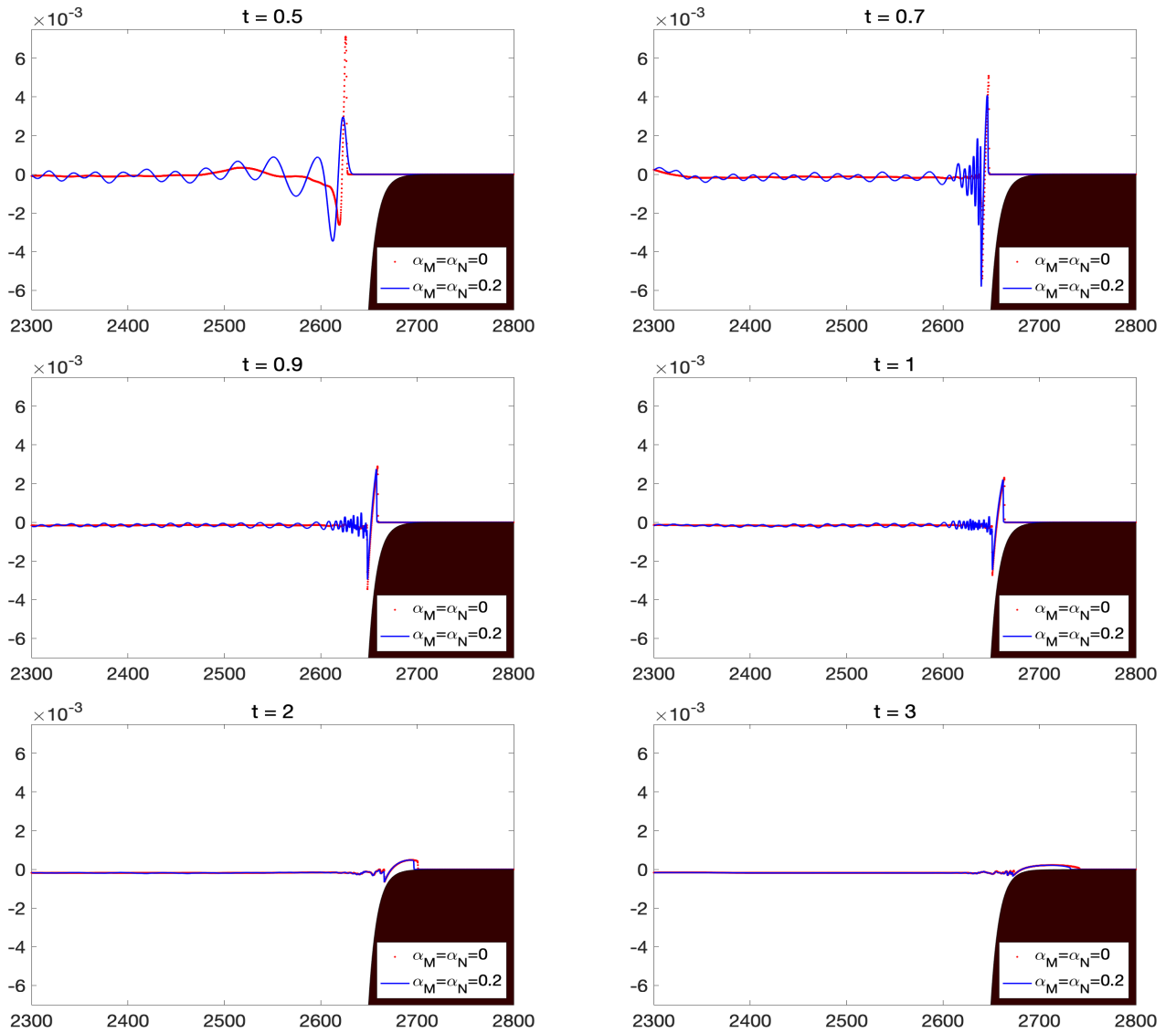


Figure 2.2.12 Example 3: On-shore arrival of the tsunami-like waves in the hydrostatic ($\alpha_M = \alpha_N = 0$) and non-hydrostatic with $\alpha_M = \alpha_N = 0.2$ regimes.

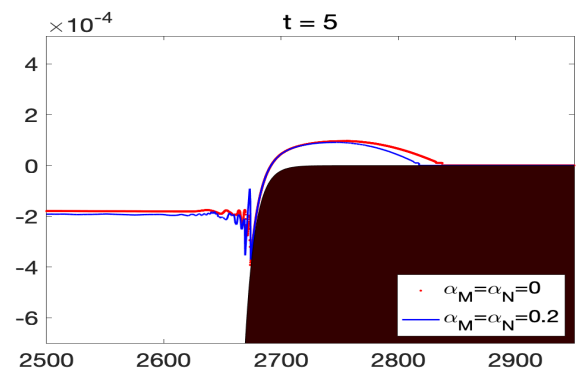
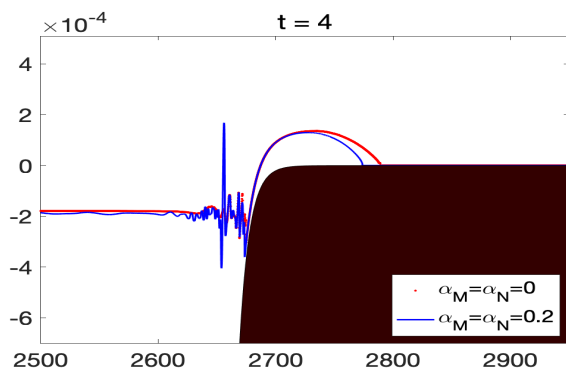
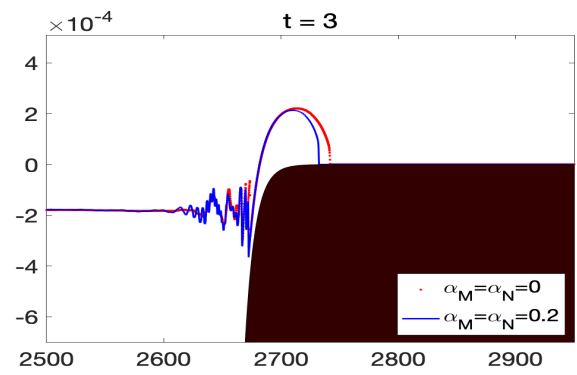
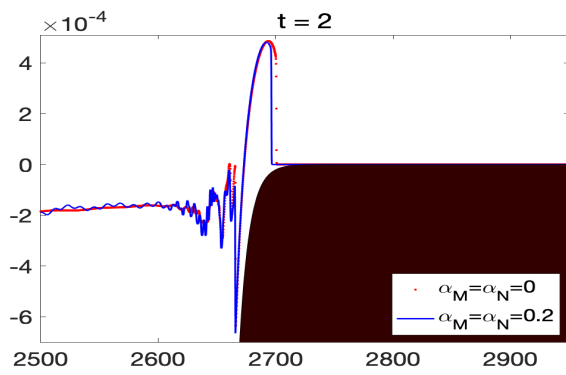


Figure 2.2.13 Example 3: Same as Figure 2.2.12, but zoomed in.

CHAPTER

3

ATMOSPHERIC FLOW EQUATIONS WITH GRAVITY

The main part of this chapter have been submitted to Communications in Computational Physics,[Che21]

In this chapter, we simulate gravitationally stratified atmospheric flows governed by the compressible Euler equations in irregular domains. Cartesian grids showed low accuracy and slow (incorrect compared to reference [Kle09] in our simulation) flow rates near irregular boundaries. The reason is that the use of such rectangular grids that intersect with the irregular boundaries leads to the generation of arbitrarily small and highly distorted computational cells adjacent to the boundaries of the domain. A more stable and accurate scheme is needed.

Several techniques were proposed to address this problem. In the older works, the terrain-following coordinate approach was widely used in atmospheric simulations; see, e.g., [Phi57; GC75; Sim81]. It normalizes the vertical coordinate by the fluid depth to incorporate the topography of domains into the studied models. However, this approach typically leads to significant truncation errors near boundaries, especially when the flow contains steep gradients; see, e.g., [Jan89; Sun76]. Alternatively, as we mentioned before, one may use Cartesian-grid based methods, which are relatively simple, but suffer from the appearance of arbitrarily small and highly distorted cells adjacent to the boundaries of the domain. Such cut cells may lead to stability and efficiency issues for numerical methods and therefore require special techniques; see, e.g., [Kle09; GB06; Bra20; Mit05; Gok18; Ber12] and references therein. Triangular, quadrilateral and cell-vertex polygonal meshes can also be used to conduct simulations in domains with irregular boundaries. It should be observed that unstructured meshes with different polygons can accurately represent irregular

boundaries and thus provide with a flexible tool to handle regions with steep topographic gradients.

In this chapter, we develop a well-balanced method for the system (3.1.1), (3.1.2) in two steps. We first rewrite the studied system in terms of the perturbation variables and thus ensure that the resulting method is well-balanced. We then introduce a structured quadrilateral mesh, which is specifically designed for every considered irregular domain. Finally, the rewritten system is numerically integrated using the second-order semi-discrete central-upwind scheme, which was introduced in [Kur07a; Kur01b; Kur00c] as a robust and highly accurate “black-box solver” for general multidimensional system of hyperbolic conservation and balance laws (including the compressible Euler equations with gravitation [Che18]) on Cartesian grids, and then extended to structured and unstructured quadrilateral meshes in [Kur17; Kur20; Shi16].

The proposed method is tested in a number of numerical experiments, including the buoyant bubble rising and interacting with an (zeppelin) obstacle and the Lee wave generation due to topography. The obtained numerical results demonstrate high resolution and robustness of the proposed computational approach.

3.1 Mathematical Model

Gravitationally stratified flows in a compressible medium are widely used in atmospheric models to predict weather and climate. These models are typically characterized as variants of the compressible Euler equations with gravity. Here, we focus on studying the following two-dimensional (2-D) system proposed in [Kle09]:

$$\begin{cases} \rho_t + (\rho u)_x + (\rho v)_y = 0, \\ (\rho u)_t + (\rho u^2 + p)_x + (\rho uv)_y = 0, \\ (\rho v)_t + (\rho vu)_x + (\rho v^2 + p)_y = -\rho g, \\ (\rho \theta)_t + (\rho \theta u)_x + (\rho \theta v)_y = 0, \end{cases} \quad (3.1.1)$$

where x and y are spatial variables, t is a time, $\rho(x, y, t)$, $u(x, y, t)$, $v(x, y, t)$ and $\theta(x, y, t)$ are the density, horizontal, vertical velocities and potential temperature, respectively, and g is the acceleration due to gravity. The air flow is assumed to be an ideal gas satisfying the equation of state:

$$p = (\rho \theta)^\gamma, \quad (3.1.2)$$

where p is the pressure and $\gamma = 1.4$ is the specific heat ratio.

Time-independent (steady-state or equilibrium) solutions of the system (3.1.1) play an important role as many atmospheric phenomena are described by small perturbations of the steady states. In particular, one of the physically relevant equilibria is the motionless hydrostatic one:

$$u = v \equiv 0, \quad p_x \equiv 0, \quad p_y = -\rho g. \quad (3.1.3)$$

Capturing small perturbations of (3.1.3) numerically is a challenging task since at a large scale or on

a coarse grid the magnitude of such perturbations may be smaller than the size of truncation errors.

3.2 Model Description and Numerical Method

In this section, we follow the idea introduced in [Bot04] and achieve the well-balanced property of proposed numerical method by rewriting the system (3.1.1), (3.1.2) in terms of the perturbation variables. To this end, we first denote the steady-state solution (3.1.3) by $\rho_s(y)$ and $p_s(y)$ with the corresponding potential temperature $\theta_s(y) = [p_s(y)]^{1/\gamma} / \rho_s(y)$, and introduce the perturbation variables ρ' , u' , v' and θ' so that

$$\rho = \rho_s + \rho', \quad u = u', \quad v = v', \quad \theta = \theta_s + \theta', \quad p' = [(\rho_s + \rho')(\theta_s + \theta')]^\gamma - p_s. \quad (3.2.1)$$

where p' is obtained from the equation of state (3.1.2). We then rewrite the system (3.1.1) in the following form:

$$\begin{cases} \rho'_t + (\rho u')_x + (\rho v')_y = 0, \\ (\rho u')_t + [\rho(u')^2 + p']_x + (\rho u' v')_y = 0, \\ (\rho v')_t + (\rho v' u')_x + [\rho(v')^2 + p']_y = -\rho' g, \\ (\rho \theta)_t + (\rho \theta u')_x + (\rho \theta v')_y = 0. \end{cases} \quad (3.2.2)$$

The main advantage of the system (3.2.2) over its original counterpart (3.1.1) is that when the solution is at the steady state, the perturbation variables vanish and this makes it easy to design a well-balanced numerical method. In this chapter, we use the second-order semi-discrete central-upwind scheme as it is described in [Kur20] with the only exception that the piecewise linear reconstruction is now performed not for the conservative variables $\mathbf{U} := (\rho', \rho u', \rho v', \rho \theta)$, but for the perturbation variables $\mathbf{U}' := (\rho', u', v', \theta')$, which remain constant (zero) at the steady state (3.1.3).

The central-upwind scheme can be briefly described as follows. Let us assume that the computational domain is covered with a structured quadrilateral mesh consisting of cells $C_{j,k}$ with vertices $(x_{j-\frac{1}{2},k-\frac{1}{2}}, y_{j-\frac{1}{2},k-\frac{1}{2}})$, $(x_{j-\frac{1}{2},k+\frac{1}{2}}, y_{j-\frac{1}{2},k+\frac{1}{2}})$, $(x_{j+\frac{1}{2},k-\frac{1}{2}}, y_{j+\frac{1}{2},k-\frac{1}{2}})$ and $(x_{j+\frac{1}{2},k+\frac{1}{2}}, y_{j+\frac{1}{2},k+\frac{1}{2}})$, the center of mass $(x_{j,k}, y_{j,k})$, and area $|C_{j,k}|$. We also assume that the computed cell averages,

$$\bar{U}_{j,k}(t) \approx \frac{1}{|C_{j,k}|} \iint_{C_{j,k}} U(x, y, t) dx dy.$$

are available at a certain time level t and we use them to approximate the corresponding point values of \mathbf{U}' at the center of mass of cell $C_{j,k}$:

$$\rho'_{j,k} = \bar{\rho}'_{j,k}, \quad u'_{j,k} = \frac{(\overline{\rho u'})_{j,k}}{\rho_{j,k}}, \quad v'_{j,k} = \frac{(\overline{\rho v'})_{j,k}}{\rho_{j,k}}, \quad \theta'_{j,k} = \frac{(\overline{\rho \theta})_{j,k}}{\rho_{j,k}} - \theta_s(x_{j,k}, y_{j,k}).$$

Here, $\rho_{j,k} = \bar{\rho}'_{j,k} + \rho_s(x_{j,k}, y_{j,k})$ and the dependence of the indexed quantities on t has been omitted for the sake of brevity.

If we denote $U_s := (\rho_s, 0, 0, \rho_s \theta_s)$, then (3.2.2) can be written as

$$U_t + F(U, U_s)_x + G(U, U_s)_y = S(U'), \quad (3.2.3)$$

where

$$\begin{aligned} F(U, U_s) &= \left(\rho u', \rho (u')^2 + p', \rho v' u', \rho \theta u' \right)^T, \\ G(U, U_s) &= \left(\rho v', \rho v' u', \rho (v')^2 + p', \rho \theta v' \right)^T, \\ S(U') &= (0, 0, -\rho' g, 0)^T. \end{aligned}$$

Equipped with the point values $\{U'_{j,k}\}$, we perform the piecewise linear reconstruction from [Kur20] for U' and then obtain all of the required point values of U using (3.2.1). The obtained point values are, in turn, used to complete the construction of the second-order semi-discrete central-upwind scheme; see 3.2.1, [Kur20] for details. The resulting system of ODEs is integrated in time using the three-stage third-order strong stability-preserving Runge-Kutta (SSP-RK3) method; see, e.g., [Got11; Got01].

Remark 3.2.1 Notice that the gravitational source term on the right-hand side of (3.2.2) vanishes at the steady state (3.1.3). Therefore, approximating its cell averages using the midpoint rule leads to a well-balanced discretization. Readers can refer to [Che18; LeV11a; Xin13; Bot04; GB06; Kle09; Kli19; K p16; Gab18] for well-balanced numerical methods capable of exactly preserving motionless hydrostatic steady-states solutions.

3.2.1 Two-Dimensional Semi-Discrete Scheme

3.2.1.1 Structured Mesh Generation

Computational domain is designed to be covered with a structured irregular quadrilateral mesh consisting of cells $C_{j,k}$ with area $|C_{j,k}|$, and notations of related cell data are given below (see Figure 3.2.1):

$z_{j+\frac{1}{2}, k+\frac{1}{2}} := (x_{j+\frac{1}{2}, k+\frac{1}{2}}, y_{j+\frac{1}{2}, k+\frac{1}{2}}):$	cell vertices,
$z_{j,k} := (x_{j,k}, y_{j,k}):$	center of mass of $C_{j,k}$,
$\ell_{j+\frac{1}{2}, k} := z_{j+\frac{1}{2}, k+\frac{1}{2}} - z_{j+\frac{1}{2}, k-\frac{1}{2}} :$	length of the edge $z_{j+\frac{1}{2}, k-\frac{1}{2}} z_{j+\frac{1}{2}, k+\frac{1}{2}}$,
$z_{j+\frac{1}{2}, k} := \frac{1}{2}(z_{j+\frac{1}{2}, k+\frac{1}{2}} + z_{j+\frac{1}{2}, k-\frac{1}{2}}):$	midpoint of the edge $z_{j+\frac{1}{2}, k-\frac{1}{2}} z_{j+\frac{1}{2}, k+\frac{1}{2}}$,
$n_{j+\frac{1}{2}, k} := (\cos(\theta_{j+\frac{1}{2}, k}), \sin(\theta_{j+\frac{1}{2}, k})):$	the unit outer normal vector to the edge $z_{j+\frac{1}{2}, k-\frac{1}{2}} z_{j+\frac{1}{2}, k+\frac{1}{2}}$,
$\ell_{j, k+\frac{1}{2}} := z_{j+\frac{1}{2}, k+\frac{1}{2}} - z_{j-\frac{1}{2}, k+\frac{1}{2}} :$	length of the edge $z_{j-\frac{1}{2}, k+\frac{1}{2}} z_{j+\frac{1}{2}, k+\frac{1}{2}}$,
$z_{j, k+\frac{1}{2}} := \frac{1}{2}(z_{j+\frac{1}{2}, k+\frac{1}{2}} + z_{j-\frac{1}{2}, k+\frac{1}{2}}):$	midpoint of the edge $z_{j-\frac{1}{2}, k+\frac{1}{2}} z_{j+\frac{1}{2}, k+\frac{1}{2}}$,
$n_{j, k+\frac{1}{2}} := (\cos(\theta_{j, k+\frac{1}{2}}), \sin(\theta_{j, k+\frac{1}{2}})):$	the unit outer normal vector to the edge $z_{j-\frac{1}{2}, k+\frac{1}{2}} z_{j+\frac{1}{2}, k+\frac{1}{2}}$.

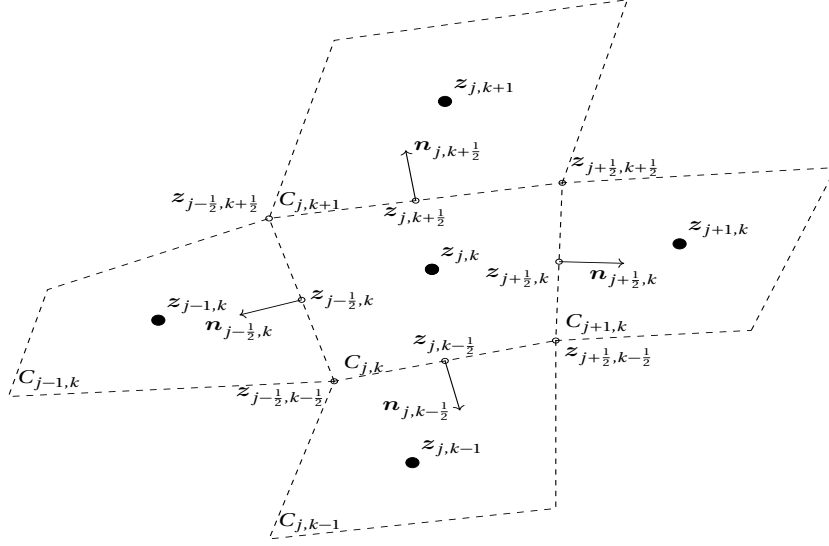


Figure 3.2.1 Quadrilateral cell $C_{j,k}$ with its four neighbors

3.2.1.2 Reconstruction

We assume cell averages of perturbation variables at time t are given in the cell $C_{j,k}$:

$$\overline{U'}_{j,k}(t) := \frac{1}{|C_{j,k}|} \iint_{C_{j,k}} U'(x, y, t) dx dy.$$

Together with cell data and cell averages, we can first construct a second-order linear piecewise polynomial interpolation:

$$\mathbf{P}_{j,k}(x, y) := \overline{U'}_{j,k} + (U'_x)_{j,k}(x - x_{j,k}) + (U'_y)_{j,k}(y - y_{j,k}), \quad (3.2.4)$$

$$\mathbf{P}(x, y) := \sum_{j,k} \mathbf{P}_{j,k}(x, y) \chi_{C_{j,k}}, \quad (3.2.5)$$

where $\chi_{C_{j,k}}$ is the characteristic function of the cell $C_{j,k}$ and the numerical derivatives $(U'_x)_{j,k}$ and $(U'_y)_{j,k}$ are (at least) first-order, componentwise approximations of the x and y -derivatives of U' at $z_{j,k}$.

In order to calculate the i -th component of the numerical derivatives of U' , $(U'_x)_{j,k}^{(i)}$ and $(U'_y)_{j,k}^{(i)}$, we construct four linear interpolations: $L_{j,k}^{(i)\pm,\pm}(x, y)$. Each of these linear interpolations is obtained by the point $(z_{j,k}, \overline{U'}_{j,k}^{(i)})$ and adjacent points in the two neighboring cells. For example, the plane $L_{j,k}^{(i)+,+}(x, y)$ is uniquely determined by $(z_{j,k}, \overline{U'}_{j,k}^{(i)})$, $(z_{j+1,k}, \overline{U'}_{j+1,k}^{(i)})$ and $(z_{j,k+1}, \overline{U'}_{j,k+1}^{(i)})$ and the plane $L_{j,k}^{(i)+,-}(x, y)$ is uniquely determined by $(z_{j,k}, \overline{U'}_{j,k}^{(i)})$, $(z_{j+1,k}, \overline{U'}_{j+1,k}^{(i)})$, meanwhile, $(z_{j,k-1}, \overline{U'}_{j,k-1}^{(i)})$.

To minimize numerical dispersion, one can use any flux limiter. In our numerical experiments

reported below, we have used the generalized minmod limiter for each component:

$$\begin{aligned}
(U'_x)_{j,k}^{(i)} &= \minmod\left(\frac{1}{4}\left[(L_{j,k}^{(i)+,+})_x + (L_{j,k}^{(i)-,+})_x + (L_{j,k}^{(i)-,-})_x + (L_{j,k}^{(i)+,-})_x\right], \right. \\
&\quad \left. \theta(L_{j,k}^{(i)+,+})_x, \theta(L_{j,k}^{(i)-,+})_x, \theta(L_{j,k}^{(i)-,-})_x, \theta(L_{j,k}^{(i)+,-})_x\right); \\
(U'_y)_{j,k}^{(i)} &= \minmod\left(\frac{1}{4}\left[(L_{j,k}^{(i)+,+})_y + (L_{j,k}^{(i)-,+})_y + (L_{j,k}^{(i)-,-})_y + (L_{j,k}^{(i)+,-})_y\right], \right. \\
&\quad \left. \theta(L_{j,k}^{(i)+,+})_y, \theta(L_{j,k}^{(i)-,+})_y, \theta(L_{j,k}^{(i)-,-})_y, \theta(L_{j,k}^{(i)+,-})_y\right).
\end{aligned} \tag{3.2.6}$$

Here the parameter $\theta \in [1, 2]$ controls the amount of numerical dissipation: larger values of θ typically result in less dissipative but more dispersive schemes. Meanwhile, the minmod function is defined by:

$$\minmod(z_1, z_2, \dots) := \begin{cases} \min(z_1, z_2, \dots), & \text{if } z_i > 0 \ \forall i, \\ \max(z_1, z_2, \dots), & \text{if } z_i < 0 \ \forall i, \\ 0, & \text{otherwise,} \end{cases}$$

Here, we do all numerical reconstruction on perturbation variables U' , so no positivity preserving scheme is applied here.

3.2.1.3 Evolution

(3.2.3) can be further reduced as

$$U_t + F(U)_x + G(U)_y = S(U), \tag{3.2.7}$$

since we regard U_s as underlying information and U' can be uniquely determined by U and U_s .

The second-order semi-discrete central-upwind scheme on quadrilateral grids are developed in [Shi16] and here we reduce the numerical dissipation by using the approach presented in [Kur07a]:

$$\frac{d}{dt} \bar{U}_{j,k} = -\frac{1}{|C_{j,k}|} \left[H_{j+\frac{1}{2},k} - H_{j-\frac{1}{2},k} + H_{j,k+\frac{1}{2}} - H_{j,k-\frac{1}{2}} \right] + \bar{S}_{j,k}, \tag{3.2.8}$$

where $H_{j\pm\frac{1}{2},k}$ and $H_{j,k\pm\frac{1}{2}}$ are 4 numerical fluxes crossing 4 cell interfaces/edges. Here we can represent the numerical flux $H_{j+\frac{1}{2},k}$ across cell interface $z_{j+\frac{1}{2},k-\frac{1}{2}}, z_{j+\frac{1}{2},k+\frac{1}{2}}$:

$$\begin{aligned}
H_{j+\frac{1}{2},k} &= \ell_{j+\frac{1}{2},k} \left[\left(\cos(\theta_{j+\frac{1}{2},k}) H_{j+\frac{1}{2},k}^x + \sin(\theta_{j+\frac{1}{2},k}) H_{j+\frac{1}{2},k}^y \right) \right. \\
&\quad \left. + \frac{a_{j+\frac{1}{2},k}^+ a_{j+\frac{1}{2},k}^-}{a_{j+\frac{1}{2},k}^+ - a_{j+\frac{1}{2},k}^-} \left(U_{j+\frac{1}{2},k}^+ - U_{j+\frac{1}{2},k}^- - d_{j+\frac{1}{2},k} \right) \right],
\end{aligned} \tag{3.2.9}$$

where the x - and y -directional fluxes $\mathbf{H}_{j+\frac{1}{2},k}^x$ and $\mathbf{H}_{j+\frac{1}{2},k}^y$ are

$$\begin{aligned}\mathbf{H}_{j+\frac{1}{2},k}^x &= \frac{a_{j+\frac{1}{2},k}^+ \mathbf{F}(U_{j+\frac{1}{2},k}^-) - a_{j+\frac{1}{2},k}^- \mathbf{F}(U_{j+\frac{1}{2},k}^+)}{a_{j+\frac{1}{2},k}^+ - a_{j+\frac{1}{2},k}^-} \\ \mathbf{H}_{j+\frac{1}{2},k}^y &= \frac{a_{j+\frac{1}{2},k}^+ \mathbf{G}(U_{j+\frac{1}{2},k}^-) - a_{j+\frac{1}{2},k}^- \mathbf{G}(U_{j+\frac{1}{2},k}^+)}{a_{j+\frac{1}{2},k}^+ - a_{j+\frac{1}{2},k}^-},\end{aligned}\tag{3.2.10}$$

with built-in anti-diffusion term $\mathbf{d}_{j+\frac{1}{2},k}$:

$$\begin{aligned}\mathbf{d}_{j+\frac{1}{2},k} &= \min\left(\mathbf{U}_{j+\frac{1}{2},k+\frac{1}{2}}^+ - \mathbf{U}_{j+\frac{1}{2},k}^{\text{int}}, \mathbf{U}_{j+\frac{1}{2},k-\frac{1}{2}}^+ - \mathbf{U}_{j+\frac{1}{2},k}^{\text{int}}, \right. \\ &\quad \left. \mathbf{U}_{j+\frac{1}{2},k}^{\text{int}} - \mathbf{U}_{j+\frac{1}{2},k+\frac{1}{2}}^-, \mathbf{U}_{j+\frac{1}{2},k}^{\text{int}} - \mathbf{U}_{j+\frac{1}{2},k-\frac{1}{2}}^- \right)\end{aligned}\tag{3.2.11}$$

and the intermediate value $U_{j+\frac{1}{2},k}^{\text{int}}$:

$$\begin{aligned}U_{j+\frac{1}{2},k}^{\text{int}} &= \frac{a_{j+\frac{1}{2},k}^+ U_{j+\frac{1}{2},k}^+ - a_{j+\frac{1}{2},k}^- U_{j+\frac{1}{2},k}^-}{a_{j+\frac{1}{2},k}^+ - a_{j+\frac{1}{2},k}^-} \\ &\quad - \cos(\theta_{j+\frac{1}{2},k}) \frac{\mathbf{F}(U_{j+\frac{1}{2},k}^+) - \mathbf{F}(U_{j+\frac{1}{2},k}^-)}{a_{j+\frac{1}{2},k}^+ - a_{j+\frac{1}{2},k}^-} - \sin(\theta_{j+\frac{1}{2},k}) \frac{\mathbf{G}(U_{j+\frac{1}{2},k}^+) - \mathbf{G}(U_{j+\frac{1}{2},k}^-)}{a_{j+\frac{1}{2},k}^+ - a_{j+\frac{1}{2},k}^-}.\end{aligned}\tag{3.2.12}$$

$U_{j+\frac{1}{2},k}^\pm$ are conservative variables at the same point $z_{j+\frac{1}{2},k}$ that can be determined by $U_s(z_{j+\frac{1}{2},k})$ and $(U')_{j+\frac{1}{2},k}^\pm$.

Similarly, $U_{j+\frac{1}{2},k\pm\frac{1}{2}}^+$ and $U_{j+\frac{1}{2},k\pm\frac{1}{2}}^-$ are conservative variables at vertices of the edge $z_{j+\frac{1}{2},k-\frac{1}{2}} z_{j+\frac{1}{2},k+\frac{1}{2}}$ that can also be determined by corresponding U_s and U' .

Noted that $(U')_{j+\frac{1}{2},k}^\pm$ are perturbation variables at the same point values $z_{j+\frac{1}{2},k}$ of the linear pieces reconstruction (3.2.5) but from different cells $C_{j,k}$ and $C_{j+1,k}$, namely,

$$(U')_{j+\frac{1}{2},k}^- := \mathbf{P}_{j,k}(z_{j+\frac{1}{2},k}), \quad (U')_{j+\frac{1}{2},k}^+ := \mathbf{P}_{j+1,k}(z_{j+\frac{1}{2},k}),$$

and $a_{j+\frac{1}{2},k}^\pm$ and $a_{j,k+\frac{1}{2}}^\pm$ are the directional local speeds of propagation, which, in the case of convex flux function, can be estimated by

$$\begin{aligned}a_{j+\frac{1}{2},k}^+ &= \max\{\lambda_N(V_{j+\frac{1}{2},k}^+), \lambda_N(V_{j+\frac{1}{2},k}^-), 0\}, & a_{j+\frac{1}{2},k}^- &= \min\{\lambda_1(V_{j+\frac{1}{2},k}^+), \lambda_1(V_{j+\frac{1}{2},k}^-), 0\}, \\ a_{j,k+\frac{1}{2}}^+ &= \max\{\lambda_N(V_{j,k+\frac{1}{2}}^+), \lambda_N(V_{j,k+\frac{1}{2}}^-), 0\}, & a_{j,k+\frac{1}{2}}^- &= \min\{\lambda_1(V_{j,k+\frac{1}{2}}^+), \lambda_1(V_{j,k+\frac{1}{2}}^-), 0\},\end{aligned}\tag{3.2.13}$$

with $\lambda_1(V) \leq \lambda_2(V) \leq \dots \leq \lambda_N(V)$ being the N eigenvalues of the matrix $V = \cos(\theta) \frac{\partial \mathbf{F}}{\partial U} + \sin(\theta) \frac{\partial \mathbf{G}}{\partial U}$

and

$$\begin{aligned} V_{j+\frac{1}{2},k}^{\pm} &:= \cos(\theta_{j+\frac{1}{2},k}) \frac{\partial \mathbf{F}}{\partial \mathbf{U}}(\mathbf{U}_{j+\frac{1}{2},k}^{\pm}) + \sin(\theta_{j+\frac{1}{2},k}) \frac{\partial \mathbf{G}}{\partial \mathbf{U}}(\mathbf{U}_{j+\frac{1}{2},k}^{\pm}), \\ V_{j,k+\frac{1}{2}}^{\pm} &:= \cos(\theta_{j,k+\frac{1}{2}}) \frac{\partial \mathbf{F}}{\partial \mathbf{U}}(\mathbf{U}_{j,k+\frac{1}{2}}^{\pm}) + \sin(\theta_{j,k+\frac{1}{2}}) \frac{\partial \mathbf{G}}{\partial \mathbf{U}}(\mathbf{U}_{j,k+\frac{1}{2}}^{\pm}). \end{aligned} \quad (3.2.14)$$

The numerical fluxes $\mathbf{H}_{j-\frac{1}{2},k}$ and $\mathbf{H}_{j,k\pm\frac{1}{2}}$ can be computed in a similar way like $\mathbf{H}_{j+\frac{1}{2},k}$ using eqs. (3.2.9) to (3.2.14).

Finally, the term $\bar{\mathbf{S}}_{j,k}$ in (3.2.8) represents appropriate discretizations of the cell averages of the source terms:

$$\bar{\mathbf{S}}_{j,k} \approx \frac{1}{|C_{j,k}|} \iint_{C_{j,k}} \mathbf{S}(\mathbf{U}(x, y, t)) dx dy. \quad (3.2.15)$$

Remark 3.2.2 Notice that if both $a_{j+\frac{1}{2},k}^{\pm}$ are very close to zero, that is, if $a_{j+\frac{1}{2},k}^{+} - a_{j+\frac{1}{2},k}^{-} < \varepsilon$, where $\varepsilon > 0$ is a small parameter, we replace the numerical fluxes $\mathbf{H}_{j+\frac{1}{2},k}$ in (3.2.9) with

$$\mathbf{H}_{j+\frac{1}{2},k} = \frac{\ell_{j+\frac{1}{2},k}}{2} \left(\cos(\theta_{j+\frac{1}{2},k}) \left[\mathbf{F}(\mathbf{U}_{j+\frac{1}{2},k}^{-}) + \mathbf{F}(\mathbf{U}_{j+\frac{1}{2},k}^{+}) \right] + \sin(\theta_{j+\frac{1}{2},k}) \left[\mathbf{G}(\mathbf{U}_{j+\frac{1}{2},k}^{-}) + \mathbf{G}(\mathbf{U}_{j+\frac{1}{2},k}^{+}) \right] \right).$$

Similarly, if both $a_{j,k+\frac{1}{2}}^{\pm}$ are very close to zero, we replace the numerical fluxes $\mathbf{H}_{j,k+\frac{1}{2}}$ in (3.2.9) with

$$\mathbf{H}_{j,k+\frac{1}{2}} = \frac{\ell_{j,k+\frac{1}{2}}}{2} \left(\cos(\theta_{j,k+\frac{1}{2}}) \left[\mathbf{F}(\mathbf{U}_{j,k+\frac{1}{2}}^{-}) + \mathbf{F}(\mathbf{U}_{j,k+\frac{1}{2}}^{+}) \right] + \sin(\theta_{j,k+\frac{1}{2}}) \left[\mathbf{G}(\mathbf{U}_{j,k+\frac{1}{2}}^{-}) + \mathbf{G}(\mathbf{U}_{j,k+\frac{1}{2}}^{+}) \right] \right).$$

In all of our numerical experiments, we have used $\varepsilon = 10^{-8}$.

Remark 3.2.3 The ODE systems (3.2.8)–(3.2.15) should be numerically solved by a stable ODE solver of a proper order. In all of the numerical examples in this chapter, we have used the three-stage third-order strong stability preserving (SSP) Runge-Kutta method; see, e.g., [Got01; Got11]. The time step is restricted by the CFL condition, which is

$$\Delta t \max_{j,k} \left\{ \frac{\max\{|a_{j+\frac{1}{2},k}^{-}|, |a_{j-\frac{1}{2},k}^{+}|, |a_{j,k+\frac{1}{2}}^{-}|, |a_{j,k-\frac{1}{2}}^{+}|\}}{\text{dist}(z_{j,k}, \partial C_{j,k})} \right\} \leq \frac{1}{2}. \quad (3.2.16)$$

3.3 Numerical Examples

In this section, we demonstrate the performance of the proposed well-balanced central-upwind scheme on three numerical examples. In all of the experiments, we take the minmod parameter $\theta = 1.3$; see [Kur20].

3.3.1 Example 1 (Convergence Test)

In the first example, we experimentally check the accuracy of the proposed method. We take $g = 1$.

3.3.1.1 Problem Settings

We take a relatively simple computational domain $\{(x, y) : -1 \leq x \leq 1, 0.1(x+1) \leq y \leq 2\}$; see Figure 3.3.1 (left).

The steady-state solution satisfying (3.1.3) and (3.1.2) is made of one layer atmosphere and given by

$$\theta_s(y) = e^{y/4}, \quad p_s(y) = \left(1 + \frac{8}{7}(e^{-y/4} - 1)\right)^{7/2}, \quad \rho_s(y) = \frac{[p_s(y)]^{5/7}}{\theta_s(y)}.$$

We introduce a small perturbation in the potential temperature only,

$$\theta'(x, y, 0) = 0.01 e^{-100(x^2 + (y-0.5)^2)},$$

while setting

$$u'(x, y, 0) = v'(x, y, 0) \equiv 0, \quad \rho'(x, y, 0) \equiv 0, \quad p'(x, y, 0) \equiv 0.$$

In addition, solid wall boundary conditions are applied on all of the four sides of the computational domain.

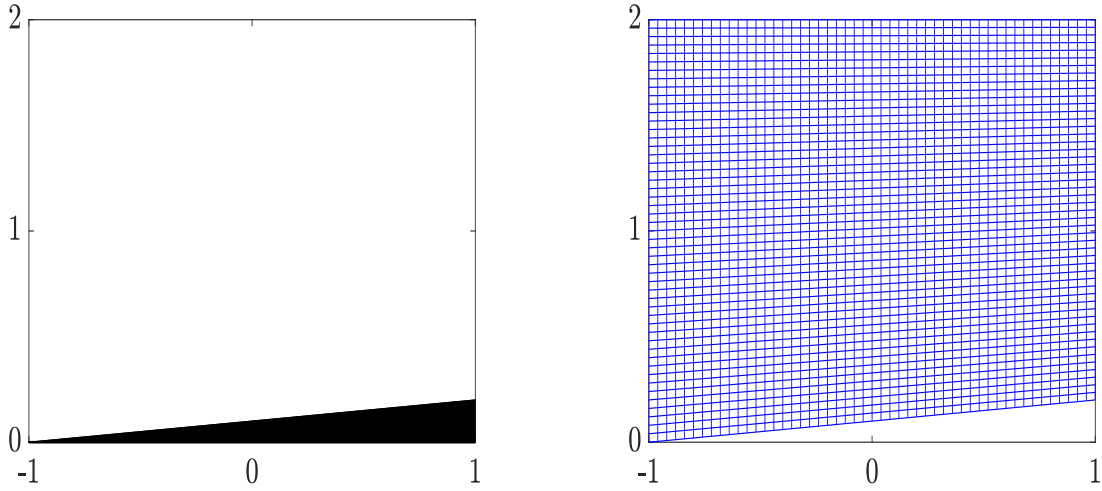


Figure 3.3.1 Example 1: Computational domain (left) and structured quadrilateral mesh (right).

3.3.1.2 Mesh Generation

Structured quadrilateral mesh can be easily generated in this example by equally spacing left and right boundaries for the horizontal distance and top and bottom boundaries for vertical distances;

see Figure 3.3.1 (right). Then, the constructed cell vertices are

$$\begin{cases} x_{j+\frac{1}{2},k+\frac{1}{2}} = -1 + \frac{2j}{M}, \\ y_{j+\frac{1}{2},k+\frac{1}{2}} = \left(1 - \frac{k}{N}\right) 0.1(x_{j+\frac{1}{2},\frac{1}{2}} + 1) + \frac{2k}{N}, \end{cases} \quad j = 0, \dots, M, \quad k = 0, \dots, N.$$

3.3.1.3 Results

We measure the experimental convergence rates using the numerical solutions computed with $M = N$ for $N = 50, 100, 200, 400$ and 800 at time $t = 0.1$. The convergence rates are calculated using the numerical solutions on successively refined grids. For example, let us denote by ρ_N the density computed using the $N \times N$ mesh. Then the estimated convergence rate for the density field is

$$\text{Rate} \approx \log_2 \left(\frac{\|\Delta \rho_{N/2}\|_1}{\|\Delta \rho_N\|_1} \right), \quad \Delta \rho_N := \|\rho_N - \rho_{N/2}\|_1.$$

The corresponding convergence rates for the other fields can be obtained similarly.

The results of the mesh refinement study are reported in Table 3.3.1. As one can see, the proposed method achieves the expected second order of accuracy.

Table 3.3.1 Example 1: Experimental convergence rates in the L^1 -norm.

N	$\Delta \rho_N$	Rate	$\Delta(\rho u)_N$	Rate	$\Delta(\rho v)_N$	Rate	$\Delta(\rho \theta)_N$	Rate
100	0.9288E-4	–	0.9354E-5	–	0.1236E-4	–	0.5476E-4	–
200	0.2506E-4	1.89	0.3488E-5	1.42	0.0381E-4	1.70	0.1479E-4	1.89
400	0.0639E-4	1.97	0.0875E-5	2.00	0.0092E-4	2.05	0.0354E-4	2.06
800	0.0162E-4	1.98	0.0210E-5	2.06	0.0024E-4	1.96	0.0089E-4	1.99

3.3.2 Example 2 (Zeppelin Test)

In this test, we consider an example from [Dur86; Kle09], in which the hot air is propagating upward and flows around a stationary suspended zeppelin. We take $g = 1.14$.

3.3.2.1 Problem Settings

We solve the studied atmospheric flow equations in a vertically stratified atmosphere with a stationary elliptic obstacle suspended in the air. The computational domain is presented in Figure 3.3.2.

The boundary of the obstacle is given by

$$\frac{x^2}{\ell_0^2} + \frac{(y-0.5)^2}{h_0^2} = \frac{1}{4},$$

where $h_0 = 0.333$ is the height and $\ell_0 = 0.466$ is the length of the zeppelin.

In order to minimize gravity wave reflection from the top of the domain, we use the highlighted upper part of the computational domain as a sponge layer; see Figure 3.3.2. To this end, we replace the computed solution at every stage of the SSP-RK3 method with the following relaxed values:

$$\bar{U}_{j,k}^{\text{relax}} = \bar{U}_{j,k}^0 + \frac{1}{1 + \frac{\Delta t}{10} \hat{y}} (\bar{U}_{j,k} - \bar{U}_{j,k}^0),$$

where $\bar{U}_{j,k}^0$ are the initial data and $\hat{y} := \max(y_{j,k} - 1, 0)$ is the distance from the center of mass $(x_{j,k}, y_{j,k})$ of cell $C_{j,k}$ to the non-sponge part of the computational domain.

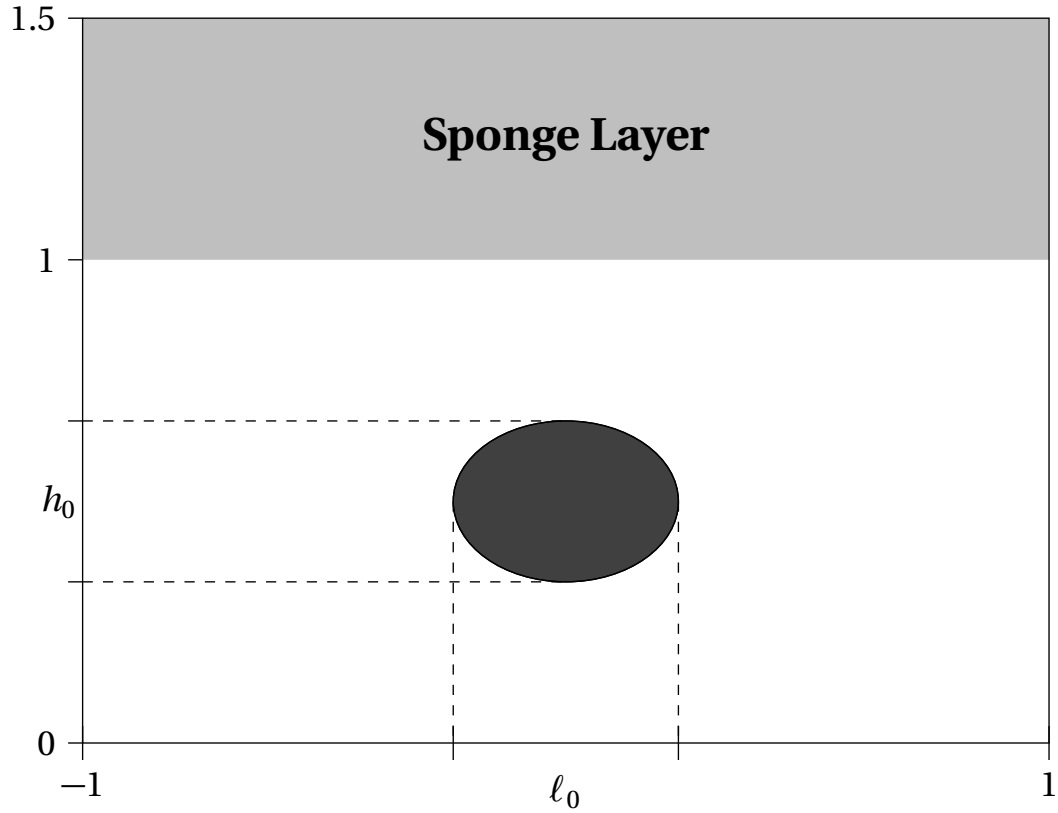


Figure 3.3.2 Example 2: Computational domain.

In this example, the steady-state solution satisfying (3.1.3) and (3.1.2) is

$$\theta_s(y) \equiv 1, \quad p_s(y) = \left(1 - \frac{2}{7} g y\right)^{7/2}, \quad \rho_s(y) = \left(1 - \frac{2}{7} g y\right)^{5/2}.$$

We introduce the initial perturbations in the potential temperature and pressure so that

$$\theta'(x, y, 0) = \theta_B \cos^2\left(\frac{\pi r}{2}\right), \quad p'(x, y, 0) = p_s(y) \left(\left[1 + \theta_B \cos^2\left(\frac{\pi r}{2}\right)\right]^{7/5} - 1 \right), \quad (3.3.1)$$

while setting

$$u'(x, y, 0) = v'(x, y, 0) \equiv 0, \quad \rho'(x, y, 0) \equiv 0.$$

In (3.3.1), $r = \min\left\{\frac{1}{R_B} \sqrt{(x - x_B)^2 + (y - y_B)^2}, 1\right\}$, with $R_B = 0.15$, $(x_B, y_B) = (-0.23, 0.2)$ and $\theta_B = 0.0333$ being the radius, center and magnitude of the initial perturbation.

In addition, solid wall conditions are applied on the boundary of the zeppelin and on the top and the bottom of the computational domain, while periodic boundary conditions are implemented on the horizontal domain edges.

3.3.2.2 Mesh Generation

The structured quadrilateral mesh we have used in this example is presented in Figure 3.3.3.

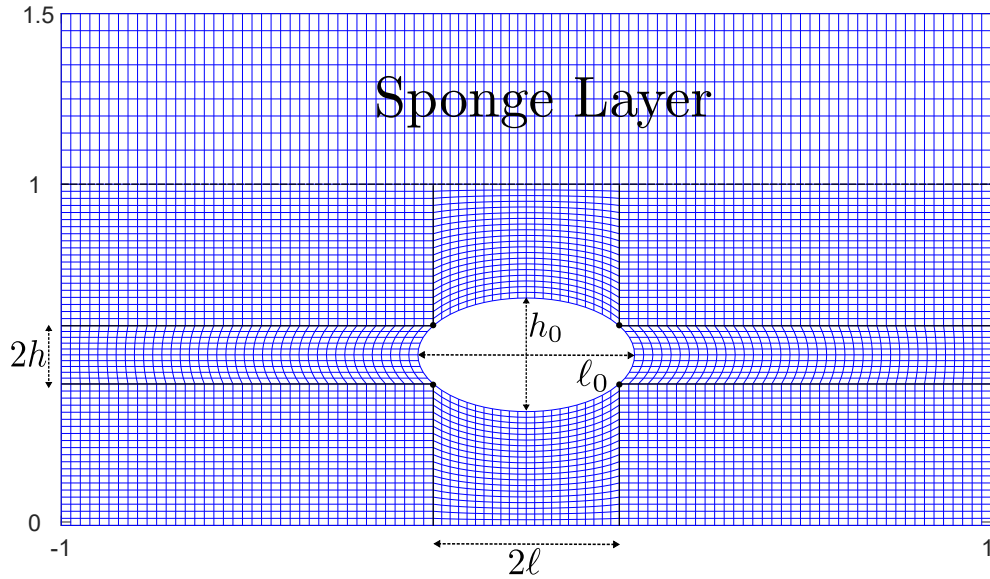


Figure 3.3.3 Example 2: Structured quadrilateral mesh.

This mesh is constructed as follows. We first consider the mesh in the non-sponge part of the

computational domain in $[-1, 1] \times [0, 1]$ and introduce the cell vertices there:

$$\left\{ \left(x_{j+\frac{1}{2}, k+\frac{1}{2}}, y_{j+\frac{1}{2}, k+\frac{1}{2}} \right) \right\}, \quad j = -M, \dots, M, \quad k = -N, \dots, N.$$

Our goal is to make the generated mesh structured and avoid flat angles in the mesh cells. The difficulty is related to the presence of the elliptic obstacle inside the domain, which we split into several simpler parts using the following four symmetric points on the boundary of the ellipse:

$$\left(x_{\pm M'+\frac{1}{2}, \pm N'+\frac{1}{2}}, y_{\pm M'+\frac{1}{2}, \pm N'+\frac{1}{2}} \right) = (\pm \ell, \pm h + 0.5),$$

where $\ell < \ell_0/2$ and $h = h_0 \sqrt{\frac{1}{4} - \frac{\ell^2}{\ell_0^2}}$; see Figure 3.3.3. We then consider the cell vertices located below and above the zeppelin, that is, those vertices whose indices satisfy $|j| \leq M'$ and $|k| \geq N'$; see Figure 3.3.3. These cell vertices are given by

$$x_{j+\frac{1}{2}, k+\frac{1}{2}} = \frac{j\ell}{M'}, \quad j = -M', \dots, M',$$

$$y_{j+\frac{1}{2}, k+\frac{1}{2}} = \begin{cases} \frac{N+k}{N-N'} \left(\frac{1}{2} - h_0 \sqrt{\frac{1}{4} - \frac{x_{j+\frac{1}{2}, k+\frac{1}{2}}^2}{\ell_0^2}} \right), & k = -N, \dots, -N', \\ 1 - \frac{N-k}{N-N'} \left(\frac{1}{2} - h_0 \sqrt{\frac{1}{4} - \frac{x_{j+\frac{1}{2}, k+\frac{1}{2}}^2}{\ell_0^2}} \right), & k = N', \dots, N. \end{cases}$$

Similarly, the cell vertices located to the left and to the right of the zeppelin, that is, those vertices whose indices satisfy $|j| \geq M'$ and $|k| \leq N'$, are given by

$$y_{j+\frac{1}{2}, k+\frac{1}{2}} = \frac{kh}{N'}, \quad k = -N', \dots, N',$$

$$x_{j+\frac{1}{2}, k+\frac{1}{2}} = \begin{cases} \frac{j+M'}{M-M'} - \frac{M+j}{M-M'} \cdot \ell_0 \sqrt{\frac{1}{4} - \frac{y_{j+\frac{1}{2}, k+\frac{1}{2}}^2}{h_0^2}}, & j = -M, \dots, -M', \\ \frac{j-M'}{M-M'} + \frac{M-j}{M-M'} \cdot \ell_0 \sqrt{\frac{1}{4} - \frac{y_{j+\frac{1}{2}, k+\frac{1}{2}}^2}{h_0^2}}, & j = M', \dots, M; \end{cases}$$

see Figure 3.3.3. Next, the cell vertices in the four corners of the non-sponge part of the computational

domain, that is, those whose indices satisfy $|j| > M'$ and $|k| > N'$, are

$$x_{j+\frac{1}{2}, k+\frac{1}{2}} = \begin{cases} \frac{j+M'}{M-M'} - \ell \frac{M+j}{M-M'}, & j = -M, \dots, -M'-1, \\ \frac{j-M'}{M-M'} + \ell \frac{M-j}{M-M'}, & j = M'+1, \dots, M, \end{cases}$$

$$y_{j+\frac{1}{2}, k+\frac{1}{2}} = \begin{cases} \frac{N+k}{N-N'} \left(\frac{1}{2} - h \right), & k = -N, \dots, -N'-1, \\ 1 - \frac{N-k}{N-N'} \left(\frac{1}{2} - h \right), & k = N'+1, \dots, N, \end{cases}$$

Finally, in the sponge layer $[-1, 1] \times [1, 1.5]$ we use a uniform mesh with

$$x_{j+\frac{1}{2}, k+\frac{1}{2}} = x_{j+\frac{1}{2}, N+\frac{1}{2}}, \quad j = -M, \dots, M,$$

$$y_{j+\frac{1}{2}, k+\frac{1}{2}} = 1 + \frac{k-N}{2N_s}, \quad k = N+1, \dots, N+N_s.$$

In the numerical simulations reported in 3.3.2.3, we have used $\ell = 0.2$. Notice that if ℓ is chosen to be close to either 0 or $\ell_0/2$, flat angles will appear in some of the cells, and this may cause numerical oscillations.

3.3.2.3 Results

We first compute the solution using the constructed mesh with $M = 400$, $N = 200$, $N_s = 50$, $M' = 81$ and $N' = 35$ until the final time $t = 33.55$ and plot the time snapshots of the obtained potential temperature θ in Figure 3.3.4. At $t = 0$, the warm air circular area is located below the left part of the zeppelin. As a result of buoyancy effects, warm air rises and by the time $t = 5.77$ the warm air “bubble” touches the lower boundary of the zeppelin and then splits into two parts, which move along the surface of the zeppelin in the opposite directions. Later on, the left part of the “bubble” takes off the surface of the zeppelin, keeps rising and further splits into smaller pieces, while the right-going part of the “bubble” keeps sliding along the zeppelin. By the final time $t = 33.55$, the left part of the warm air spins counter-clockwise, the middle part spins clockwise and reaches the absorption layer, and the right part has detached from the zeppelin and started to rise and spin clockwise.

It should be observed that while the details of the warm air evolution are not the same as in the computations reported in [Kle09], we find that the results are qualitatively similar. In order to further validate the proposed numerical method, we refine the mesh and compute the solution at the same sequence of times, but using $M = 800$, $N = 400$, $N_s = 100$, $M' = 161$ and $N' = 69$. The obtained results, plotted in Figure 3.3.5, clearly demonstrate that the structure of the fine mesh solution is the same as the coarse mesh one, while, as expected, more small features are now resolved.

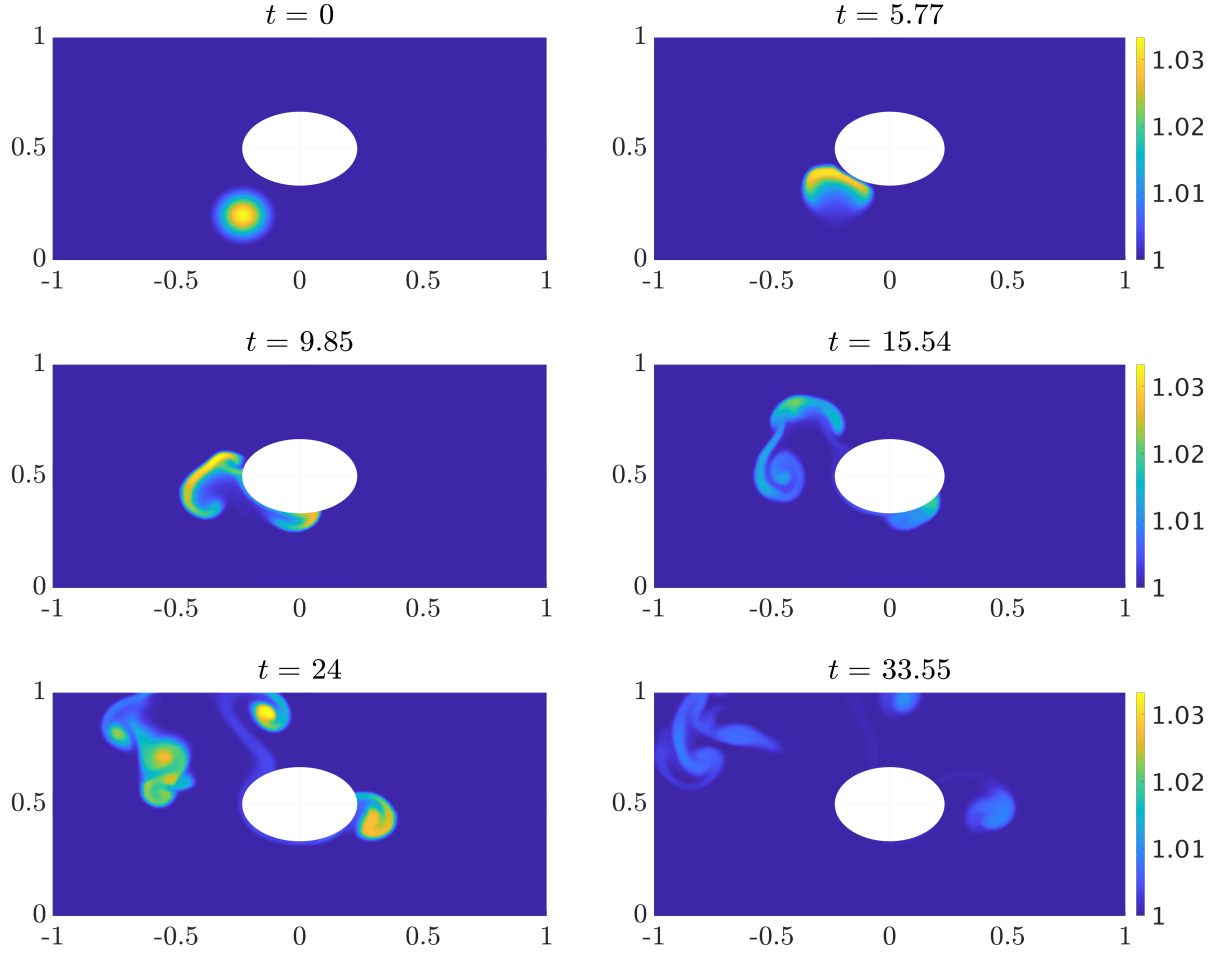


Figure 3.3.4 Example 2: Potential temperature θ at different times.

3.3.3 Example 3 (Lee Waves)

In the final example taken from [Dur86; GB06; Kle09], we test the capability of the proposed numerical method to accurately capture the Lee waves generated when gravitationally stratified flow passes a mountain. We take $g = 1.14$.

3.3.3.1 Problem Settings

The computational domain is

$$\{(x, y) : -7.2 \leq x \leq 10.8, h(x) \leq y \leq 1.28\}, \quad h(x) = \frac{h_0 a^2}{x^2 + a^2}, \quad (3.3.2)$$

where $a = 1$ and $h_0 = 0.06$ represent the characteristic width and the height of the mountain. We set the solid wall boundary conditions on the top and the bottom of the computational domain, while the periodicity is imposed on the left and the right boundaries.

A sponge layer is implemented to avoid gravity wave reflection from top of the domain and

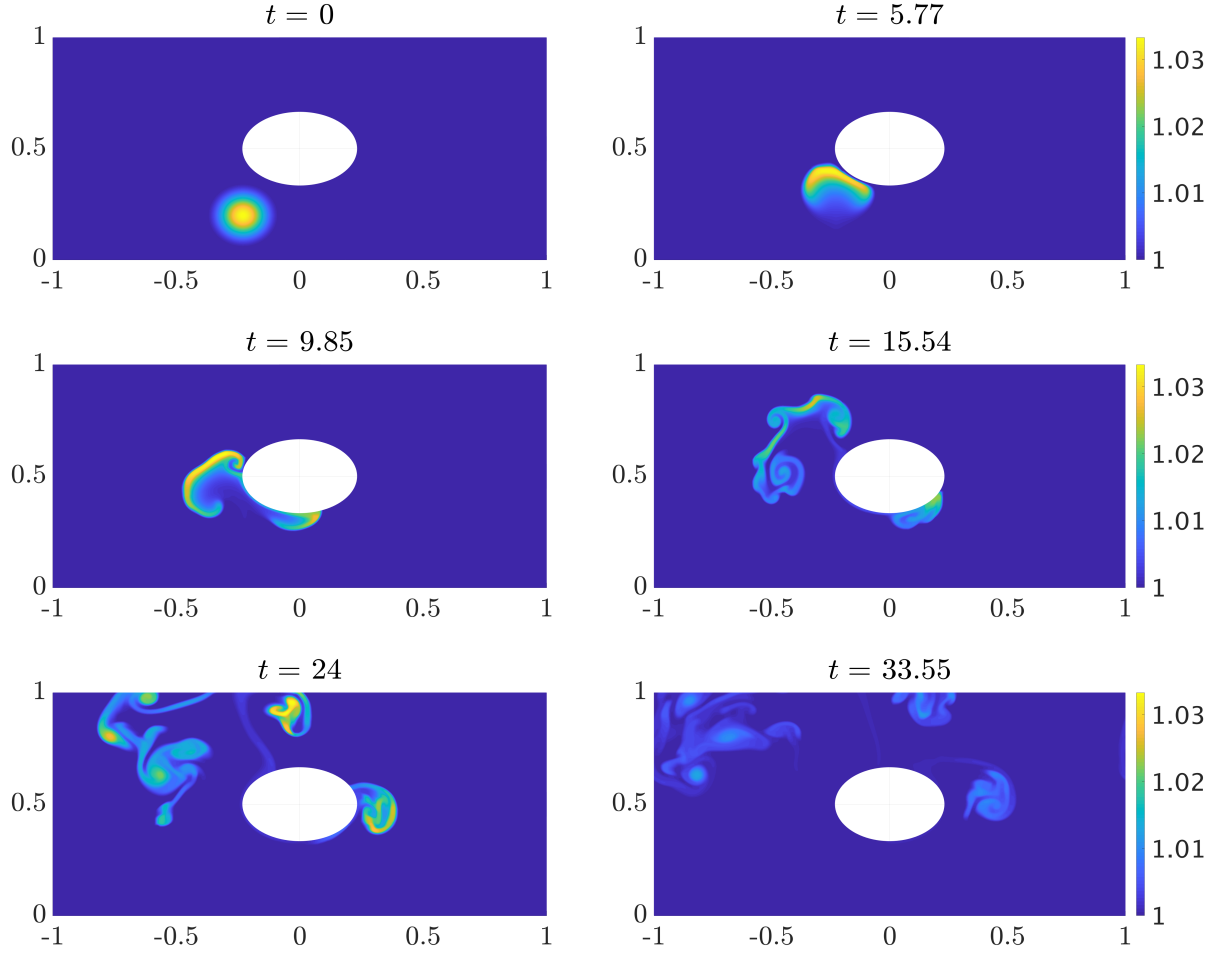


Figure 3.3.5 Same as Figure 3.3.4, but the results are computed using a finer mesh.

transmission across the horizontal boundaries. As illustrated in Figure 3.3.6, the sponge width is 3 both on the left and on the right and its height is 0.63. In the sponge layer, we follow [Kle09] and replace the computed solution at every stage of the SSP-RK3 method with the following relaxed values:

$$\bar{U}_{j,k}^{\text{relax}} = \bar{U}_{j,k}^0 + \frac{1}{1 + \Delta t \max(0.83\hat{x}, 0.17\hat{y})} (\bar{U}_{j,k} - \bar{U}_{j,k}^0),$$

where $\bar{U}_{j,k}^0$ are the initial data and \hat{x} and \hat{y} are the horizontal and vertical relative distances from the center of mass $(x_{j,k}, y_{j,k})$ of cell $C_{j,k}$ to the non-sponge part of the computational domain, namely, $\hat{x} := \max(x_{j,k} - 7.8, -4.2 - x_{j,k}, 0)$ and $\hat{y} := \max(y_{j,k} - 0.65, 0)$.

In this example, the steady-state solution satisfying (1.3) and (1.2) consists of two layers of atmosphere (with two different Brunt-Väisälä frequency constants N_ℓ and N_u for the lower and

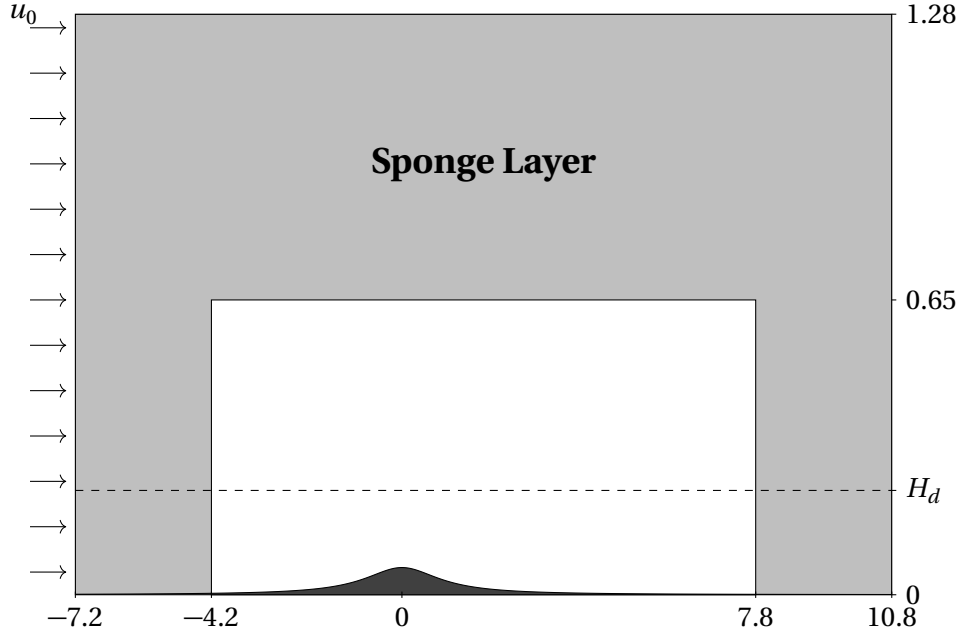


Figure 3.3.6 Example 3: Computational domain.

upper layers, respectively) separated at height H_d :

$$\begin{aligned}\theta_s(y) &= \begin{cases} e^{N_\ell^2 y/g}, & y < H_d, \\ e^{[(N_\ell^2 - N_u^2)H_d + N_u^2 y]/g}, & y \geq H_d, \end{cases} \\ p_s(y) &= \begin{cases} \left[1 - \frac{2g^2}{7N_\ell^2}(1 - e^{-N_\ell^2 y/g})\right]^{7/2}, & y < H_d, \\ \left[p_{H_d}^{2/7} - \frac{2g^2}{7N_u^2}e^{-N_\ell^2 H_d/g}(1 - e^{-N_u^2(y-H_d)/g})\right]^{7/2}, & y \geq H_d, \end{cases} \\ \rho_s(y) &= \frac{[p_s(y)]^{5/7}}{\theta_s(y)},\end{aligned}$$

where $p_{H_d} = \lim_{y \rightarrow H_d^-} p_s(y) = \left[1 - \frac{2g^2}{7N_\ell^2}(1 - e^{-N_\ell^2 H_d/g})\right]^{7/2}$. Similarly to [Kle09; GB06], we will consider three different combinations of parameters H_d , N_ℓ and N_u , given in Table 3.3.2.

Table 3.3.2 Lee-wave parameters.

Parameter	Case (a)	Case (b)	Case (c)
H_d	0.1571	0.3142	0.3142
N_ℓ	0.6816	0.6816	0.3408
N_u	0.3408	0.3408	0.6816

We introduce the constant initial perturbation $u'(x, y, 0) = 0.06816$ in the horizontal velocity, while setting $v'(x, y, 0)$, $\rho'(x, y, 0)$ and $\theta'(x, y, 0)$ to be zero.

3.3.3.2 Mesh Generation

The structured quadrilateral mesh we have used in this example is presented in Figure 3.3.7.

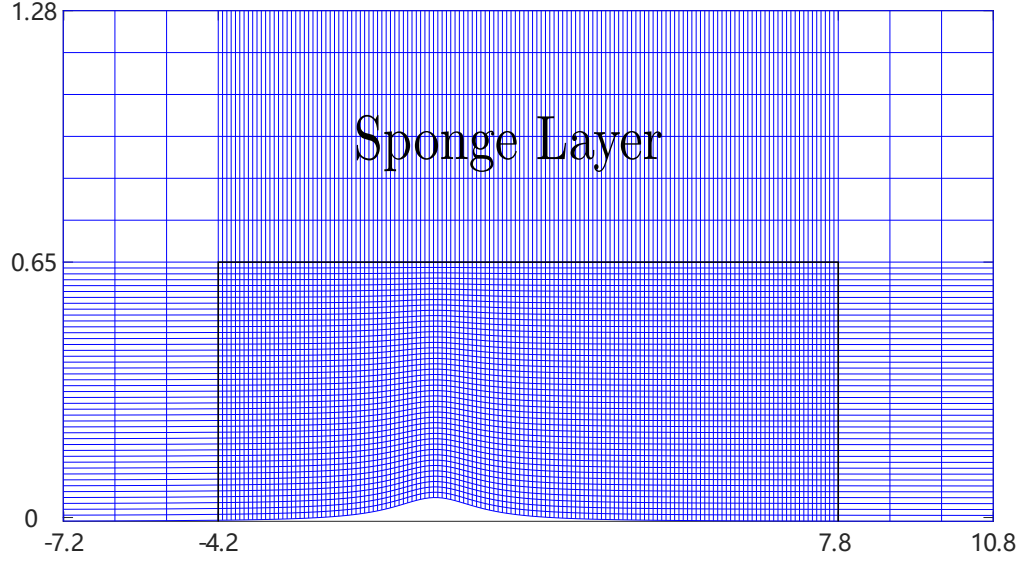


Figure 3.3.7 Example 3: Structured quadrilateral mesh.

This mesh is constructed as follows. We begin with the non-sponge part of the computational domain, which is

$$[x_{\min}, x_{\max}] \times [h(x), y_{\max}], \quad x_{\min} := -4.2, \quad x_{\max} := 7.8, \quad y_{\max} := 0.65,$$

where $h(x)$ is defined in (3.3.2). The cell vertices in this part of the domain are given by

$$\begin{aligned} x_{j+\frac{1}{2}, k+\frac{1}{2}} &= \left(1 - \frac{j}{M}\right) x_{\min} + \frac{j}{M} x_{\max}, \quad j = 0, \dots, M, \\ y_{j+\frac{1}{2}, k+\frac{1}{2}} &= \left(1 - \frac{k}{N}\right) h(x_{j+\frac{1}{2}, k+\frac{1}{2}}) + \frac{k}{N} y_{\max}, \quad k = 0, \dots, N. \end{aligned}$$

Within the sponge layer, we have

$$x_{j+\frac{1}{2},k+\frac{1}{2}} = \begin{cases} x_{\min} + \frac{j}{M_s} L_s, & j = -M_s, \dots, -1, \\ x_{\max} + \frac{j-M}{M_s} L_s, & j = M+1, \dots, M+M_s, \end{cases}$$

$$y_{j+\frac{1}{2},k+\frac{1}{2}} = \begin{cases} y_{j+\frac{1}{2},k+\frac{1}{2}} = \left(1 - \frac{k}{N}\right) h(x_{j+\frac{1}{2},k+\frac{1}{2}}) + \frac{k}{N} y_{\max}, & k = 0, \dots, N, \\ y_{\max} + \frac{k-N}{N_s} H_s, & k = N+1, \dots, N+N_s, \end{cases}$$

where $L_s = 3$ and $H_s = 0.63$.

3.3.3.3 Results

We first compute the solution using the constructed mesh with $M = 432$, $N = 132$, $M_s = 9$ and $N_s = 18$ until the final time $t = 293.4$ and plot the obtained potential temperature θ in Figure 3.3.8. In all three Cases (a), (b) and (c), the results qualitatively match those reported in [Dur86; GB06; Kle09]. We have also added the contour lines corresponding to different values of θ with the difference between adjacent contours being 0.01. As one can observe, in all of the three cases the “density” of contours changes at about $y = H_d$. One can also see more contours in the lower layer of atmosphere in Cases (a) and (b), while in Case (c) the situation is opposite: there are less contours in the lower layer. The location where the rate of potential temperature increase changes corresponds to the height of the interface between the two layers. It also indicates the place where turbulence occurs, which provides a useful information for practitioners studying the atmospheric dynamics. In addition, in Cases (a) and (b), one can observe a sharp drop of potential temperature above the downhill part ($0 \leq x \leq 2$). In Case (b), the occurrence of vertical oscillation of the perturbed air, which can be observed at about $x \in [1, 4]$, indicates the phenomenon of Lee waves. At the same time, in Cases (a) and (c), no significant change in gravity waves on the right of the mountain has been observed.

In order to further validate the proposed numerical method, we refine the mesh and compute the solution at the same final time, but using $M = 864$, $N = 264$, $M_s = 18$ and $N_s = 36$. The obtained results, plotted in Figure 3.3.9, clearly demonstrate that the structure of the fine mesh solution is the same as the coarse mesh one, which experimentally indicates the convergence of the method.

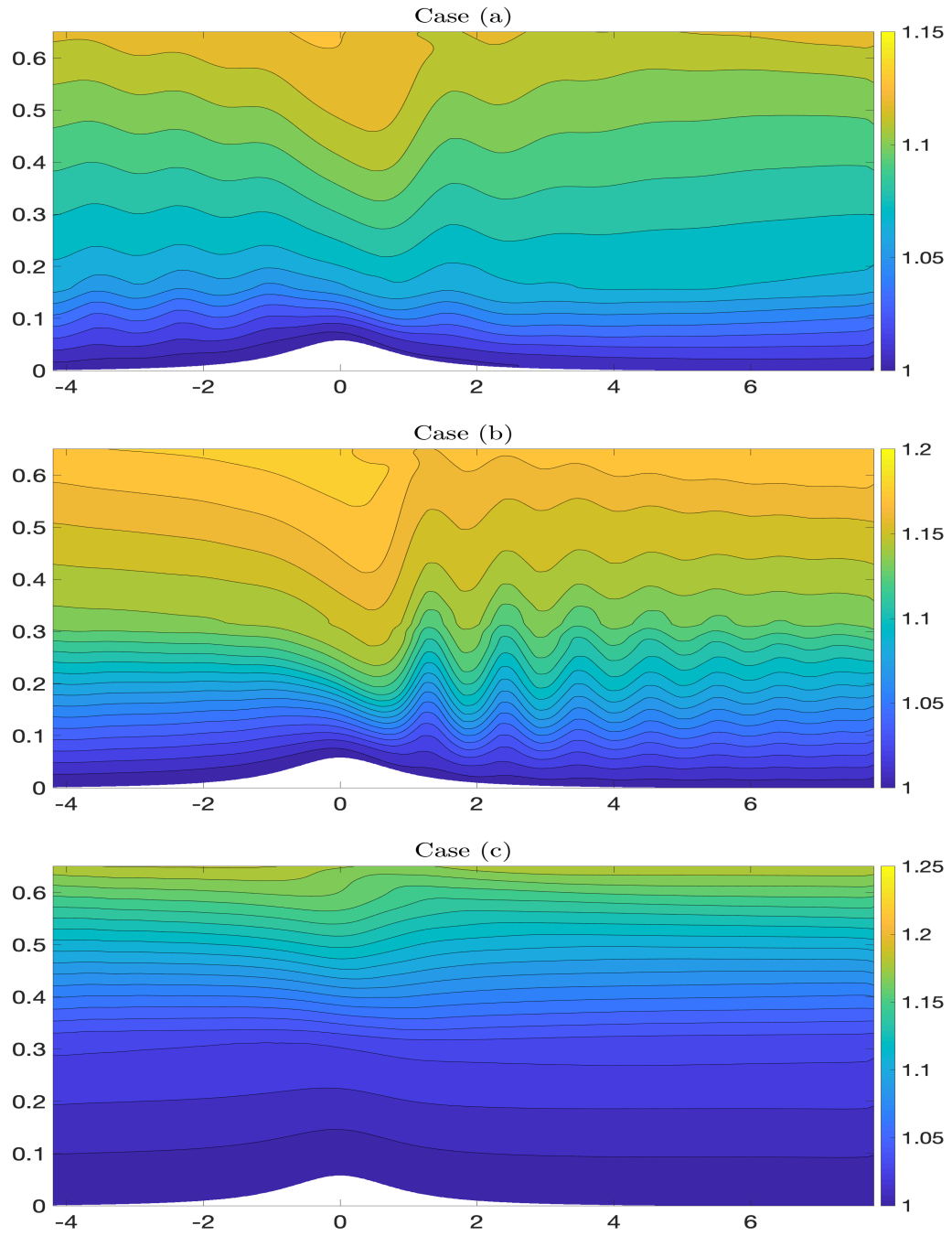


Figure 3.3.8 Example 3: Potential temperature θ at $t = 293.4$ for Cases (a)–(c). Contours are plotted at intervals of $\Delta\theta = 0.01$.

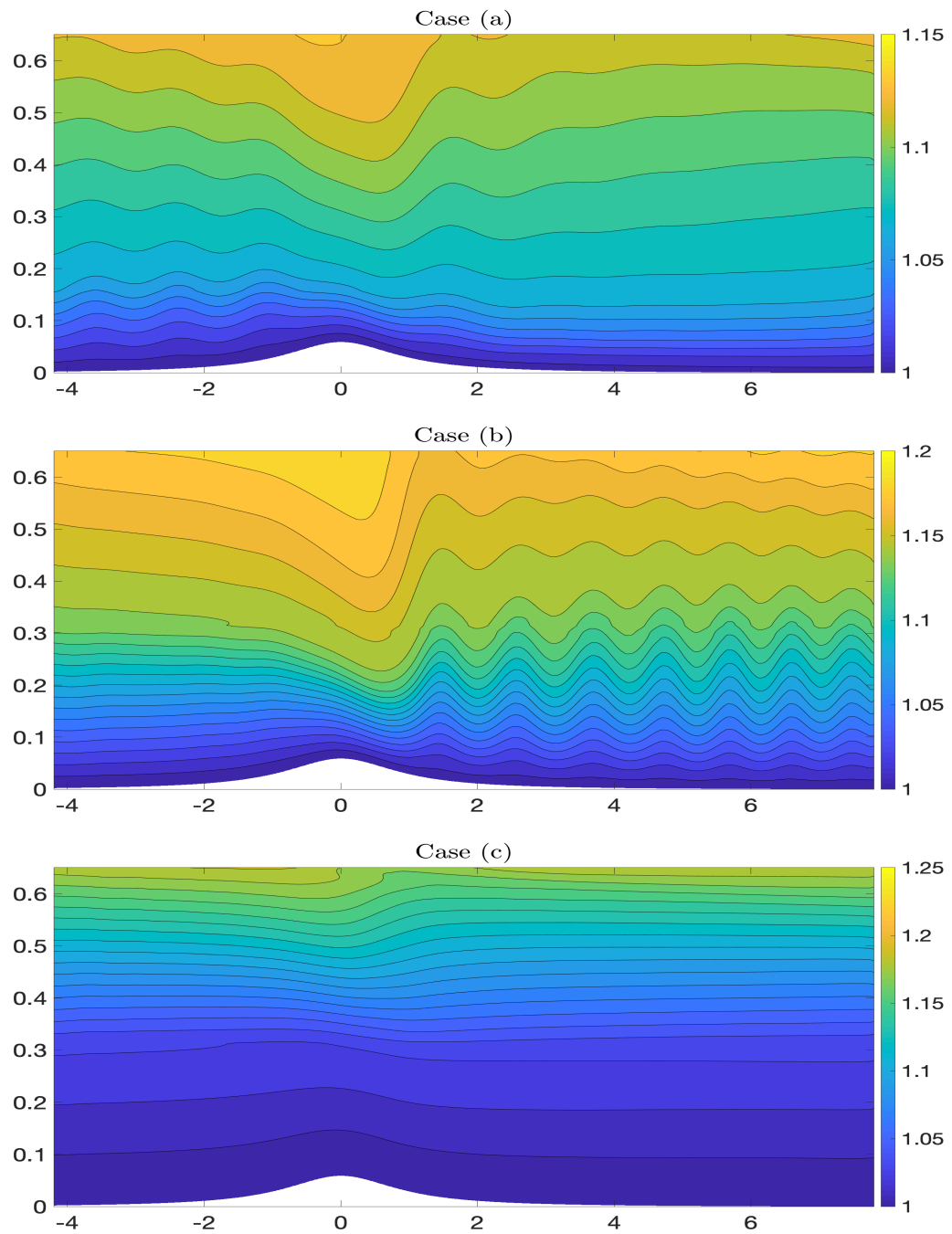


Figure 3.3.9 Same as Figure 3.3.8, but the results are computed using a finer mesh.

CHAPTER

4

CONCLUSIONS AND FUTURE WORK

This thesis presents second-order well-balanced central-upwind schemes for 2 different projects: the non-hydrostatic Saint-Venant system and the compressible system of Euler equations with gravity in irregular domains. Major contributions of 2 projects are summarized here:

- First, we used a second-order well-balanced positivity-preserving central-upwind scheme to study how the non-hydrostatic Saint-Venant system characterizes long-time propagation and on-shore arrival of tsunami-type waves. We discovered that for certain ranges of the dispersive coefficients, both the shape and amplitude of tsunamis are preserved. We also illustrated that on-shore arrival of the tsunami-type waves indicates the importance of non-hydrostatic terms.
- Second, we developed a second-order well-balanced scheme for the compressible Euler equations with gravity in irregular domains using structured quadrilateral grids. We demonstrated how quadrilateral grids are construed for different irregular domains. Besides, we indicated that in numerical experiments, quadrilateral grids perform better than Cartesian grids, especially in characterizing accurate airflow rates near irregular boundaries.

In the future, we plan to study more realistic geophysical and atmospheric systems and explore the possibility of using unstructured and adaptive meshes while conducting numerical simulations in the most general geometry setup.

BIBLIOGRAPHY

- [Arm97] Arminjon, P. et al. “A finite volume extension of the Lax-Friedrichs and Nessyahu-Tadmor schemes for conservation laws on unstructured grids”. *Int. J. Comput. Fluid Dyn.* **9** (1997), pp. 1–22.
- [Bar04] Barthelemy, E. “Nonlinear shallow water theories for coastal waves”. *Surv. Geophys.* **25.3-4** (2004), pp. 315–337.
- [Ber12] Berger, M. & Helzel, C. “A simplified h -box method for embedded boundary grids”. *SIAM J. Sci. Comput.* **34.2** (2012), A861–A888.
- [Bia99] Bianco, F. et al. “High order central schemes for hyperbolic systems of conservation laws”. *SIAM J. Sci. Comput.* **21** (1999), pp. 294–322.
- [Bol13] Bollermann, A. et al. “A Well-Balanced Reconstruction of Wet/Dry Fronts for the Shallow Water Equations”. *Journal of Scientific Computing* **56.2** (2013), pp. 267–290.
- [Bon02] Bona, J. L. et al. “Boussinesq equations and other systems for small-amplitude long waves in nonlinear dispersive media. I. Derivation and linear theory”. *J. Nonlinear Sci.* **12.4** (2002), pp. 283–318.
- [Bon04] Bona, J. L. et al. “Boussinesq equations and other systems for small-amplitude long waves in nonlinear dispersive media. II. The nonlinear theory”. *Nonlinearity* **17.3** (2004), pp. 925–952.
- [Bot04] Botta, N. et al. “Well balanced finite volume methods for nearly hydrostatic flows”. *J. Comput. Phys.* **196** (2004), pp. 539–565.
- [Bra20] Brady, P. T. & Livescu, D. “Foundations for high-order, conservative cut-cell methods: Stable discretizations on degenerate meshes”. *J. Comput. Phys.* (2020), p. 109794.
- [Bri08] Bristeau, M.-O. & Sainte-Marie, J. “Derivation of a non-hydrostatic shallow water model; comparison with Saint-Venant and Boussinesq systems”. *Discrete Contin. Dyn. Syst. Ser. B* **10.4** (2008), pp. 733–759.
- [Bri11] Bristeau, M.-O. et al. “Numerical simulations of a non-hydrostatic shallow water model”. *Comput. & Fluids* **47.1** (2011), pp. 51–64.
- [Bry08] Bryant, E. *Tsunami: the Underrated Hazard*. 2nd ed. Cambridge University Press, 2008.
- [Bur05] Burden, R. L. & Faires, D. J. *Numerical Analysis*. 8th ed. Brooks Cole, 2005.
- [CD] Castro Díaz, M. J. et al. “Path-conservative central-upwind schemes for nonconservative hyperbolic systems”. *ESAIM Math. Model. Numer. Anal.* (). To appear.
- [Che16] Cheng, Y. & Kurganov, A. “Moving-water equilibria preserving central-upwind schemes for the shallow water equations”. *Commun. Math. Sci.* **14.6** (2016), pp. 1643–1663.

- [Che15] Chertock, A. et al. “Well-balanced positivity preserving central-upwind scheme for the shallow water system with friction terms”. *International Journal for Numerical Methods in Fluids* **78.6** (2015), pp. 355–383.
- [Che18] Chertock, A. et al. “Well-balanced schemes for the Euler equations with gravitation: Conservative formulation using global fluxes”. *J. Comput. Phys.* **358** (2018), pp. 36–52.
- [Che20] Chertock, A. et al. “Central-upwind scheme for a non-hydrostatic Saint-Venant system”. *Proceedings of the XVII International Conference on Hyperbolic Problems: Theory, Numerics and Applications* **10** (2020).
- [Che21] Chertock, A. et al. “Well-Balanced Numerical Method for Atmospheric Flow Equations with Gravity”. *Submitted* (2021).
- [Chr08] Christov, I. & Popov, B. “New nonoscillatory central schemes on unstructured triangulations for hyperbolic systems of conservation laws”. *J. Comput. Phys.* **227** (2008), pp. 5736–5757.
- [Dur86] Durran, D. “Another look at downslope windstorms. Part I: The development of analogs to supercritical flow in an infinitely deep, continuously stratified fluid”. *J. Atmos. Sci.* **43** (1986), pp. 2527–2543.
- [Fal93] Falconer, R. “An Introduction to Nearly Horizontal Flows”. *Coastal, Estuarial and Harbour Engineers’ Reference Book* (1993), pp. 27–36.
- [FN08] Fernández-Nieto, E. D. et al. “A new Savage-Hutter type model for submarine avalanches and generated tsunami”. *J. Comput. Phys.* **227** (2008), pp. 7720–7754.
- [Gab18] Gaburro, E. et al. “Well-balanced Arbitrary-Lagrangian-Eulerian finite volume schemes on moving nonconforming meshes for the Euler equations of gas dynamics with gravity”. *Mon. Not. R. Astron. Soc.* **477.2** (2018), pp. 2251–2275.
- [GC75] Gal-Chen, T. & Somerville, R. “On the use of a coordinate transformation for the solution of the Navier-Stokes equations”. *J. Comput. Phys.* **17** (1975), pp. 209–228.
- [GB06] Gatti-Bono, C. & Colella, P. “An anelastic allspeed projection method for gravitationally stratified flows”. *J. Comput. Phys.* **216** (2006), pp. 589–615.
- [God59] Godunov, S. “A difference method for numerical calculation of discontinuous solutions of the equations of hydrodynamics”. *Mat. Sb. (N.S.)* **47 (89)** (1959), pp. 271–306.
- [Gok18] Gokhale, N. et al. “A dimensionally split Cartesian cut cell method for hyperbolic conservation laws”. *J. Comput. Phys.* **364** (2018), pp. 186–208.
- [Got01] Gottlieb, S. et al. “Strong stability-preserving high-order time discretization methods”. *SIAM Rev.* **43** (2001), pp. 89–112.
- [Got11] Gottlieb, S. et al. *Strong stability preserving Runge-Kutta and multistep time discretizations*. World Scientific Publishing Co. Pte. Ltd., Hackensack, NJ, 2011, pp. xii+176.

- [Gre76] Green, A. & Naghdi, P. “A derivation of equations for wave propagation in water at variable depth”. *J. Fluid Mech.* **78** (1976), pp. 237–246.
- [Hei01] Heinrich, P. et al. “Numerical modelling of tsunami generation and propagation from submarine slumps: the 1998 Papua New Guinea event”. *Geophys. J. Int.* **145** (2001), pp. 97–111.
- [Hig09] Higuera, I. “Characterizing strong stability preserving additive Runge-Kutta methods”. *J. Sci. Comput.* **39.1** (2009), pp. 115–128.
- [Jan89] Janji, Z. I. “On the pressure gradient force error in σ -coordinate spectral models”. *Mon. Wea. Rev.* **117** (1989), pp. 2285–2292.
- [Jia98] Jiang, G.-S. & Tadmor, E. “Nonoscillatory central schemes for multidimensional hyperbolic conservation laws”. *SIAM J. Sci. Comput.* **19.6** (1998), 1892–1917 (electronic).
- [Käp16] Käppeli, R. & Mishra, S. “A well-balanced finite volume scheme for the Euler equations with gravitation. The exact preservation of hydrostatic equilibrium with arbitrary entropy stratification”. *Astron. Astrophys.* **587** (2016), A94.
- [Kle09] Klein, R. et al. “Well-balanced compressible cut-cell simulation of atmospheric flow”. *Philos. Trans. R. Soc. Lond. Ser. A Math. Phys. Eng. Sci.* **367.1907** (2009), pp. 4559–4575.
- [Kli19] Klingenberg, C. et al. “Arbitrary order finite volume well-balanced schemes for the Euler equations with gravity”. *SIAM J. Sci. Comput.* **41.2** (2019), A695–A721.
- [Kur18] Kurganov, A. “Finite-volume schemes for shallow-water equations”. *Acta Numer.* **27** (2018), pp. 289–351.
- [Kur00a] Kurganov, A. & Levy, D. “Third-order semi-discrete central scheme for conservation laws and convection-diffusion equations”. *SIAM J. Sci. Comput.* **22** (2000), pp. 1461–1488.
- [Kur02] Kurganov, A. & Levy, D. “Central-upwind schemes for the Saint-Venant system”. *M2AN Math. Model. Numer. Anal.* **36** (2002), pp. 397–425.
- [Kur07a] Kurganov, A. & Lin, C.-T. “On the reduction of numerical dissipation in central-upwind schemes”. *Commun. Comput. Phys.* **2.1** (2007), pp. 141–163.
- [Kur07b] Kurganov, A. & Lin, C.-T. “On the reduction of numerical dissipation in central-upwind schemes”. *Commun. Comput. Phys.* **2** (2007), pp. 141–163.
- [Kur14] Kurganov, A. & Miller, J. “Central-upwind scheme for Savage-Hutter type model of submarine landslides and generated tsunami waves”. *Comput. Methods Appl. Math.* **14** (2014), pp. 177–201.
- [Kur00b] Kurganov, A. & Petrova, G. “Central schemes and contact discontinuities”. *M2AN Math. Model. Numer. Anal.* **34.6** (2000), pp. 1259–1275.

- [Kur01a] Kurganov, A. & Petrova, G. “A third-order semi-discrete genuinely multidimensional central scheme for hyperbolic conservation laws and related problems”. *Numer. Math.* **88.4** (2001), pp. 683–729.
- [Kur07c] Kurganov, A. & Petrova, G. “A second-order well-balanced positivity preserving central-upwind scheme for the Saint-Venant system”. *Commun. Math. Sci.* **5** (2007), pp. 133–160.
- [Kur09] Kurganov, A. & Petrova, G. “Central-upwind schemes for two-layer shallow equations”. *SIAM J. Sci. Comput.* **31** (2009), pp. 1742–1773.
- [Kur00c] Kurganov, A. & Tadmor, E. “New high resolution central schemes for nonlinear conservation laws and convection-diffusion equations”. *J. Comput. Phys.* **160** (2000), pp. 241–282.
- [Kur00d] Kurganov, A. & Tadmor, E. “New high-resolution semi-discrete central scheme for Hamilton-Jacobi equations”. *J. Comput. Phys.* **160** (2000), pp. 720–742.
- [Kur01b] Kurganov, A. et al. “Semi-discrete central-upwind scheme for hyperbolic conservation laws and Hamilton-Jacobi equations”. *SIAM J. Sci. Comput.* **23** (2001), pp. 707–740.
- [Kur07d] Kurganov, A. et al. “Adaptive semi-discrete central-upwind schemes for nonconvex hyperbolic conservation laws”. *SIAM J. Sci. Comput.* **29** (2007), pp. 2381–2401.
- [Kur17] Kurganov, A. et al. “Second-order fully discrete central-upwind scheme for two-dimensional hyperbolic systems of conservation laws”. *SIAM J. Sci. Comput.* **39.3** (2017), A947–A965.
- [Kur20] Kurganov, A. et al. “Adaptive moving mesh central-upwind schemes for hyperbolic system of PDEs. Applications to compressible Euler equations and granular hydrodynamics”. *Commun. Appl. Math. Comput.* (2020). To appear.
- [LeV11a] LeVeque, R. J. “A well-balanced path-integral f-wave method for hyperbolic problems with source terms”. *J. Sci. Comput.* **48.1-3** (2011), pp. 209–226.
- [LeV11b] LeVeque, R. J. et al. “Tsunami modelling with adaptively refined finite volume methods”. *Acta Numer.* **20** (2011), pp. 211–289.
- [Lev99] Levy, D. et al. “Central WENO schemes for hyperbolic systems of conservation laws”. *M2AN Math. Model. Numer. Anal.* **33.3** (1999), pp. 547–571.
- [Lie03] Lie, K.-A. & Noelle, S. “On the artificial compression method for second-order nonoscillatory central difference schemes for systems of conservation laws”. *SIAM J. Sci. Comput.* **24.4** (2003), pp. 1157–1174.
- [MI06] Mercado-Irizarry, A. & Liu, P. L. F. *Caribbean Tsunami Hazard*. World Scientific, 2006.
- [Mit05] Mittal, P. & Iaccarino, G. “Immersed boundary methods”. *Annu. Rev. Fluid Mech.* **37** (2005), pp. 239–261.

- [Nes90] Nessyahu, H. & Tadmor, E. “Nonoscillatory central differencing for hyperbolic conservation laws”. *J. Comput. Phys.* **87.2** (1990), pp. 408–463.
- [Ort00] Ortiz, M. et al. “A fast preliminary estimation model for transoceanic tsunami propagation”. *Geofis. Int.* **39** (2000), pp. 207–220.
- [Phi57] Phillips, N. A. “A coordinate system having some special advantages for numerical forecasting”. *J. Atmos. Sci.* **14** (1957), pp. 184–185.
- [SV71] Saint-Venant, A. J. C. de. “Théorie du mouvement non-permanent des eaux, avec application aux crues des rivières et à l’introduction des marées dans leur lit.” *C.R. Acad. Sci. Paris* **73** (1871), pp. 147–154.
- [She50] Sherman, J. & Morrison, W. J. “Adjustment of an inverse matrix corresponding to a change in one element of a given matrix”. *Ann. Math. Statistics* **21** (1950), pp. 124–127.
- [Shi16] Shirkhani, H. et al. “A well-balanced positivity-preserving central-upwind scheme for shallow water equations on unstructured quadrilateral grids”. *Comput. & Fluids* **126** (2016), pp. 25–40.
- [Sim81] Simmons, A. J. & Burridge, D. M. “An energy and angular-momentum conserving vertical finite-difference scheme and hybrid vertical coordinates”. *Mon. Wea. Rev.* **109** (1981), pp. 758–766.
- [Sun76] Sundqvist, H. “On vertical interpolation and truncation in connexion with use of sigma system models”. *Atmosphere* **14** (1976), pp. 37–52.
- [Swe84] Sweby, P. K. “High resolution schemes using flux limiters for hyperbolic conservation laws”. *SIAM J. Numer. Anal.* **21.5** (1984), pp. 995–1011.
- [Tre97] Trefethen, L. & Bau, D. *Numerical Linear Algebra*. Society for Industrial and Applied Math, 1997.
- [Wan99] Wang, B. & Glaz, H. “Second order Godunov-like schemes for gas dynamics with a nonconvex equation of state” (1999).
- [Xin13] Xing, Y. & Shu, C.-W. “High order well-balanced WENO scheme for the gas dynamics equations under gravitational fields”. *J. Sci. Comput.* **54** (2013), pp. 645–662.

APPENDICES

APPENDIX

A

LEIBNIZ INTEGRAL RULE

Theorem. Let $f(x, t)$ be a function such that $f_x(x, t)$ are continuous in t and x in some region of the (x, t) -plane, including $a(x) \leq t \leq b(x)$, $x_0 \leq x \leq x_1$. Also suppose that the functions $a(x)$ and $b(x)$ are both continuous and both have continuous derivatives for $x_0 \leq x \leq x_1$. Then, for $x_0 \leq x \leq x_1$,

$$\frac{d}{dx} \left(\int_{a(x)}^{b(x)} f(x, t) dt \right) = \int_{a(x)}^{b(x)} \frac{\partial f(x, t)}{\partial x} dt + f(x, b(x)) \cdot \frac{d}{dx} b(x) - f(x, a(x)) \cdot \frac{d}{dx} a(x). \quad (\text{A.0.1})$$

APPENDIX

B

RANKINE-HUGONIOT JUMP CONDITION

B.1 Derivation of Rankine-Hugoniot Jump Condition

Here we would like to derive Rankine-Hugoniot jump condition. Suppose there's a jump across curve $x = \xi(t)$ in one dimensional differential equation of conservation laws:

$$\begin{aligned}\frac{\partial q}{\partial t} + \frac{\partial F(q)}{\partial x} &= 0, \\ q(x, 0) &= q_0(x),\end{aligned}\tag{B.1.1}$$

then q must satisfy this condition:

$$\frac{F(q^-) - F(q^+)}{q^- - q^+} = \xi'(t).\tag{B.1.2}$$

Suppose $x_1 < \xi(t) < x_2$, then

$$\begin{aligned}\frac{\partial}{\partial t} \int_{x_1}^{x_2} q(x, t) dx &= \int_{x_1}^{x_2} \frac{\partial q(x, t)}{\partial t} dx \\ &= - \int_{x_1}^{x_2} \frac{\partial F(q)}{\partial x} dx \\ &= F(q(x_1, t)) - F(q(x_2, t))\end{aligned}\tag{B.1.3}$$

$$\begin{aligned}\frac{\partial}{\partial t} \int_{x_1}^{x_2} q(x, t) dx &= \frac{\partial}{\partial t} \left[\int_{x_1}^{\xi(t)-} q(x, t) dx + \int_{\xi(t)+}^{x_2} q(x, t) dx \right] \\ &= \int_{x_1}^{\xi(t)-} \frac{\partial q(x, t)}{\partial t} dx + q(\xi(t)-, t) \frac{d[\xi(t)-]}{dt}\end{aligned}\tag{B.1.4}$$

$$+ \int_{\xi(t)+}^{x_2} \frac{\partial q(x, t)}{\partial t} dx - q(\xi(t)+, t) \frac{d[\xi(t)+]}{dt}\tag{B.1.5}$$

Here, note that if we let $x_1 \rightarrow \xi(t)-$, $x_2 \rightarrow \xi(t)+$, we will have $q(x_1, t) \rightarrow q^-$, $q(x_2, t) \rightarrow q^+$, $F(q(x_1, t)) \rightarrow F(q^-)$ and $F(q(x_2, t)) \rightarrow F(q^+)$.

Since slopes at different sides of the jump are assumed to be the same, we have $\frac{d[\xi(t)-]}{dt} = \frac{d[\xi(t)+]}{dt}$.

Then combine B.1.3 and B.1.5, we have

$$F^- - F^+ = (q^- - q^+) \frac{d\xi(t)}{dt}\tag{B.1.6}$$

$$\frac{F(q^-) - F(q^+)}{q^- - q^+} = \xi'(t)\tag{B.1.7}$$

APPENDIX

C

THIRD-ORDER STRONG STABILITY PRESERVING RUNGE-KUTTA METHODS

We start by considering the following 1-D semi-discrete system of ODE systems:

$$\frac{d}{dt} q(t) = L(q(t)), \quad (\text{C.0.1})$$

where q is the vector of functions to solve and $L(q(t))$ is its spatial discretization.

Here, we choose the three-stage third-order strong stability preserving (SSP) Runge-Kutta method (see [Hig09; Got01; Got11] for details) which is a convex combination of forward Euler steps:

$$\begin{aligned} q^{(1)} &= q^n + \Delta t L(q^n), \\ q^{(2)} &= \frac{3}{4} q^n + \frac{1}{4} \left(q^{(1)} + \Delta t L(q^{(1)}) \right), \\ q^{n+1} &= \frac{1}{3} q^n + \frac{2}{3} \left(q^{(2)} + \Delta t L(q^{(2)}) \right), \end{aligned} \quad (\text{C.0.2})$$

where $q^n = q(\cdot, t^n)$.

Take one-dimensional balance laws as an example:

$$\frac{d}{dt} \bar{q}_j = -\frac{1}{\Delta x} \left[H_{j+\frac{1}{2}} - H_{j-\frac{1}{2}} \right] + \bar{S}_j, \quad (\text{C.0.3})$$

where j represents the index of cells in the computational domain, \bar{q}_j is the cell average of vector of

unknowns, \bar{S}_j is numerical discretization of source term, $H_{j\pm\frac{1}{2}}$ is numerical fluxes in j -th cell. We can rewrite the RHS of (C.0.3) such that

$$L(q_j) = -\frac{1}{\Delta x} [H_{j+\frac{1}{2}} - H_{j-\frac{1}{2}}] + \bar{S}_j.$$

The SSP-RK3 procedure, which entails evolving the system as a convex combination of forward Euler steps, is given by

$$\begin{aligned} q_j^{(1)} &= q_j^n + \Delta t L(q_j^n), \\ q_j^{(2)} &= \frac{3}{4} q_j^n + \frac{1}{4} \left[q_j^{(1)} + \Delta t L(q_j^{(1)}) \right], \\ q_j^{n+1} &= \frac{1}{3} q_j^n + \frac{2}{3} \left[q_j^{(2)} + \Delta t L(q_j^{(2)}) \right]. \end{aligned} \tag{C.0.4}$$

For two-dimensional case, recall in (3.2.8), we have

$$\frac{d}{dt} \bar{Q}_{j,k} = -\frac{1}{|C_{j,k}|} [H_{j+\frac{1}{2},k} - H_{j-\frac{1}{2},k} + H_{j,k+\frac{1}{2}} - H_{j,k-\frac{1}{2}}] + \bar{S}_{j,k}, \tag{C.0.5}$$

where j, k represents the index of cells in the computational domain, $\bar{Q}_{j,k}$ is the cell average of vector of unknowns, $\bar{S}_{j,k}$ is the numerical discretization of the source term, $H_{j\pm\frac{1}{2},k}$ is numerical fluxes in the x -direction, $H_{j,k\pm\frac{1}{2}}$ is numerical fluxes in the y -direction in (j, k) -th cell. We can rewrite the RHS of (C.0.5) such that

$$L(Q_{j,k}) = -\frac{1}{|C_{j,k}|} [H_{j+\frac{1}{2},k} - H_{j-\frac{1}{2},k} + H_{j,k+\frac{1}{2}} - H_{j,k-\frac{1}{2}}] + \bar{S}_{j,k}.$$

The SSP-RK3 procedure, which entails evolving the system as a convex combination of forward Euler steps, is given by

$$\begin{aligned} Q_{j,k}^{(1)} &= Q_{j,k}^n + \Delta t L(Q_{j,k}^n), \\ Q_{j,k}^{(2)} &= \frac{3}{4} Q_{j,k}^n + \frac{1}{4} \left[Q_{j,k}^{(1)} + \Delta t L(Q_{j,k}^{(1)}) \right], \\ Q_{j,k}^{n+1} &= \frac{1}{3} Q_{j,k}^n + \frac{2}{3} \left[Q_{j,k}^{(2)} + \Delta t L(Q_{j,k}^{(2)}) \right]. \end{aligned} \tag{C.0.6}$$